LED PUMPED Nd:YAG LASER DEVELOPMENT PROGRAM

IBM

FSC 73-5027

LED PUMPED Nd:YAG LASER DEVELOPMENT PROGRAM

Final Report

Contract No. NAS 8-27563

March 16, 1973

Prepared by

G. I. Farmer, Y. C. Kiang, and R. J. Lynch

for

National Aeronautics and Space Administration

Huntsville, Alabama

Federal System Division

INTERNATIONAL BUSINESS MACHINES CORPORATION

Gaithersburg, Maryland 20760

ABSTRACT

This report describes the results of a development program for light emitting diode (LED) pumped Nd:YAG lasers. A significant design feature, an index matching method to increase the coupling efficiency of the laser is described. A solid glass half-cylinder of 5.0 by 5.6 centimeters was used for index matching and also as a pumping cavity reflector. Twenty 0.034x0.254 cm^2 GaAlAs diodes, connected in series, were aligned such that the emission area formed a straight line. The laser rods were 1.5 by 56 millimeters with dielectric coatings on both end surfaces. The interfaces between the diode array, glass cylinder, and laser rod were filled with viscous fluid of refractive index n = 1.55. Experiments performed with both the glass cylinder and a gold coated stainless steel reflector of the same dimensions under the same operating conditions indicated that the index matching cylinder gave 159 to 200 percent improvement of coupling efficiency over the metal reflector at various operating temperatures. For driving current density 207 A/cm^2, the laser produced CW output power of 27 milliwatts with the laser rod temperature at -27° C.

The dynamic behavior of the Neodymium-doped Yttrium Aluminum Garnet (Nd:YAG) laser has been analyzed using the nonlinear rate equations. The laser threshold, optimum power output, and amplitude modulation by pumping intensity variation have been evaluated and compared with experimental results.

CONTENTS

CONTENTS (Continued)

ILLUSTRATIONS

ILLUSTRATIONS (Continued)

TABLES

LIST OF ABBREVIATIONS AND SYMBOLS

Å	Angstrom
AuGeNi	Gold Germanium Nickel
AuZn	Gold Zinc
GaAlAs $= Ga_{1-x}Al_xA_s$	Gallium Aluminum Arsenide
GaAs	Gallium Arsenide
μ	Micron
LED	Light Emitting Diode
LPE	Liquid Phase Epitaxial
Nd:YAG	Neodymium Doped Yttrium Aluminum Garnet
p-n	Semiconductor Doping Types
Te	Tellurium
Sn	Tin
HLPE	Horizontal Liquid Phase Epitaxial

1.1 PROGRAM GOAL

This final report covers research and development activity begun in July 1971 at IBM - Federal Systems Division (FSD), Gaithersburg, Maryland. During the subsequent 18-month period, work was performed in FSD laboratories in Gaithersburg, Maryland, and Owego, New York, to develop a space qualifiable diode pumped Nd:YAG laser. The performance goals for this laser were an output power of 0.5 to 1 watt CW at 1.06 microns, TEM_{00} mode, with at least 1 percent efficiency and amplitude stability 1 percent or better. The final device should be rugged and durable and should have an operating life of at least 10,000 hours. Cryogenic cooling used on some LED-pumped Nd:YAG devices in the past is undesirable, and its elimination was a prime consideration in this program. Initially, this project was envisioned as consisting of two parts. Part I, the work covered by this report, was intended to obtain the most efficient laser pump head possible and to deliver a representative Nd:YAG laser that can be used in field tests or serve as a progress milestone. Part II will require the manufacture and delivery of a space qualifiable diode pumped Nd:YAG laser.

1.2 PROPOSED APPROACH

It was proposed to make two main efforts in this program:

1. Grow efficient and long lived $Ga_{1-x}Al_xAs$ light emitting diodes at peak emission wavelength near 8100 Å.

2. Use index matching technique on diode arrays to optimize optical coupling from pumping source to the laser rod thereby increasing overall efficiency.

Improvement of $Ga_{1-x}Al_xAs$ diode efficiency was essential for the success of this program. Rectangular shaped "flip-chip" diodes with a minimum bandgap structure, as described in the final report, NASA Contract NAS8-11447, appeared to be a desirable diode structure for this goal. This structure has the advantages that:

a. The p-n junction is very close to the heat sink for heat removal

b. The operating current density in linear arrays is lower compared with domed diodes for the same excitation density

c. Light emitted through n type GaAlAs layers encounters little absorption because of the minimum bandgap structure.

All these factors are crucial for efficient operation and long life of the diodes.

To improve the design of the laser pump, it was proposed to use a solid half cylinder reflector for laser pumping cavity and laser support. This arrangement makes the laser device much more compact in size and rugged. The solid cylinder acts as a pumping reflector and as an index matching medium between the diode semiconductor and the rod. This increases diode output efficiency and improves optical coupling, since diode external quantum efficiency is limited by the total internal reflection at the discontinuity of refractive index of the diode (3.5) to air (1.0). By increasing the refractive index of the material outside the diode surface, the critical angle for total internal reflection is increased; therefore, more light is transmitted through the diode surface and the reflection at the laser rod is also reduced.

1.3 SUMMARY OF THE RESULTS

During the period of this work, two types of GaAlAs diode structures were studied. First, a flip-chip diode geometry was grown with layers of p type $Ga_{1-x}Al_xAs$:Zn and n type $Ga_{1-x}Al_xAs$:Te on n type GaAs:Sn substrates. Because of the long period (18 hours) involved in growing these thick structures (1-5 mils), it was not possible to keep the doping levels at the prescribed values. Also, various defects were observed in the crystals. Consequently, the efficiencies were low and not acceptable for laser device use. The second type of growth was n-up structure with n type $Ga_{1-x}Al_xAs$:Te and p type $Ga_{1-x}Al_xAs$:Zn layers on to p type GaAs:Zn substrate. This proved to be a more useful structure at the present time. This structure was more amenable to obtain the desired wavelength (8070 ± 50 Å) and moderate efficiencies (1.1-1.5%). Life testing of this diode structure was started on two diode arrays (5 and 7) to determine aging characteristics. The operating current of these arrays is one ampere, which is a current density of 115 ampere/cm^2. The arrays are mounted on copper heatsinks held at approximately 20° C. At the end of 4300 hours of CW operation, arrays 5 and 7 were

operating at 70 and 75 percent, respectively of their initial output. The emission spectrum of these diode arrays has shown a negligible change during this testing period.

As a result of this program, a representative model 1.06 microns diode pumped Nd:YAG laser was designed, built, and evaluated. A solid glass index matching cylinder was used to replace the conventional metal reflector as a laser pumping cavity. Experimental results indicated that the improved coupling efficiency of the index matching cylinder was 159 to 200 percent compared with a metal reflector of the same dimensions at various operating temperatures. Theoretical calculation had predicted a 324 percent improvement under those experimental conditions. The discrepancy between theoretical prediction and experimental results was attributed to:

1. The imperfection of the optical alignment of diode array and laser rod

2. Error in reflector configuration

3. Absorption in reflective coating

4. Strain in the rod due to the mismatch between rod groove and glass reflector.

5. Diode efficiency and spectrum are slightly different from the original calibrated values.

Typically, the CW power output was 9 milliwatts at one ampere (or current density 115 A/cm^2) driving current to the diode array with the laser rod temperature at -27° C and diode heat sink temperature at -14° C. For driving current of 1.8 amperes (current density 207 A/cm^2), a CW laser power output of 27 milliwatts was attained.

Further development of diode pumped Nd:YAG lasers is required before practical devices can be built for communication applications. Continuous improvement of some critical technological problems such as diode structure and efficiency which relate directly to thermal conduction and optical coupling encountered in this program must be made before output power and overall efficiency can be substantially improved.

Section 2. $Ga_{1-x}Al_xAs$ LIGHT EMITTING DIODE

2.1 GROWTH OF SEMICONDUCTOR MATERIAL

2.1.1 Introduction

The phenomenon of injection electroluminescence must be explained in terms of the dynamics of a p-n junction. This phenomenon arises when a p-n junction is forward biased so that minority carriers are injected into the bulk regions of the diode on either side of the junction. The recombination of these injected minority carriers with majority carriers already existing in the bulk material can lead to the generation of radiation. The energy of this radiation corresponds to the bandgap of the material from which the diode is made.

The material dealt with in this program was that of $Ga_{1-x}Al_xAs$ with the bandgap energy ($x \simeq 10.6\%$) equivalent to that of ~ 1.53eV for emission at 8070 ± 50Å.

Because of the geometrical configuration of the Nd:YAG device, two types of LED structures were considered. The first of these two was the flip-chip type. This device would be very advantageous since it would have its electrical connections on one side while the other side, free of connections, could be put into intimate contact with the solid cylindrical reflector. The concept here was to grow layers of n-type $Ga_{1-x}Al_xAs$:Te($n = 3 \times 10^{18}$ carrier/cm^3; 0.0127 cm thick) on a GaAs:Sn substrate ($n = 1 - 3 \times 10^{18}$ carrier/cm^3; 0.0457 cm thick). The final step was to grow a p-type $Ga_{1-x}Al_xA_s$:Zn ($n = 1 \times 10^{19}$ carriers/cm^3; 0.00254 cm thick) layer onto the relatively thick n-type $Ga_{1-x}Al_xAs$:Te layers. The growths were carried out using the liquid phase epitaxial technique [1]. The $Ga_{1-x}Al_xAs$ layers were purposely grown thick for structural integrity (i.e., the original GaAs:Sn was completely lapped away). By proper etching techniques, a portion of the p-type $Ga_{1-x}Al_xAs$:Zn layer could be removed to expose the n-type $Ga_{1-x}Al_xAs$:Te layer. Hence, contact could be put on both the n and p type $Ga_{1-x}Al_xAs$ layers by photolithography (on the same back side). In this manner, the device could be fabricated so that the emission would come entirely through the n-region of the $Ga_{1-x}Al_xAs$:Te in which the photons are not strongly absorbed.

Figure 2-1 shows a schematic diagram of the device as grown:

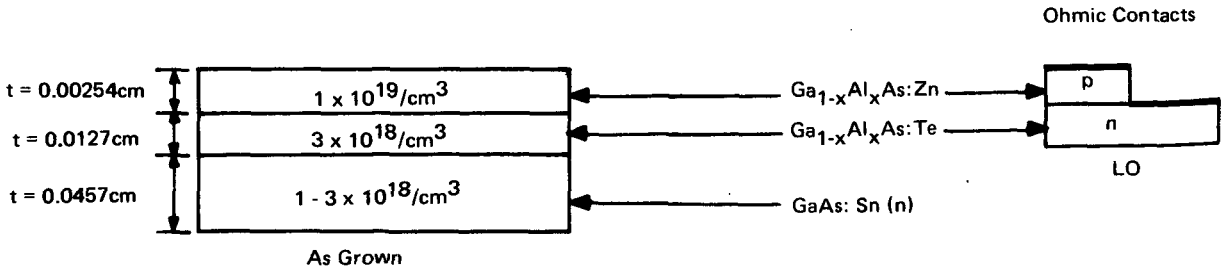

Figure 2-1. Flip-Chip Cross Section

2. 1. 2 Epitaxy Growth Technique

The liquid phase epitaxial (LPE) process has been found successful in producing high quality III-V semiconductor compounds and alloys. Using LPE methods in conjunction with a sliding technique incorporated into the crystal growing furnace, a variety of layered structures have been grown in this laboratory.

This technique of growing epitaxial layers of the desired types has been efficacious for various types of homo and heterojunction devices.

Certain conditions of the layers must be met during the growth process. They are as follows:

a. Smooth layers are mandatory. Lapping and polishing grown layers to obtain smooth layers often damage the surfaces which may degrade the device. By this method of growing, the smoothness requirement has been obtained during the growth process.

b. Uniform layer thickness is especially necessary with ternary alloys like $Ga_{1-x}Al_xAs$ because of the variation of alloy concentration with distance from the substrate layer interface. Without uniform growth, control of diffusion depth into the layer would be difficult, since the diffusion coefficient is effected by the Al/Ga ratio.

Figure 2-2 shows a schematic diagram of the horizontal LPE system. In essence, a special high-purity grade graphite fixture was designed for use in the horizontal furnace.

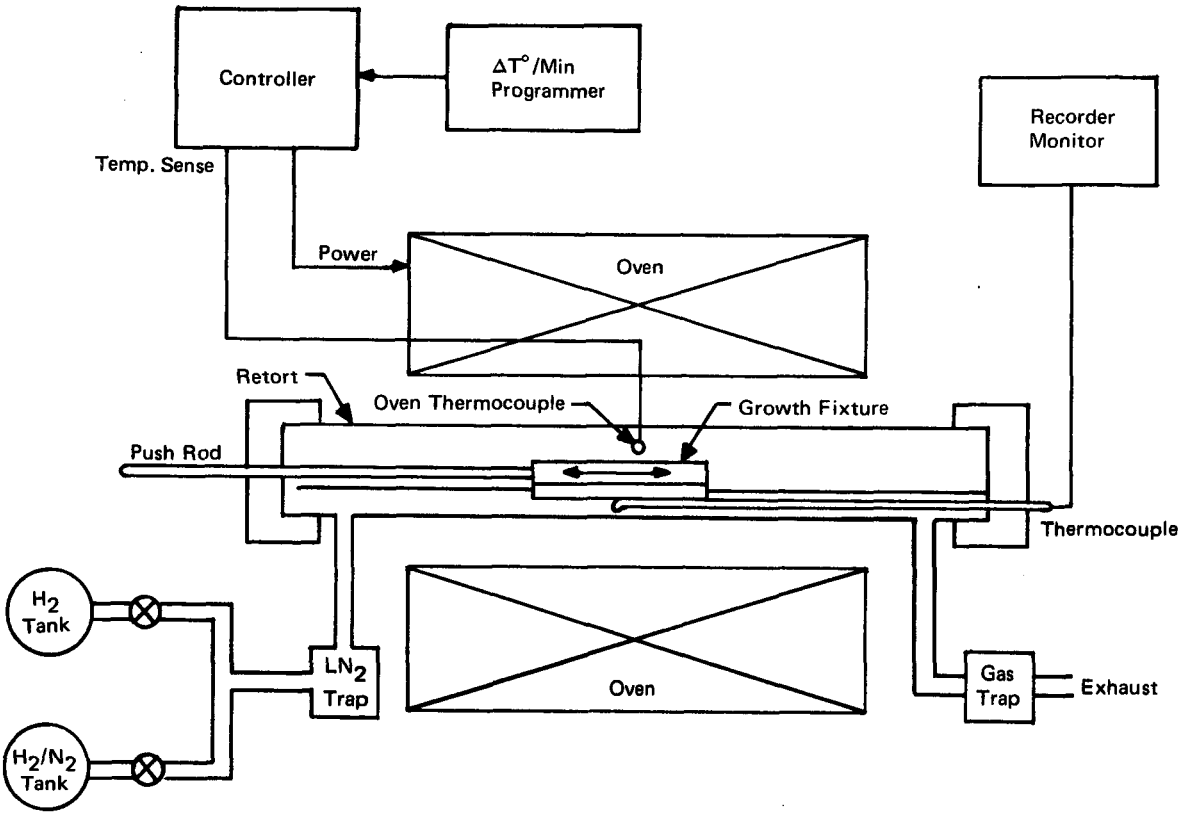

Figure 2-2. Block Diagram of Horizontal LPE System

Figure 2-3 shows this fixture with its four parts labeled 3, 4, 5 and 6. When in use, this fixture is placed in a crystal growing furnace whose temperatures are programmed for the correct value at each step of growth. For the flip-chip layered growth only two parts are required.

In practice, the slider designated by 2 is moved to the right side of the graphite holder labeled 1. When in this position, the GaAs substrate on which the growth is to take place is under the part labeled 3. The material to produce the first layer of n-$Ga_{1-x}Al_xAs$ on the n-GaAs substrate is placed in the part labeled 4. Typically, this part contains 15.00090 grams of Ga; 2.01450 milligrams of polycrystalline GaAs; 9.75 milligrams Al; and 9.60 milligrams of Te. The part labeled 5 contains the material for the p-type $Ga_{1-x}Al_xAs$ layer. It contains, typically, 15.00050 milligrams of Ga; 2.02280 grams of polycrystalline GaAs; 16.15 milligrams of Al; and 466.80 milligrams of Zn. Through experimentation, it was found that when the first n-layer was grown, the aluminum content of the melt became depleted before the layer was grown to the desired thickness. Consequently, a doping technique (of Al) was added to increase or keep the Al level fairly constant during that part of the growth.

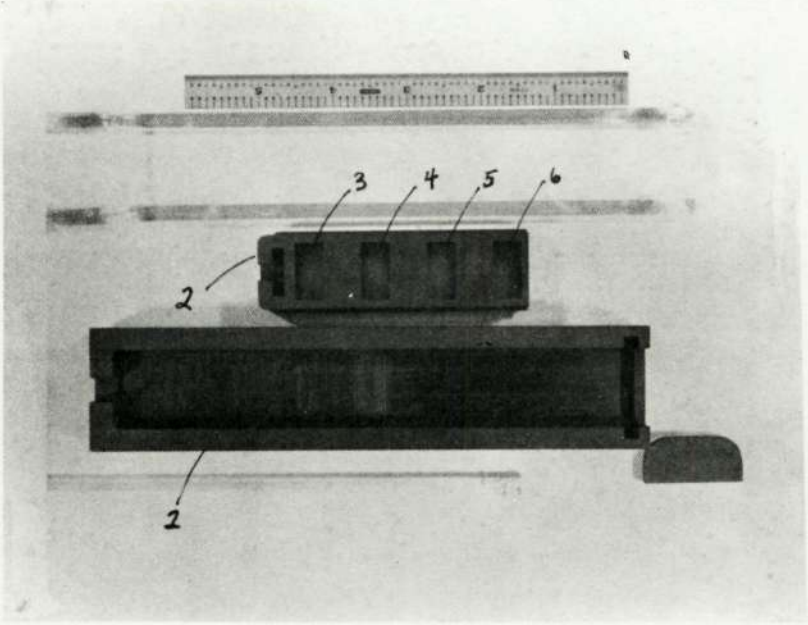

Figure 2-3. Sliding Mechanism for LPE Growth

Figure 2-4 shows a typical thermal profile for such a growth.

This system incorporates a continuous growth process such that the substrate is not removed from the system until the growth is completed.

During the growth process, the system is brought to an equilibrium temperature of 930° C. It is held at this temperature for one hour. During this period there is no material over the substrate. The next step is to reduce the temperature to 920° C (typically) at which time part 4 containing the material for the n-type growth is moved over the substrate. It is held at this temperature for about five minutes and then the temperature is raised to about 931° C for five minutes for equilibrium purposes. At this point the programmer begins to decrease the temperature at a constant rate of 0.043° C per minute. The temperature is allowed to decrease to 916° C. During this time the n-material is grown. At this point it was found that the Al content was being depleted; consequently, an appropriate amount of Al was added to the first melt at the 916° C level. The system was held for 5 minutes at 916° C and then raised to 921° C for some five minutes at which time the programmer began to decease the temperature at the rate of 0.043° C per minute until the 906° C mark was reached. This constituted

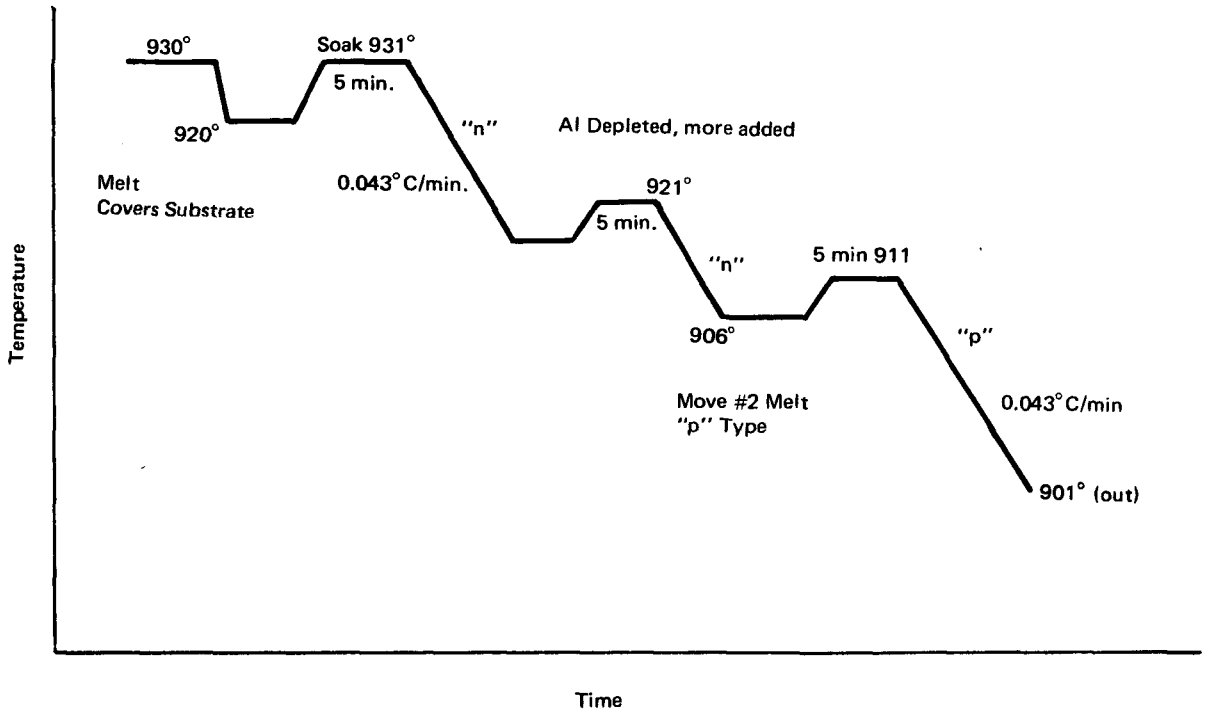

Figure 2-4. Schematic of Thermal Profile of Growth

the end of the n-layer growth. At this point the material in part 5 for the p-growth was moved over the previous growth. The temperature was held at 906° C for five minutes and then the temperature was raised and held at 911° C for five minutes. Then the programmer began to decrease the temperature at the rate of 0. 043° C per minute until 901° C was reached, which constituted the end of the p-type growth. This material is grown under a constant flow of forming gas.

In totality, 20 growth runs (B89 - 104, B-107, 109, 111, 116, 118 and 121) were made in an attempt to grow this flip-chip material. Because of the long growth runs varying from 5 to 18 hours, good diodes were not produced. This was partially attributed to the fact that the dopant levels in the last p-grown layer could not be maintained, that is, the Zn dopant would not remain in the melt over any prolonged length of time.

2. 1. 3 Technical Assessment of the Flip-Chip Material

Four and one-half months of strenuous effort were made to meet the required material characteristics. During this period more than 20 crystal growth runs

were made and analyzed by means of electron microprobing technique. In order to improve upon each succeeding run, certain variables or parameters (Ga/Al ratio, temperature gradients during growth and growth times, etc) were changed to systematically improve the epitaxial growth.

It was concluded by virtue of certain physical conditions of the crystal growing equipment that we are unable to grow the thick uniform layers of a given consistency. This has been manifested in a temperature gradient that develops in the growth apparatus during the extended long period of growing (18 hours) required for constant aluminum levels. The material that was processed had certain deficiencies. Among these are:

a. A thickness gradient across the layer caused by the temperature gradient in the furnace giving a low yield of useful material. This material had a varying aluminum content.

b. The relatively long growth time required to maintain constant aluminum in the layer structure apparently causes crystal defects that manifested themselves in high series resistance in the test diodes.

c. Such crystal imperfections could quite possibly be responsible for the low efficiencies observed in the test diodes. However, there are also other processes that could be responsible for the low efficiencies observed (traps, surface recombination, etc., all of which must be maintained at a minimum for high efficiency).

d. The growth times and the high temperature required for the flip-chip structure make it difficult to provide the proper amount of zinc necessary to produce the proper "p" doping level.

In light of the poor efficiencies obtained from this type of a flip-chip device, it was decided to turn to the concept of "n-up" material. A schematic of this device is seen in the following diagram, Figure 2-5.

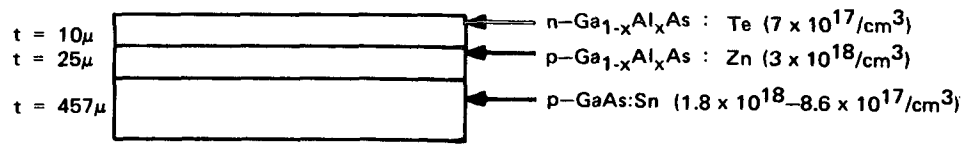

Figure 2-5. N-up Wafer Cross Section

To grow the n-up $Ga_{1-x}Al_xAs$ material, a graphite sliding device other than the one employed for the flip-chip material was used. This fixture is shown in Figure 2-6. In this situation the p-type GaAs:Sn substrate is placed in cavity labeled 1 of the base fixture. Polycrystalline GaAs is placed in the cavity labeled 2. At this point the melt slider is placed upon the base fixture and the remaining components for the first p-type growth is placed in the cavity labeled 3. The doping slider with the proper amounts of Te + Ga are placed in cavity 4 (for the n-growth) and Al + Ga (for the window) are placed in the cavity labeled 5. The cover plate is then placed over the doping slide.

Typically, the following amounts of material are placed in the respective cavities:

p-Growth (Part 3)	n-Growth (Part 4)	Final Doping (Part 5)
Ga = 8.00040 grams	Ga = 175.00 milligrams	Al = 40.40 milligrams
Polycrystalline (undoped) GaAs = 0.96625 grams	Te = 10.40 milligrams	Ga = 176.00 milligrams
Al = 5.90 milligrams		
Zn = 2.70 milligrams		

The latter step produces the high aluminum content (at p-n junction) for the window that provides maximum emission of the radiation through the n-layer.

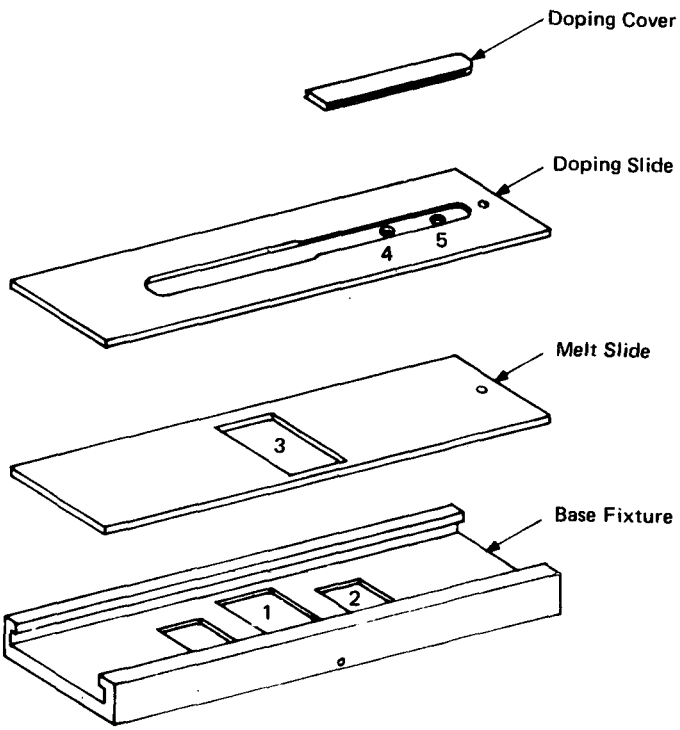

Figure 2-6. HLPE System Doping Fixture

Figure 2-7 shows a schematic of a thermal profile for an n-up layered growth.

In this programmed growth, the system is brought into an equilibrium condition at 925° C and held there for one hour (substrate and melt not in contact). At the end of one hour, the temperature is dropped to 920° C (for saturation to take place). After a time lapse of five minutes, the melt slider is advanced over the substrate (point A, Figure 2-7) and the temperature is raised to 925° C and held there for five minutes. At this point the temperature is begun to be decreased at the rate of 0. 5° C per minute. During this time, when the temperature drops from 925° C to 900° C (50 minutes) the p-type $Ga_{1-x}Al_xAs$ has been grown. After the melt has been held at 900° C for five minutes (point B, Figure 2-7), the doping slide with cavity 4 containing the n-type counter dopant (Te) is advanced over the melt cavity 3. The temperature is now allowed to rise from 900° C to 910° C over a 10-minute period. At the end of this 10-minute period (point C, Figure 2-7), the slide cavity 5 with Al + Ga is advanced over the melt cavity (this provides the high Al content window) and held at the temperature of 910° C for ten minutes. At the end of this time period, the temperature is again reduced at the rate of 0. 5° C per minute. During the time (~ 16 minutes) when the temperature drops from 910° C to 902° C, the n-type $Ga_{1-x}Al_xAs$ layer is grown.

A schematic diagram of the aluminum concentration versus thickness for the grown structure is shown in Figure 2-8.

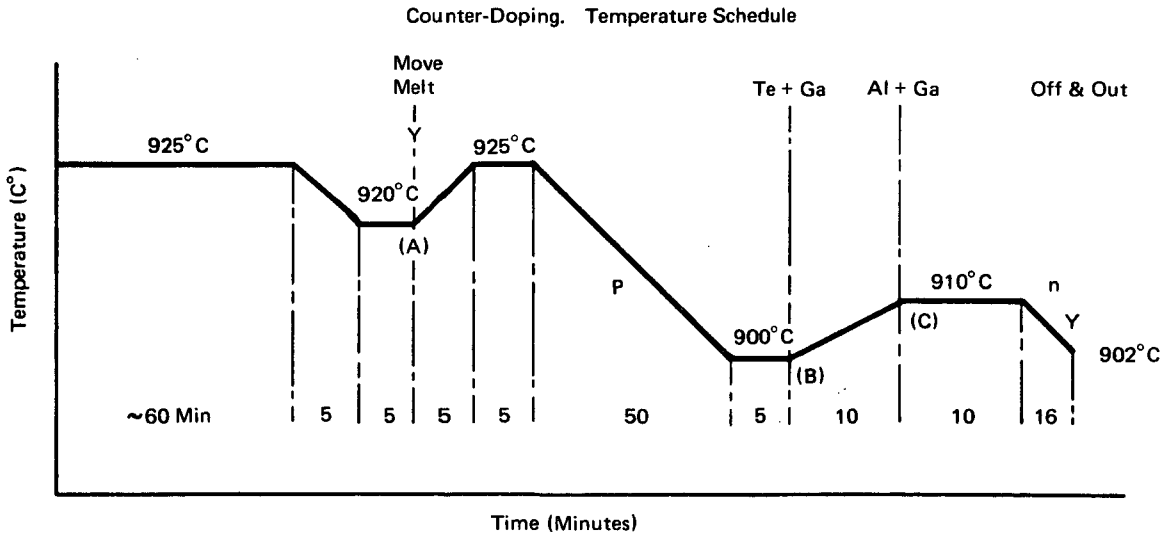

Figure 2-7. Schematic of a Thermal Profile

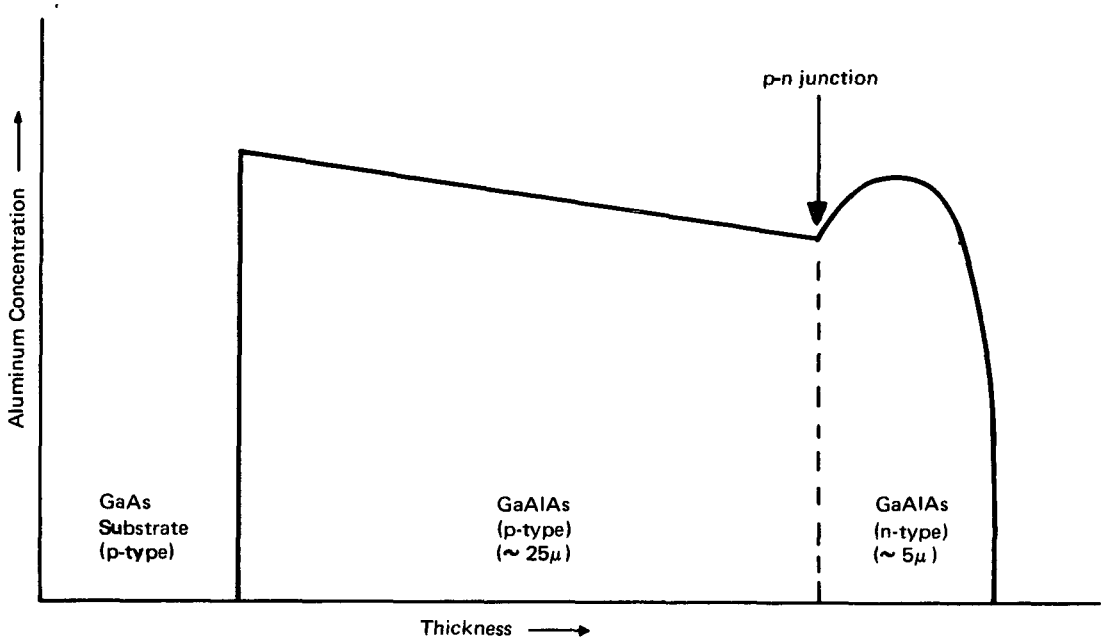

Figure 2-8. Diode Cross Sectional Profile

In order to grow the layered structure with the proper electrical and optical characteristics, a considerable number of runs were made to adjust for the proper aluminum concentration (to yield the correct wavelength) and the proper dopant levels to give the required efficiency. (Of course the efficiency is also dependent upon many other mechanisms and processes in the crystalline material such as lattice defects, radiationless transition, self-absorption, etc.).

In order to characterize the grown material, the aluminum content in each region of the growth was determined by means of the electron microprobe technique. Dopant levels were determined by means of the Hall effect technique.

A total of 30 growth runs were made. Those which exhibited the best efficiencies were assembled in diode arrays.

As an illustration of growth constituents and the results of such growth, Table 2-1 shows the results of seven growth. The data shown in this table was taken on discrete test samples and is not indicative of the entire growth. In each

Table 2-1. Wafer Growth Summary for n-up Growths

Crystal Number	Peak Emission Wavelength λ(Å)	Efficiency η_{ext} (%)	Doping Density		Al (mg)	Te (mg)	Zn (mg)
			n	p			
PL-59	8150-8180	0.97-1.39	$1 \times 10^{18}/cm^3$	$3.2 \times 10^{18}/cm^3$	5.90	2.33	9.41
PL-62	8080	0.7-0.93	$7.7 \times 10^{17}/cm^3$	$3 \times 10^{18}/cm^3$	6.08	2.38	9.24
PL-65	8040	0.96-1.1			6.10	2.38	9.48
PL-66	8080-8100	1.2-1.4			6.11	2.38	9.05
PL-68	8060	1.1-1.27			6.06	2.34	9.10
PL-71	8020-8060	1.1-1.38			6.05	2.32	9.08
PL-72	8000-8020	1.32-1.41			6.09	2.38	9.03

growth there was a certain (unpredictable) amount of nonuniformity, and as a result, the whole growth was not useful for diodes.

2.2 ELECTROLUMINESCENT DIODE ELEMENT

2.2.1 Device Geometry

The objective of the device design was to develop an LED structure that permitted efficient optical coupling into the Nd:YAG laser rod while maintaining a relatively low operating current density. Since low forward current density is usually associated with stable diode operation and long operating lifetimes, previous diode performance was reviewed. Figure 2-9 shows a graphic plot of the number of operating hours to seventy-five percent of initial output as measured using previously fabricated diodes with known current densities (amperes per cm^2). From this graph the value of 110 amperes per cm^2 was selected as a reasonable figure to use for the pumping diodes. Projections on number of hours to half power output exceed 10,000 hours.

Consideration for the diode geometry first took into account the diode width. This was chosen to conform with the TEM_{oo} mode diameter of the laser rod (0.05 cm). The total width was selected to be 0.0343 cm consisting of a 0.0254 cm active emission surface with an additional 0.0089 cm width for ohmic contacting purposes. In order to ensure uniform pumping, the minimum length of the array had to match the five cm length of the Nd:YAG laser rod. Knowing the required active LED area, the selection of the number of diodes to make up the rod distance was influenced by the LPE wafer size/device yield, power supply impedance matching and, of course, the current density. The diode length was chosen at 0.254 cm with each array consisting of 20 diodes (0.0254 cm gap between elements) arranged to approximate a straight line 5.6 cm in length.

Figure 2-10 shows a schematic diagram and a photograph of a typical pumping $Ga_{1-x}Al_xAs$ LED.

The overall diode thickness of 0.014 to 0.0152 cm resulted principally from the amount of GaAs substrate material that was left to ensure the structural integrity of the wafer. Of the aforementioned thickness, the $Ga_{1-x}Al_xAs$ p-n junction usually amounted to approximately 30 μm. In considering the thickness of the GaAlAs n-layer, theoretical calculations had determined that a thickness

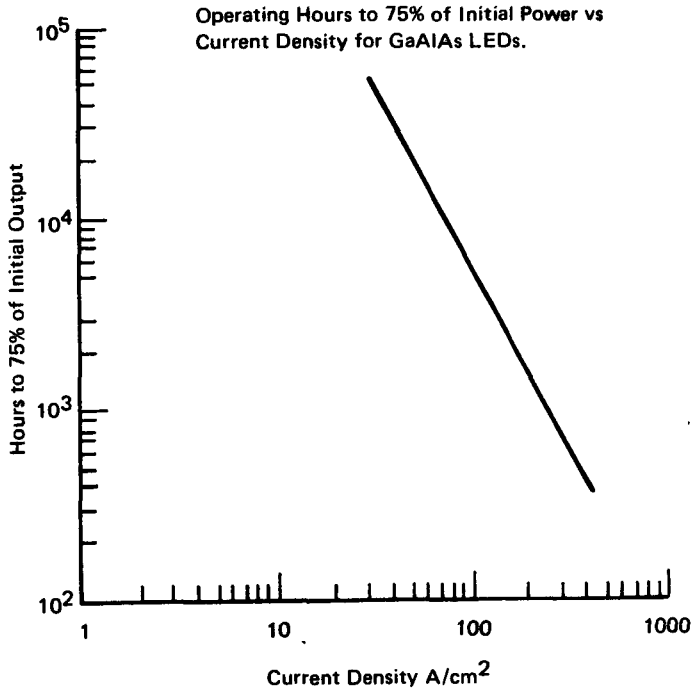

(1) Extrapolated from 26K Hours

Figure 2-9. Previous Lifetime Study Results

of 10 μ m was the best tradeoff thickness between the current crowding effects of too thin a layer and the absorption losses associated with too thick an n-layer. Measurements were made to experimentally validate the optimum value of thickness for the n-layer. The graph shown in Figure 2-11 shows the relative output from diodes taken from the same wafer in which a thickness gradient had been established.

2. 2. 2 Metallurgy

Having polished the GaAs-GaAlAs wafers to the appropriate thicknesses, contact metallurgy was applied to theGaAlAs n-type layer and the p-type GaAs (substrate). The wafers were metallized as quickly as possible following the polishing and lapping operation in order to minimize the forming of any oxides, etc. The n-type metallurgy AuGeNi was vapor deposited on the entire surface with the wafer temperature elevated to 185° C. Evacuated to approximately 10^{-5} torr, a thickness of 2200Å of AuGeNi was deposited on each wafer. Photo resist techniques were then used with a stripe mask pattern to define the n-type ohmic contacts. A subtractive etch process was then used to remove all contact material not required.

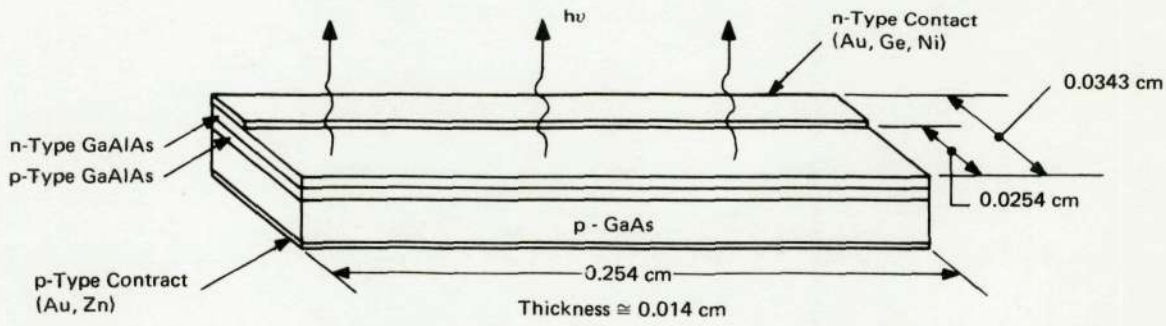

A - Schematic

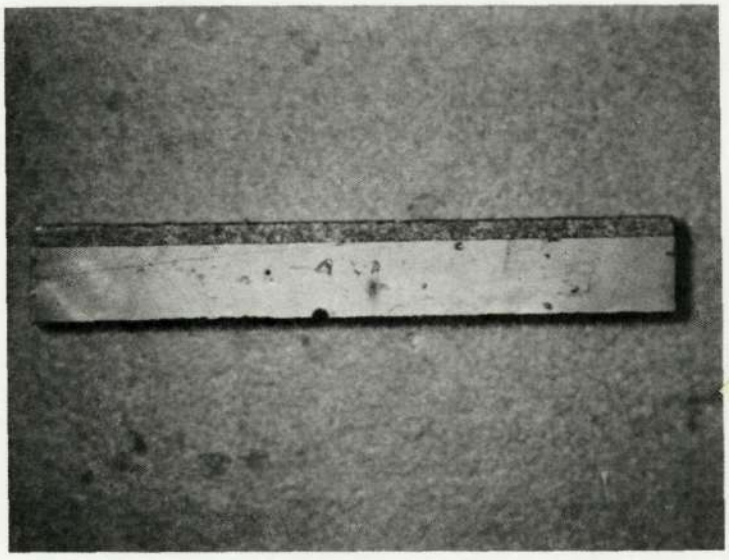

B - Photograph of LED

Figure 2-10. Basic GaAlAs Array Element

This page is reproduced at the back of the report by a different reproduction method to provide better detail.

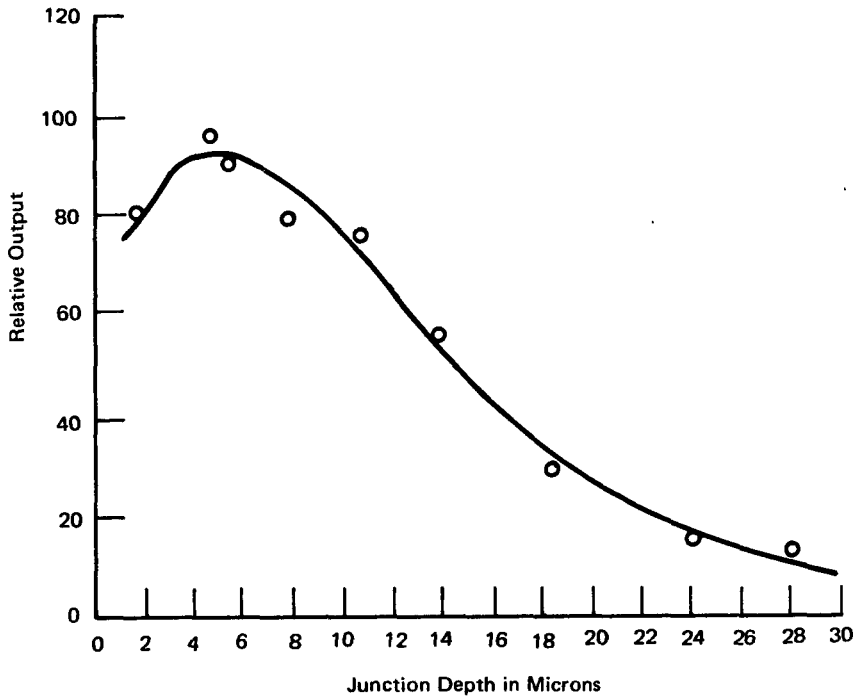

Figure 2-11. Relative Output vs Thickness

p-type AuZn material was then vapor deposited on the reverse side (GaAs) of each wafer in the same manner. However, the substrate temperature was held at 250° C and the thickness of metallurgy generally averaged 1100Å. A sintering operation for both the AuZn and AuGeNi metallurgy was then carried out in a 480° C furnace for 10 minutes, while in a forming gas atmosphere. Typical contact resistance is shown in the following Table 2-2.

Table 2-2. Contact Resistance

Material	Doping	Carrier Concentration (atoms/CC)	Resistance (Ω-cm^2)
n-GaAlAs	Te	$7\text{-}8 \times 10^{18}$	2×10^{-6}
p-GaAs	Zn	$2\text{-}5 \times 10^{18}$	2×10^{-5}

2. 2. 3 Diode Fabrication

The final step in wafer processing is the string saw dicing of the wafer into individual diodes measuring 0. 0343 x 0. 254 cm^2. Prior to cutting, the wafer is cemented to a glass slide and its surface is covered using glycol phothalate. This protects against the aluminum oxide abrasive used in the cutting-slicing. A 0. 0127 cm tungsten string saw blade cuts and steps horizontally first and then vertically as shown in Figure 2-12 to isolate each diode. Prior to dissolving the glycol phothalate with acetone, the diodes are etched along their perimeter to remove some of the crystal damage that occurs during cutting.

2. 2. 4 Diode Testing and Selection Method

Each LED chip was tested and evaluated to determine its individual characteristics prior to considering its usage in the final pumping array. In this manner, all 20 diodes for each array are selected, and the results of total diode data provide feedback information on each particular wafers yield. Table 2-3 shows the sequences of diode inspection and measurement.

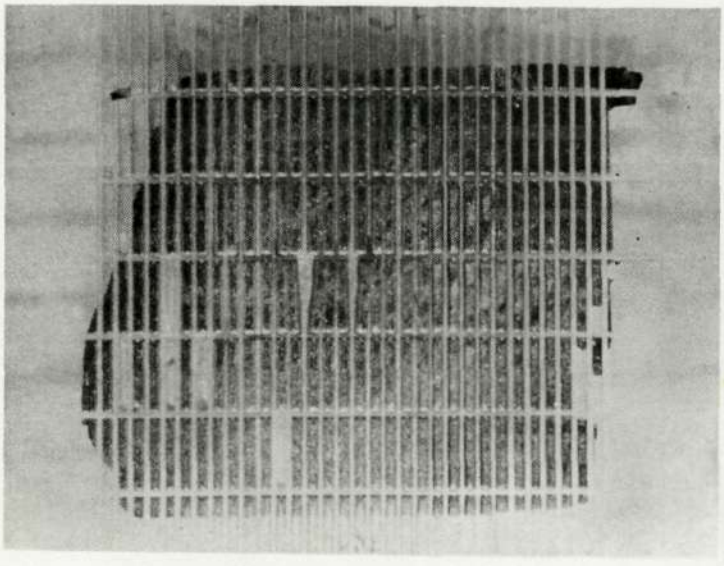

This page is reproduced at the back of the report by a different reproduction method to provide better detail.

Figure 2-12. GaAlAs Wafer Just After String Saw Cut Into Discrete Diodes

Table 2-3. LED Tests at Chip Level

Testing Sequence	Particular Test	Parameter Evaluated	Method
1	Physical examination	Screens out cracks, chips surface discontinuity	Visual inspection
2	Electrical input characteristic	I-V, series resistance	Curve tracer
3	Output radiation	Measures magnitude of power output	Solar cell probe
4	Visual radiation	Determination of radiation uniformity	IR image converter

In order to measure the relative power output of each chip a small probe was constructed consisting of two needle contacts and a glass enclosed silicon solar cell (see Figure 2-13). The needle tips were spaced to contact each chip one-third of the way in from either side of the n-type stripe contact, thereby distributing the forward current of the device more evenly than if just a single point were used. The silicon cell (10 ohm load resistor) was fastened at a fixed distance from the probe tips and its relative output correlated against exact power levels made, using test diodes enclosed in an integrating sphere. Initially, a similar probing technique using a half silvered mirror over a solar cell was used; however, minor scratching of the mirror surface introduced errors and therefore the second technique was used. The diodes were driven at a constant current level of fifty milliamperes and were sorted according to their relative output as observed by a microvoltmeter across the cells load resistor.

Table 2-4 shows an average statistical distribution of diodes from a typical LPE wafer following the testing shown in Table 2-3.

2.2.5 LED Electro Optical Performance

Table 2-5 is a summary of the characteristics GaAlAs LED.

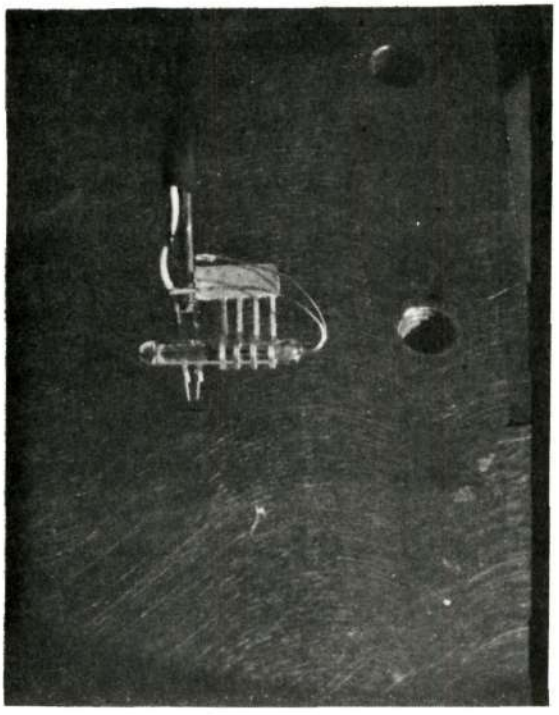

Figure 2-13. Probe used to Measure Relative Output of LEDs at the Chip Level

Table 2-4. Typical Wafer Yield Summary

Parameter	Value
Average wafer size	2.03 x 2.03 cm^2
Typical number of LEDs (0.0343 x 0.254 cm^2)	275
After mechanical defect sort	200
After IV/power output sort (N_{ext} 1.1% into air)	50
Average number of arrays per wafer	2.5

Table 2-5. GaAlAs LED Summary*

Parameter	Typical Value
Peak emission wavelength	8070 Å
Emission half width (50% points)	250 Å
Power output @ 1 amp.	35 mW
Forward voltage drop @ 1 ampere	1.80 V
External quantum efficiency (into air)	1.10%
Dynamic resistance	0.14Ω
Chip size: 0.0343 x 0.254 cm^2, grown on GaAs	
*Measurements at 25° C	

Following a preliminary E-O inspection, several typical diodes from each LPE grown wafer are mounted on TO46 headers and tested for emission wavelength and efficiency. A test diode is shown in Figure 2-14. In this way, the diode, as well as the relative reading of the solar cell probe, are checked before all the chips are examined. External quantum efficiency defined as the ratio of the number of photons per second, N_p emitted from the LED to the number of charge carriers per second N_e, injected across the pn junction:

$$N_{ext} = \frac{N_p}{N_e} = \frac{KI_c}{I_f}$$

where:

I_c = Photo current generated by a silicon integrating sphere

K = Constant that accounts for losses in the above cell

I_f = Forward Current of the LED.

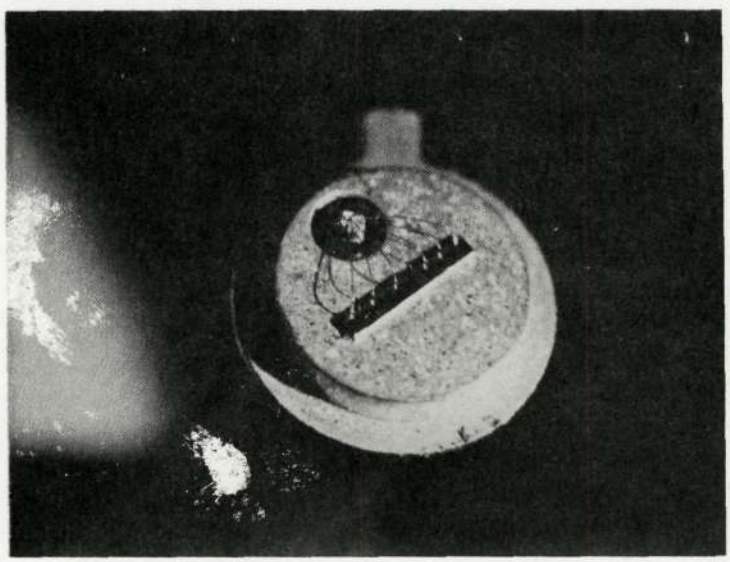

This page is reproduced at the back of the report by a different reproduction method to provide better detail.

Figure 2-14. LED Chip Mounted on T046 Header for Measurement Characteristics

Diode external quantum efficiency is measured at a forward current I_f of 400 milliamperes. All diodes selected for the final array assembly met or exceeded 1.1 percent with maximums being 1.6 percent. A typical diode current-voltage characteristic curve is shown in Figure 2-15. Figure 2-16 shows a plot of power output as a function of forward current and Figure 2-17 shows the relative light output and forward current with respect to forward voltage.

2.2.6 Conclusions

The power output from individual diodes showed their performance to be essentially linear with current up to the point of an appreciable junction-temperature rise. A variety of measurement techniques have shown that a forward current of one ampere produces a net junction-temperature rise of 16° C above ambient (more details on operating temperature in subsection 2.3.1). The curve shown in Figure 2-18 is a normalized plot of power output per cm^2 as a function of current density (A/cm^2) and depicts the output characteristics of this diode geometry.

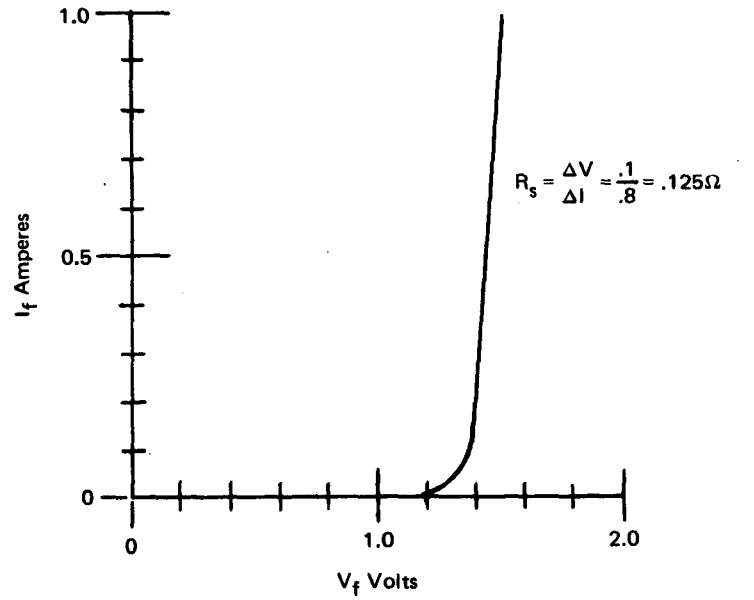

Figure 2-15. Current-Voltage Characteristics of a Typical GaAlAs LED

In retrospect, the hand selecting of 20 diodes for each array built was a somewhat tedious operation requiring many hours of chip sorting by the tests mentioned in subsection 2.2.4. However, this careful selection of diodes resulted in a 100 percent yield on final array inspection with uniform radiation output and consistent I-V characteristics from array to array.

2.3 FABRICATION OF DIODES ARRAYS

2.3.1 Hybrid Circuit Board

An array circuit configuration was developed to permit the 20 GaAlAs diodes in each array to be aligned and electrically connected in series. Since the input power into each array was typically 28 watts, prime consideration was given to the thermal conductivity of the circuit board material. To effectively transfer heat from these diodes to an appropriate heat sink, the boards thermal conductivity must be high. Table 2-6 shows a comparison of materials considered. Berlox was chosen as the best available material and blank boards measuring 7.62 x 10.3 cm^2.

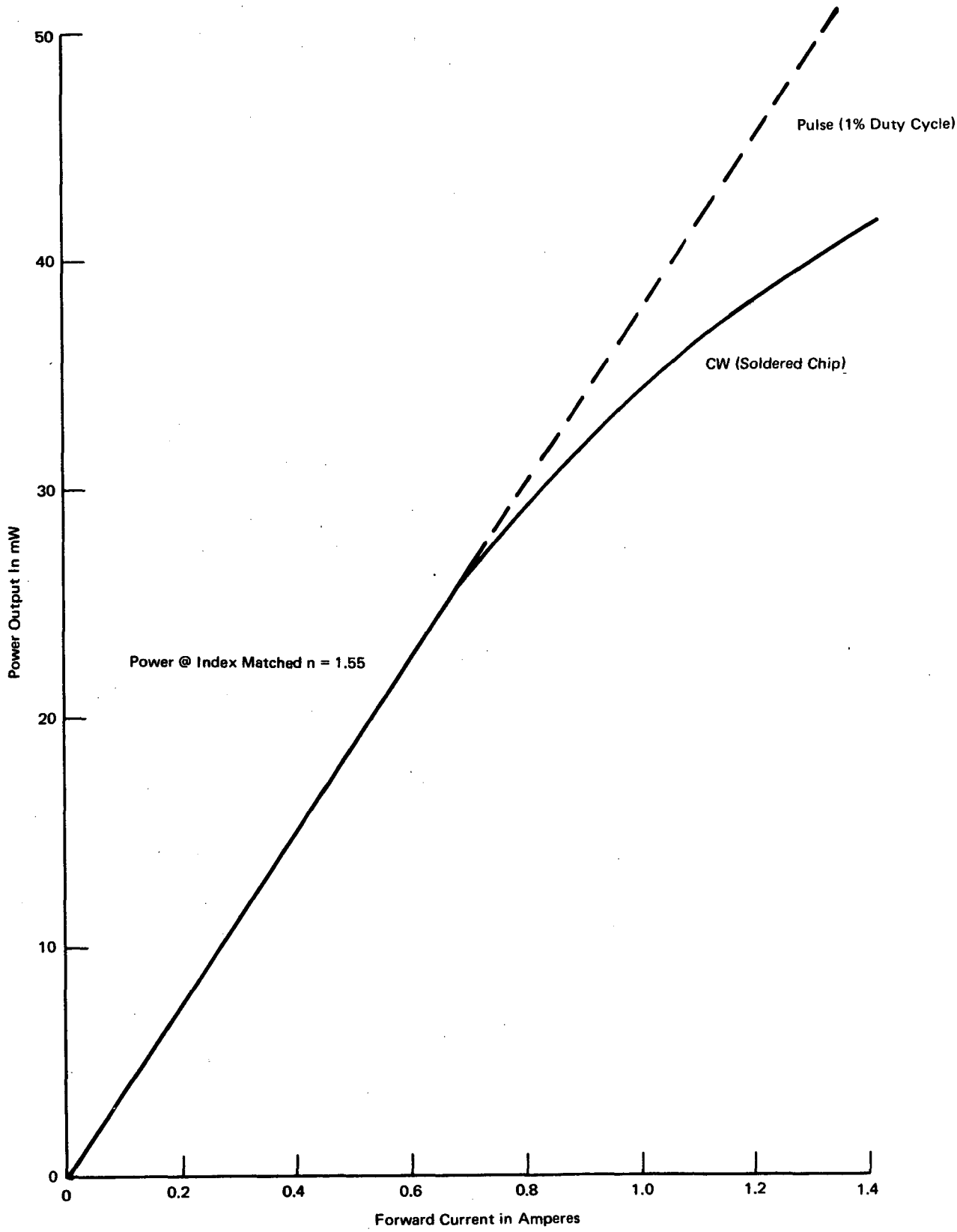

Figure 2-16. Power Output Plotted at a Function of Forward Current for a Single LED

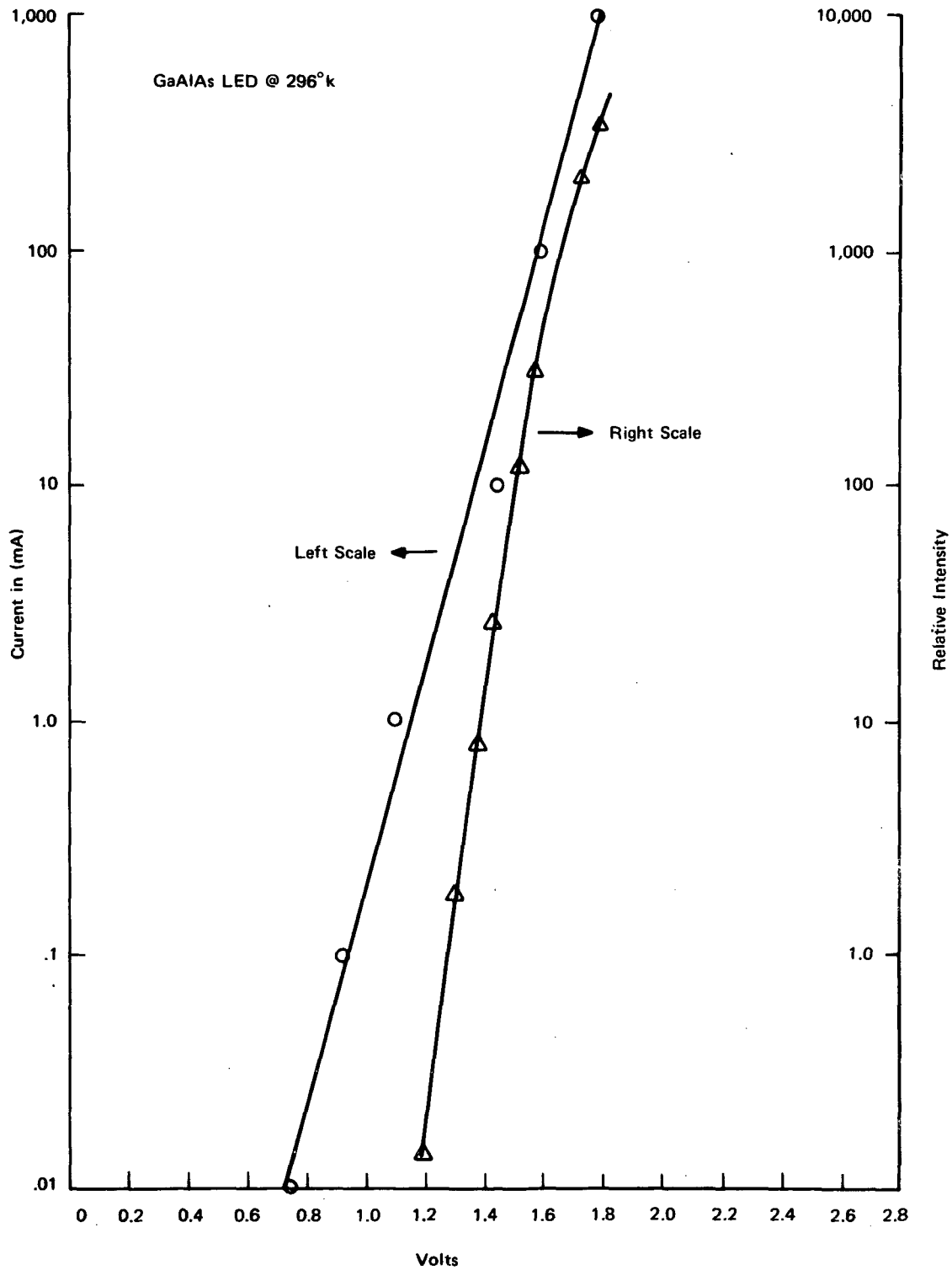

Figure 2-17. Light Output and Current versus Voltage for a Typical LED

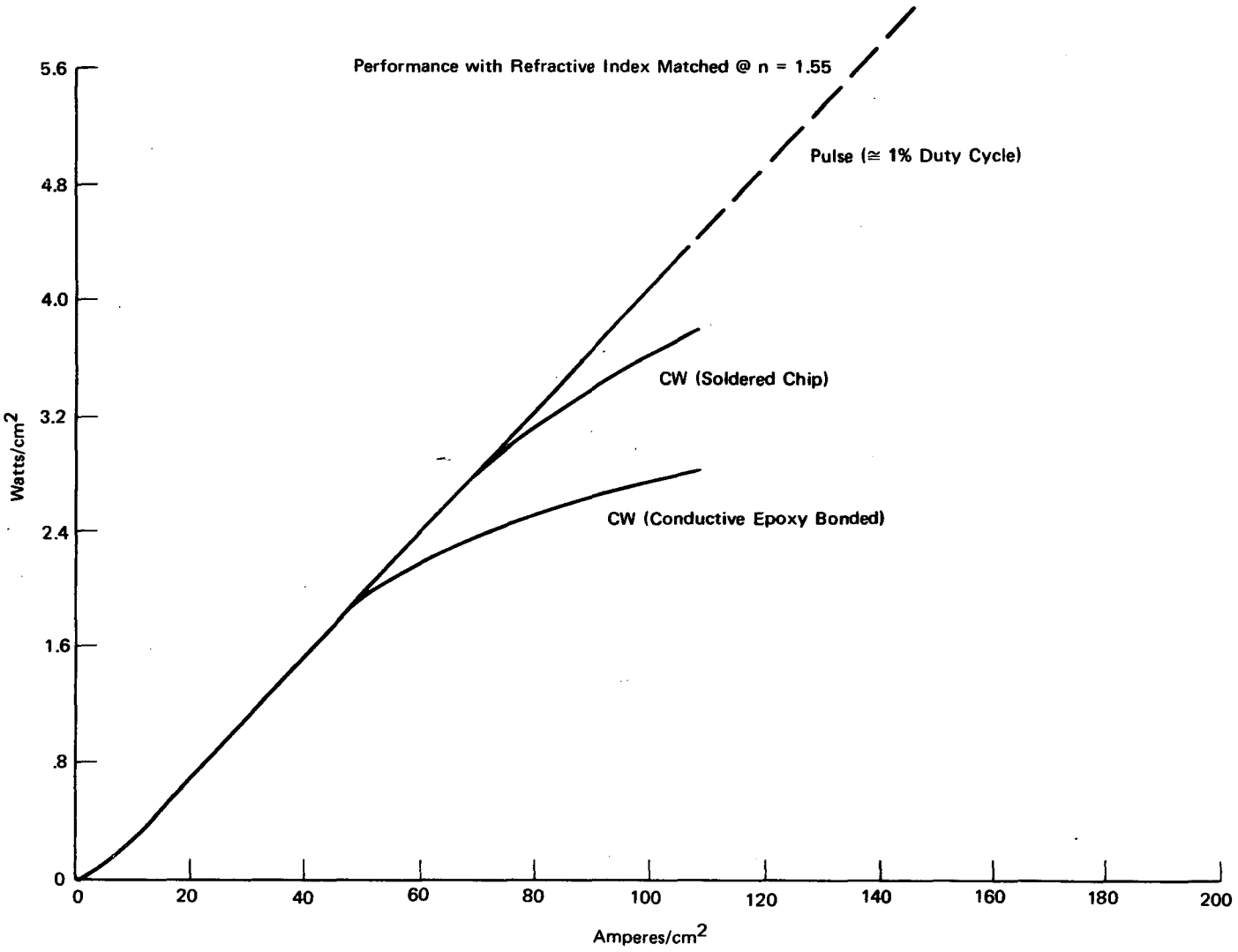

Figure 2-18. Normalized Power Output versus Current Density for the GaAlAs LED

Table 2-6. Comparison of Material Properties for Array Circuit Board

Material	Thermal Conductivity Watts/cm^2 sec °C — cm	Dielectric Constant	Thermal Expansion % Expansion @ 800°C
Alumina	0.294	8.5 - 10.0	0.58
Aluminum	2.08	---	---
Berlox*	2.42	6.0 - 6.5	0.68
Copper	3.81	---	1.60

*Registered trade name of National Beryllia Corp.

These blank ceramic boards were then sputtered with chrome, nickel, gold and then electroplated with approximately 5.08 x 10^{-4} cm of gold. A mask was designed that permitted the diodes to be placed end to end with a 0.0254 cm gap between units. This pattern, in addition to providing electrical connections to each diode, also served to establish the exact location for placement of the diode chips later in the assembly process. Conventional photolithographic techniques are then used with a positive resistance to subtractively etch off all metallurgy not required for the circuit pattern. Figure 2-19 shows a completed board prior to being diamond sawed into discrete arrays.

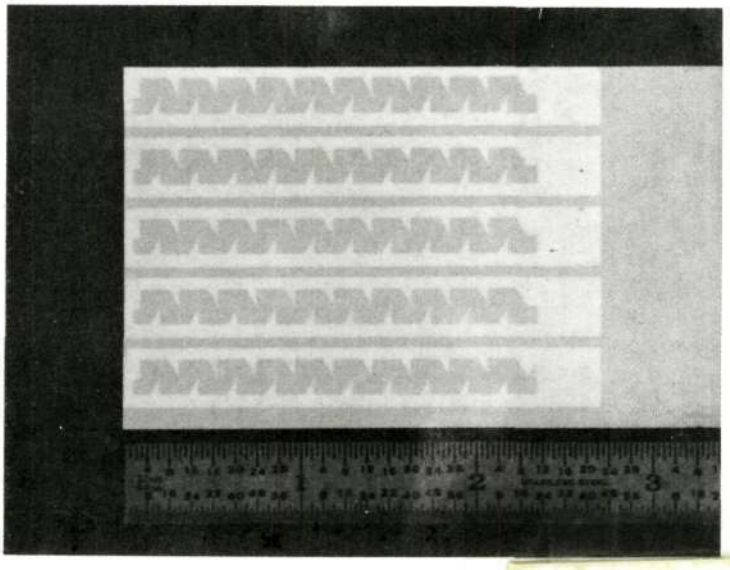

This page is reproduced at the back of the report by a different reproduction method to provide better detail.

Figure 2-19. Completed Circuit Board

Following cutting the circuit boards, the surface areas outside the diode contacting area were covered using electroplating masking tape. This effectively protects the outlying metallurgy areas during an additional 60/40 lead tin electroplating operation, which plates the diode pad placement areas with approximately a 1 mil thickness of solder. This solder will be reflowed during the chip bonding operation (see 2.3.2 Assembly Procedure).

2.3.2 Assembly Procedure

Individual LED elements are optically aligned as they are placed on the connection pads of the completed hybrid circuit board. A flux, Kester 196, is applied to wet the solder pad and provide device anchoring as each chip is positioned and aligned through a microscope. Following the completed positioning of all chips, the entire board is placed in a uniform temperature oven at 300°C for ten minutes. This temperature and flux combination has resulted in practically zero chip movement during the solder reflow which occurs simultaneously for all diodes during this baking cycle. Several different fluxes were tried but judged unacceptable because of chip movement apparently resulting from rapid evaporation of the solvent.

Following this operation, all the anode sides (+) of the diodes have been firmly soldered to the hybrid circuit board. The remaining cathode connections to the strip metallurgy on each diode is accomplished using a nail head bonding machine. Nine separate thermal compression bonds are made on each LED from the cathode ohmic contact to the adjacent metallurgical pad on the circuit board, as shown in Figure 2-20. The wire, 0.00254 cm diameter gold, has been shown experimentally to withstand 400 mA per connection. Figure 2-21 shows a completed array.

2.3.3 Array Thermal Measurements

A series of experiments were conducted to determine the approximate junction temperature of the LEDs when operating at a forward current of one ampere. Three separate techniques were employed: changes in the forward voltage as a result of heating; shift in the peak emission wavelength with temperature; and actual diode surface temperature measurements using a micro sized thermocouple on the diode and related surfaces. Results are shown in the right-hand column of Table 2-7.

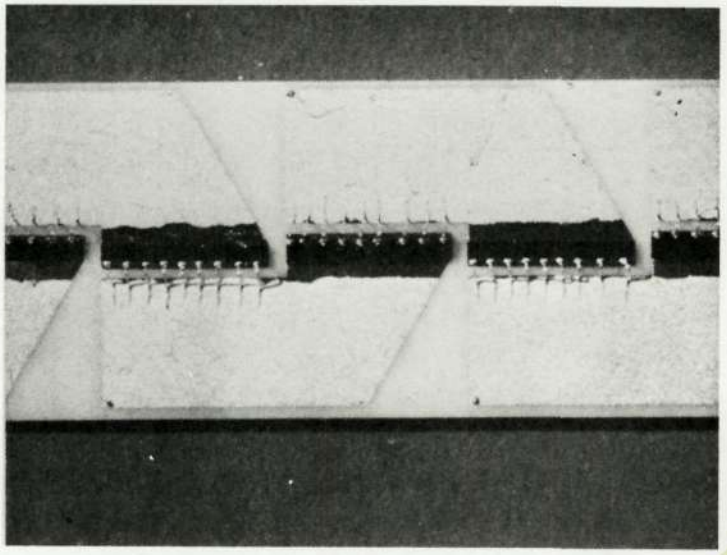

Figure 2-20. Diode Elements Connected in Series by Combination of Solder Reflow and Nail Head Bonding

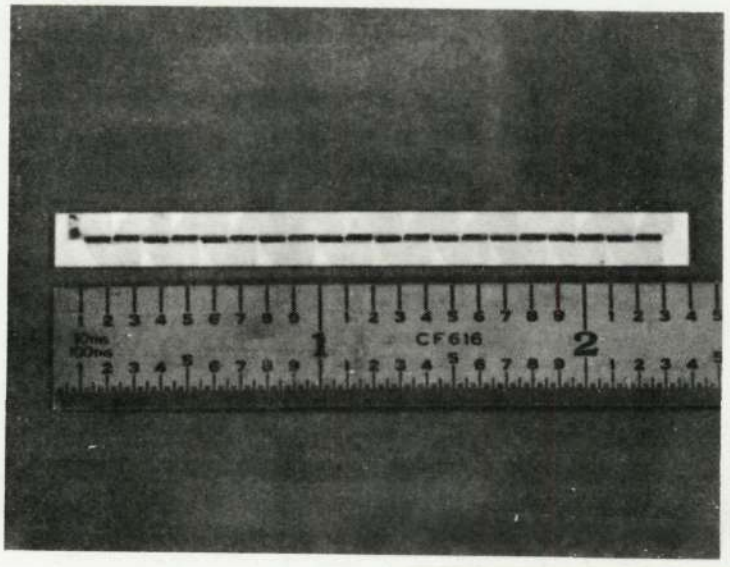

Figure 2-21. A Completed Array

Table 2-7. Parameter Changes with Temperature

Technique Used	Sample Device	Forward Voltage @ 1A Pulse	CW	ΔV Volts	Δλ Angstroms	Junction Rise Above Ambient °C
1	Array #4	28.5	28.0	0.50	---	16.5
1,2	Array #5	29.6	29.0	0.60	47	20.5, 23.0
1	Diode (PL-66)	2.060	2.035	0.025	---	16.5

Temperature Coefficient = 1.5 mV/°C

Figure 2-22 shows the temperatures measured on the surface (3) of the diode and on the hybrid board and heat sink using a 0.0127 cm diameter iron constantine thermocouple after 20 minutes at a continuous current of one ampere. In summary, all measurement data indicates that the temperature rises between 16.5 to 20°C for a forward current of one ampere. This small rise is attributed to the excellent overall thermal conductivity of the laminated structure.

2.3.4 Life Testing

Life testing was started on two GaAlAs LED arrays to determine the aging characteristics of these pumping sources. Basically, two operating characteristics were being closely monitored: the slope or rate of change in relative output with time, and the change, if any, in peak emission wavelength and/or spectral width, which would indicate junction diffusion taking place. The operating current in each array is one ampere or a current density of 115 amperes/cm^2.

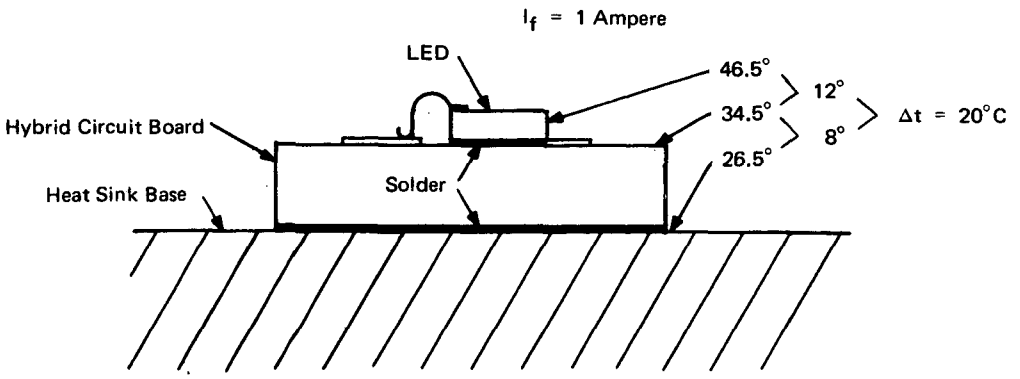

Figure 2-22. Thermal Profile as Measured Using a 0.0127 Centimeter Thermocouple

Two transistor constant current sources were constructed to maintain this current level throughout the testing period (see Figure 2-23). A silicon photodiode (SGD-100A) mounted approximately two inches above each enclosed array monitors the respective radiation output level. This output is displayed on a digital voltmeter that is switched between detectors.

Figure 2-24 shows the results at the end of 4300 hours of CW operation; arrays 5 and 7 were operating at 70 and 75 percent respectively of their initial output. Monochrometer (MOD. 99G P.E.) scans made periodically to monitor emission spectrum have shown a negligible change in spectral characteristics. Figure 2-25 shows the emitted spectrum of the 20 diodes making up a typical array.

2.4 OPERATING CHARACTERISTICS OF THE DIODE ARRAY

The properties of GaAlAs diodes are very sensitive to the temperature variation. In order to obtain meaningful data of optical power efficiency, emission spectrum, and current-voltage relationship, it is vital to obtain accurate temperature information in the p-n junction and maintain it constantly during the measurement. In practice, it is impossible to measure junction temperature directly. Furthermore, the thermal conductivity of a GaAlAs diode is about five times less than that of GaAs [2]. There is always a problem of conducting heat out from the p-n junction in CW operation. Therefore, most of our measurements of diode characteristics are made in pulse mode with one percent duty cycle.

Thermal analysis of continuously operating GaAlAs diode arrays indicated that the temperature difference between the p-n junction and copper heat sink was 16.2° centigrade at 115 A cm^{-2} current density (corresponding to 1A, 28.5W electrical input power). Experimental data indicated: from wavelength shift, a 16°C difference between the p-n junction and heat sink under the same operating condition. Thus, the measured heat sink temperature is quite close to the actual temperature of the p-n junctions when the diode array is operated in one percent duty cycle at 115 A cm^{-2} current density.

2.4.1 Spectrum of the GaAlAs Diode Array

The output energy distribution of GaAlAs diodes depends on the profile of aluminum content, p-n junction width and operating temperature. In a diode array, the energy distribution is even broader than in an individual diode due to

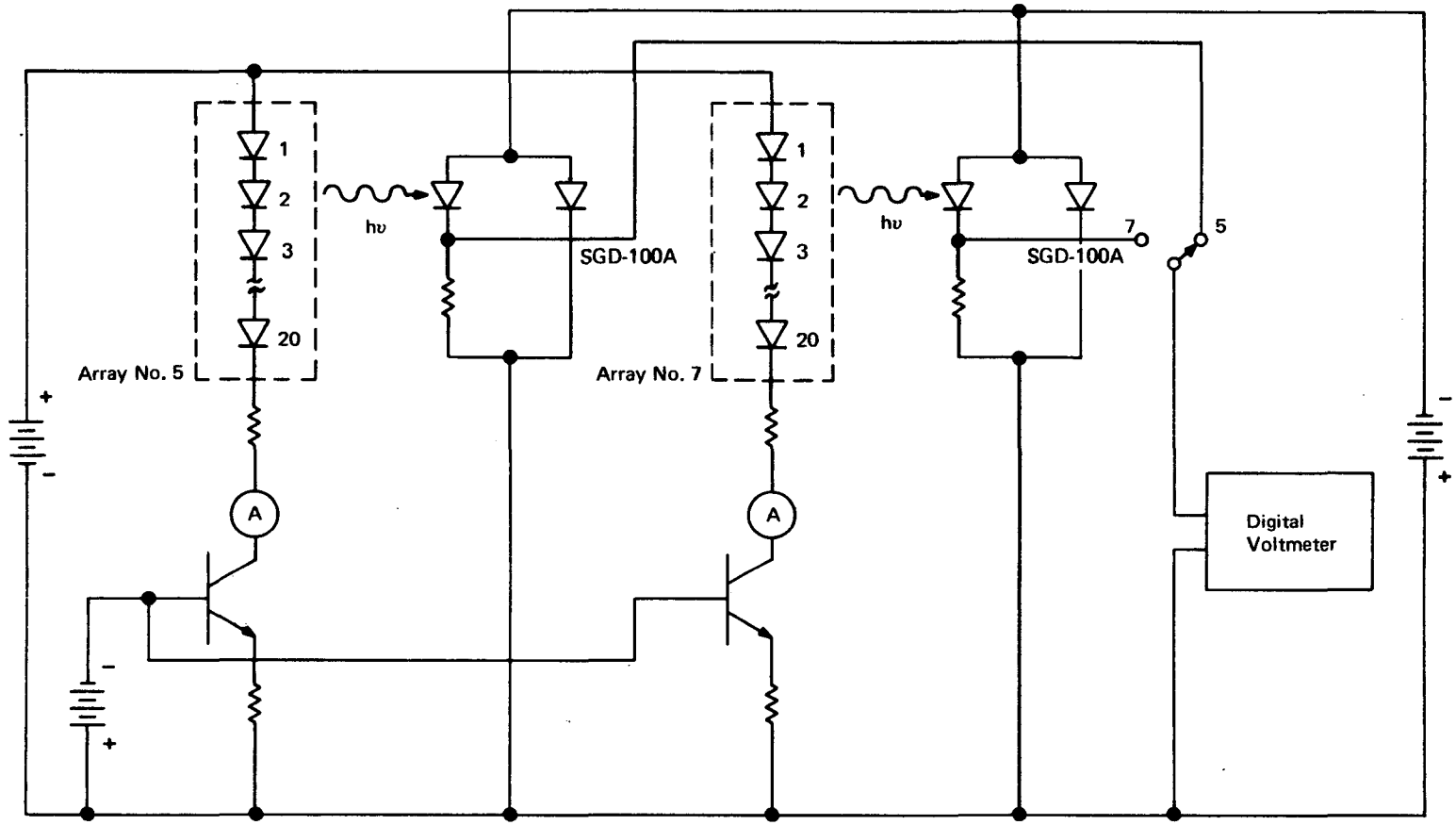

Figure 2-23. Circuit for Life Testing Two Nd:YAG Pumping LED Arrays

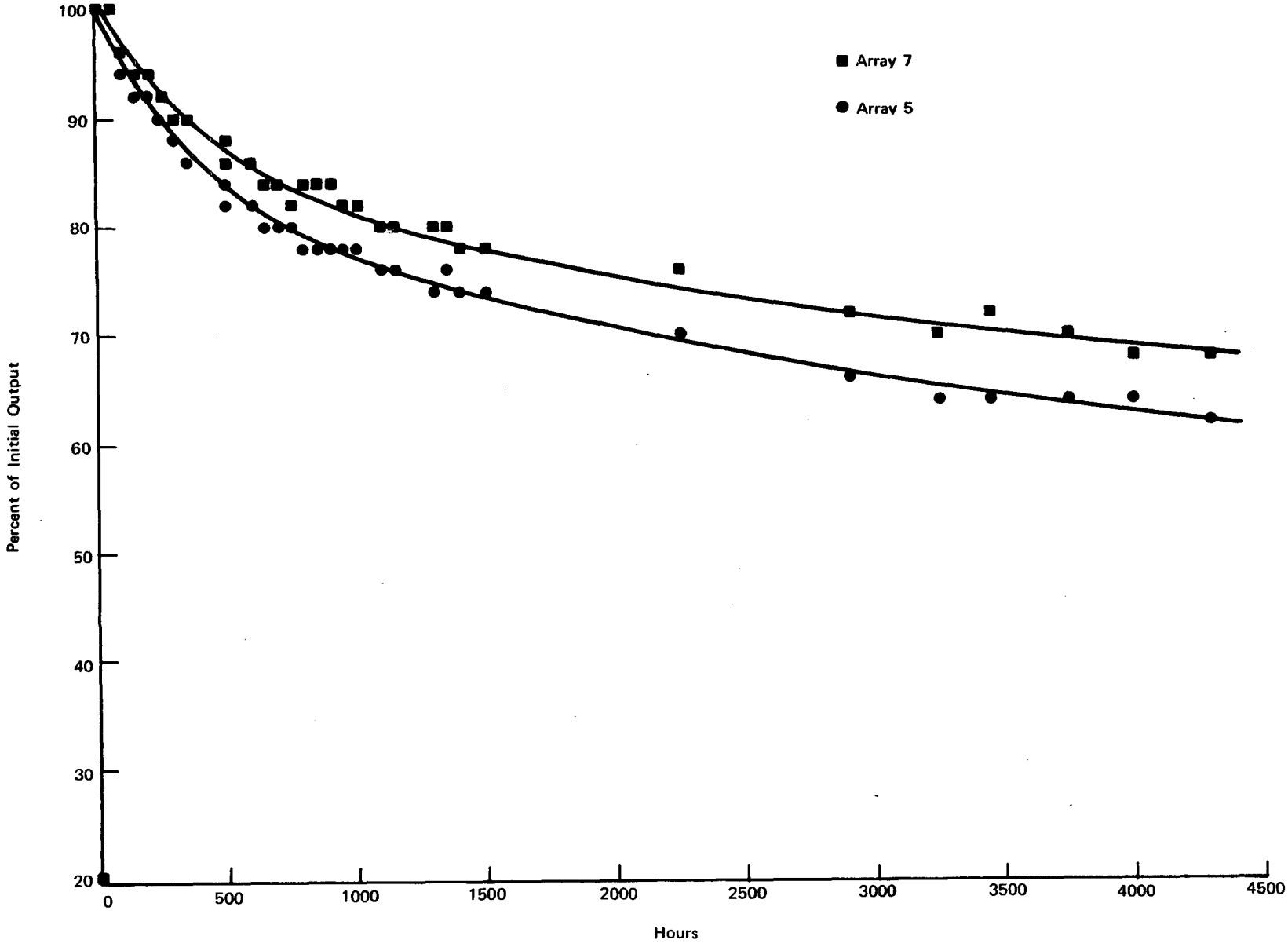

Figure 2-24. Aging Characteristics of Two Pumping Arrays

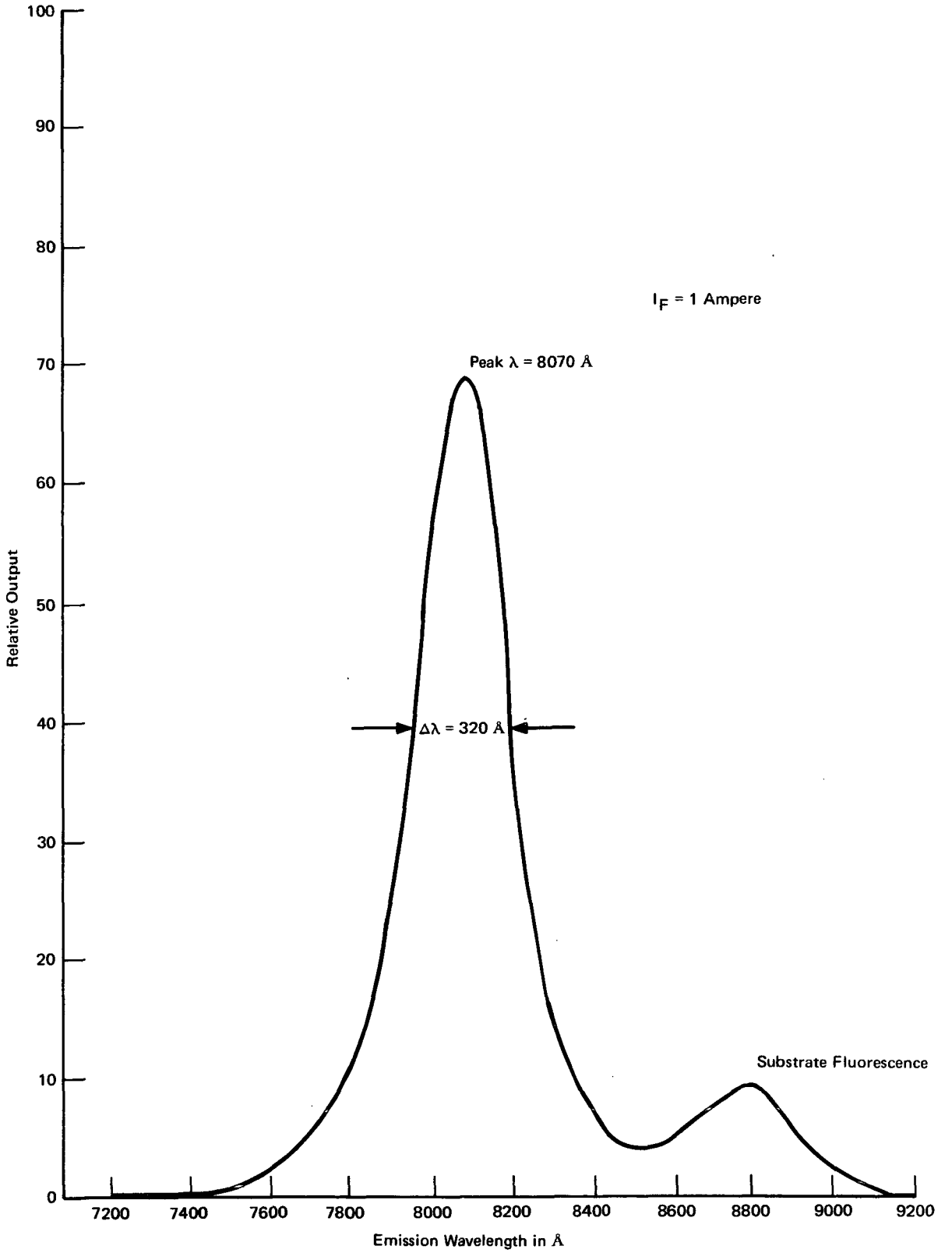

Figure 2-25. Emission Spectrum for a Typical 20 Element Array

the energy gap variation of each diode and dissimilarity in the heat conduction of various diodes to the heat sink interfaces.

From the spectral measurement, we have determined the peak emission wavelength and full linewidth at half intensity as a function of operating temperature. A Jarrell Ash one meter combination scanning spectrograph was used with an RCA 7102 S1 response, cooled photomultiplier, and combined recording system. The diode array was excited by one ampere current with 500 microseconds rectangular pulsewidth at 20 Hz repetition rate. The light output from the diode array was reflected by a plane mirror to the 50 μm wide entrance slit of the spectrograph. The wavelength marker of the scanning spectrograph was calibrated with the neon spectral lamp. Diode temperature was controlled by three Borg-Warner Model 950-71 thermoelectric modules and monitored by a copper constantan thermocouple wire attached to the diode heat sink. The spectral data plotted as function of temperature are shown in Figure 2-26. The peak emission wavelength of the GaAlAs diode array shifts 3.1Å per degree centigrade and the linewidth is 300Å at room temperature. In CW operation, the spectra are different from pulse operation because there is a larger temperature difference between the heat sink and the p-n junction. By comparison of CW and pulsed spectral data, one can determine the average junction temperature of the diode array in CW operation. Table 2-8 shows the CW operation characteristics of the GaAlAs diode array.

2.4.2 Temperature Dependence of Diode Efficiency and Current Voltage Relationship

The emission efficiency of GaAlAs diodes decreases with increasing temperature. This is illustrated by the relative light intensity curves in Figure 2-27. The values in the figure do not represent values for GaAlAs LED. Each diode array has its own special values depending on the material preparation. From the above experimental results, the degradation of diode emission efficiency near room temperature is approximately 0.615 percent per degree of temperature increase at 54 watts electrical input power ($\sim$ 200A/cm^2). The light intensities of CW operation diode arrays were measured and found to be much below that for pulse operation. The difference was due to the temperature rise in the p-n junction while the diode operated in CW mode. For example, the CW light intensity dropped 19.7 percent from the pulsed value of curve A in Figure 2-11 at 54 watts input power; using 0.615 percent degradation per degree of temperature rise, the calculated temperature increase was 32°C in the p-n junction; this agrees very well with previous spectral data.

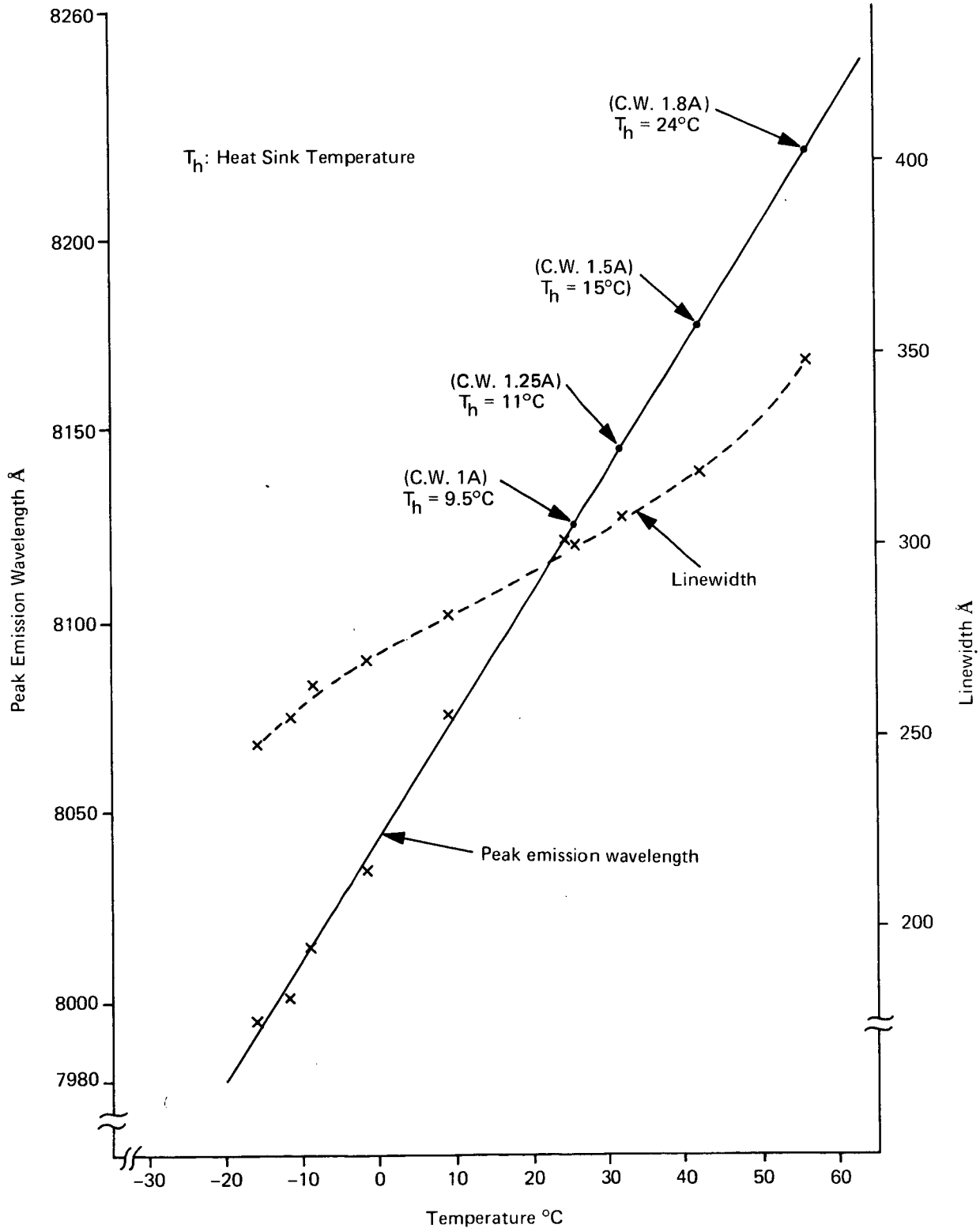

Figure 2-26. Emission Spectrum of a $Ga_{1-x}Al_xAs$ Diode Array

Table 2-8. CW Operation Characteristics of the GaAlAs Diode Array

Input Power Watts	Peak Wavelength Å	Linewidth Å	Temperature of the Heat Sink	Junction Temperature of Diode Array
28.5	8129.0	300	9.5°C	25.5°C
36.2	8145.0	307	11°C	32°C
44.2	8177.2	319	15.1°C	42°C
54.0	8222.5	348	24°C	56°C

The current voltage relationship of the diode has the usual exponential dependence on the applied forward voltage:

$$I = I_s \exp (qV/nkT)$$

where q is the electronic charge (1.6×10^{-19} coulomb), T is the absolute temperature in Kelvin, k is the Boltzmann's constant (1.38×10^{-23} joules/°k), I_S is the saturation current and n is a constant with n=1 for diffusion current to recombination of injected carriers in the junction [3] or n = 2 for current due to recombination in the space charge region via deep traps [4]. The dominant current at low current operation is due to space charge recombination. At high current level, the dominant current is due to recombination of injected carriers in the junction region. In our operation, the diffusion current is dominant, thus n = 1. The current voltage characteristics for the diode array were measured under pulse conditions at 297°K and 251°K. Typical I-V curves of the GaAlAs diode array are shown in Figure 2-28. From the forward slopes of the I-V curves, the series resistances of the whole array were 2.62 ohms at 24°C and 3 ohms at -22°C. At two amperes operating current level, the forward voltage decreases 90 millivolts per degree centigrade while the temperature is increasing.

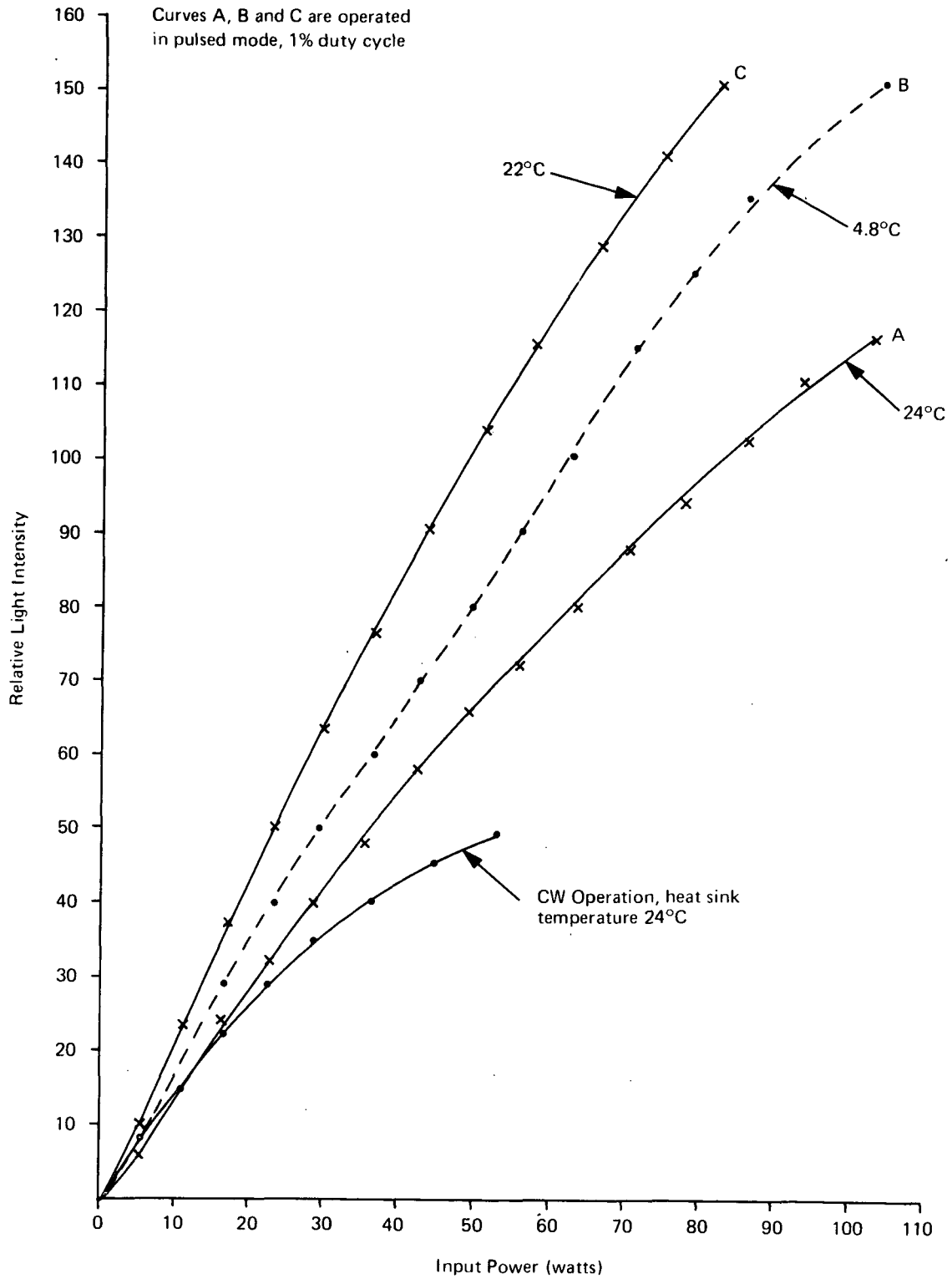

Figure 2-27. Relative Efficiency of GaAlAs Diode Array

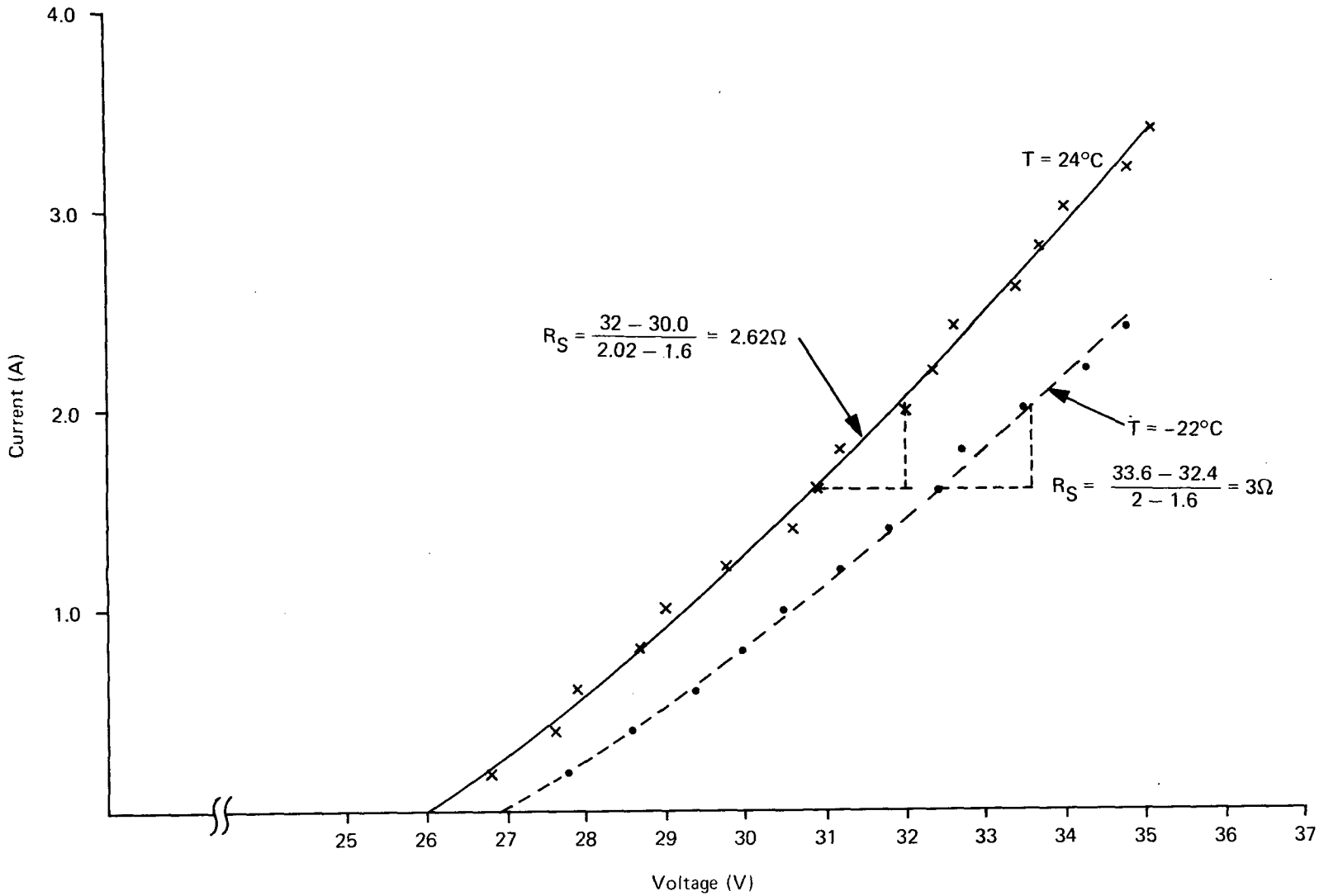

Figure 2-28. Current-Voltage Relationship of GaAlAs Diode Array

Section 3. CHARACTERISTICS OF Nd: YAG LASERS

3.1 GENERAL PROPERTIES OF Nd:YAG CRYSTALS

Neodymium-doped Yttrium Aluminum Garnet (Nd:YAG) is perhaps the most practical and widely used rare-earth doped crystalline laser. It has been extensively developed to optimize efficiency and other pertinent laser parameters. In addition, the strongest absorption band near 8100 Å (ground state to $^4F_{5/2}$ and $^2H_{9/2}$ transition [5] can be pumped by recently developed ternary alloy light emitting diodes such as gallium aluminum arsenide and gallium arsenide phosphide. The coherent emission at 1.06 microns is accessible to fast, relatively efficient detection. If using a good quality non-linear crystal, frequency doubling to 5300Å can be achieved with high conversion efficiency[6]. Nd:YAG is a four-level laser system with terminal states ($^4I_{11/2}$) of the laser transition 2000cm^{-1} above the ground state[5]. The radiative lifetime of upper laser states is 230 microseconds [7], and the lifetime of terminal states is ~100 ns[8]. Thus, the population density of terminal states is thermalized and relatively small compared to the ground state Nd^{+3} density even at room temperature; therefore, the threshold is low and easy to obtain. The laser transition has two different emission wavelengths depending on laser rod temperature. Below 222°K, the laser transition is from the lower crystal field level of the $^4F_{3/2}$ state to the lowest crystal field component of the $^4I_{11/2}$ state (line 6). For specificity the spectrum will be labeled with the transition numbers given in Reference 5. The emission wavelength is 10610Å at 77°K. Above 222°K, the laser emission is due to two combined transitions of nearby emission wavelengths; one from the upper level of $^4F_{3/2}$ to the third level of the $^4I_{11/2}$ state (line 5) and one from the lower level of the $^4F_{3/2}$ state to the second level of the $^4I_{11/2}$ state (line 4). The emission wavelength is 10640Å at 300°K[9].

The spectroscopic data of Nd^{3+} in YAG are contained in reference papers[5] and [9]. Nonetheless, accurate information related to the line width and peak emission wavelength shift of the combined transition (lines 4 and 5) near room temperature are not available from the above references. In order to understand clearly the behavior of a Nd:YAG laser near room temperature, the temperature dependence of the fluorescence has been measured in the temperature range from 240°K to 294°K. The Jarrell Ash one meter combination

scanning spectrograph was used with cooled S1 response photomultiplier. The wavelength calibration of the spectrograph was corrected with higher order neon discharge reference lines. The Nd:YAG rod with antireflection coating on the output end was pumped by a GaAlAs diode array with peak emission wavelength near 8100Å. The temperature of the rod was controlled by the thermoelectric cooler and monitored by a copper constantan thermocouple. The spectra relevant to laser transitions (line 6 and combined lines 4 and 5) are shown in Figure 3-1. Note that the full line width at half intensity of the combined transitions of lines (4) and (5) is almost constant at about 7.9Å in the temperature range from 240°K to 294°K. The shift of peak emission wavelength is relatively small at only 0.06Å/°C. On the other hand, the line width of line (6) due to the single transition has regular temperature dependence.

A detailed investigation of the absorption band of Nd:YAG from ground state to $^4F_{5/2}$ and $^2H_{9/2}$ manifold states has been undertaken in order to calculate the optical coupling efficiency of the GaAlAs diode pumping source array. A Nd:YAG sample of $1cm^2$ by 1.5mm thick was used for measuring optical transmission with Cary Spectrophotometer. The measured optical density of Nd:YAG from 7900Å to 8300Å is shown in Figure 3-2. This complex absorption band will be used to compare various emission spectra of GaAlAs diode arrays for determining the best optical coupling condition.

3.2 THEORETICAL ANALYSIS OF THE DIODE PUMPED Nd:YAG LASER

The dynamic behavior of Nd:YAG lasers can be described by the single mode nonlinear rate equations [10, 11, 12]. Special emphasis will be placed on the operation near room temperature. The effect of temperature on the laser parameters is included in the calculation of the population density of lower laser states, Boltzmann factor and stimulated cross section. This approach has the advantage of simplicity while still accurately describing a 4-level laser system.

Analytical results are expressed by relating excitation rate, pumping threshold, laser output power, and optimum mirror transmission. By direct modulation of diode input current, the characteristics of transient phenomena can be related to the optical pumping rate and cavity loss. Maximum modulation depth of laser output intensity will depend on the frequency of relaxation oscillation and modulation frequency. A comparison of the theory with measured Nd:YAG laser performance will be discussed in the section on experimental results.

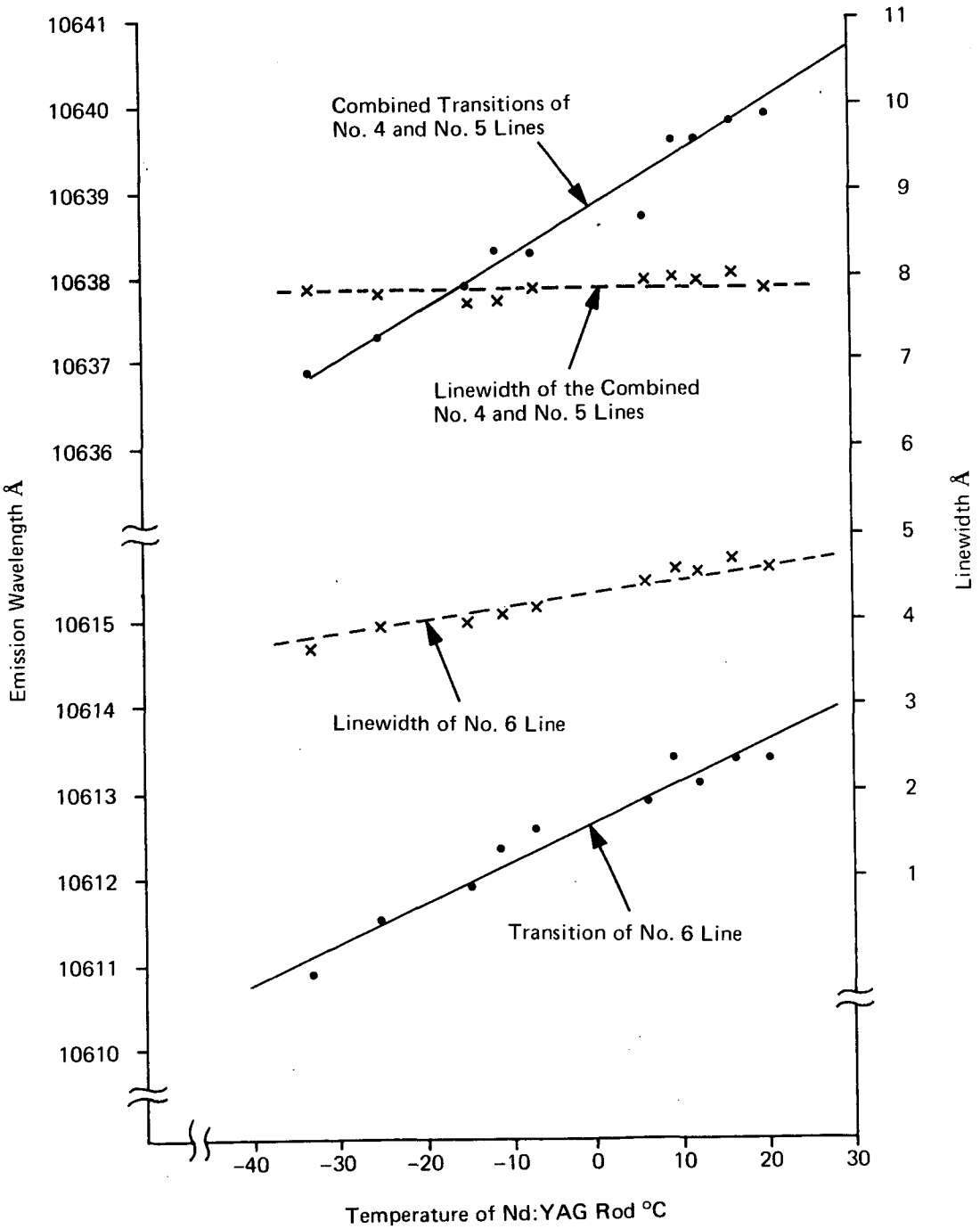

Figure 3-1. Fluorescence of Nd:YAG

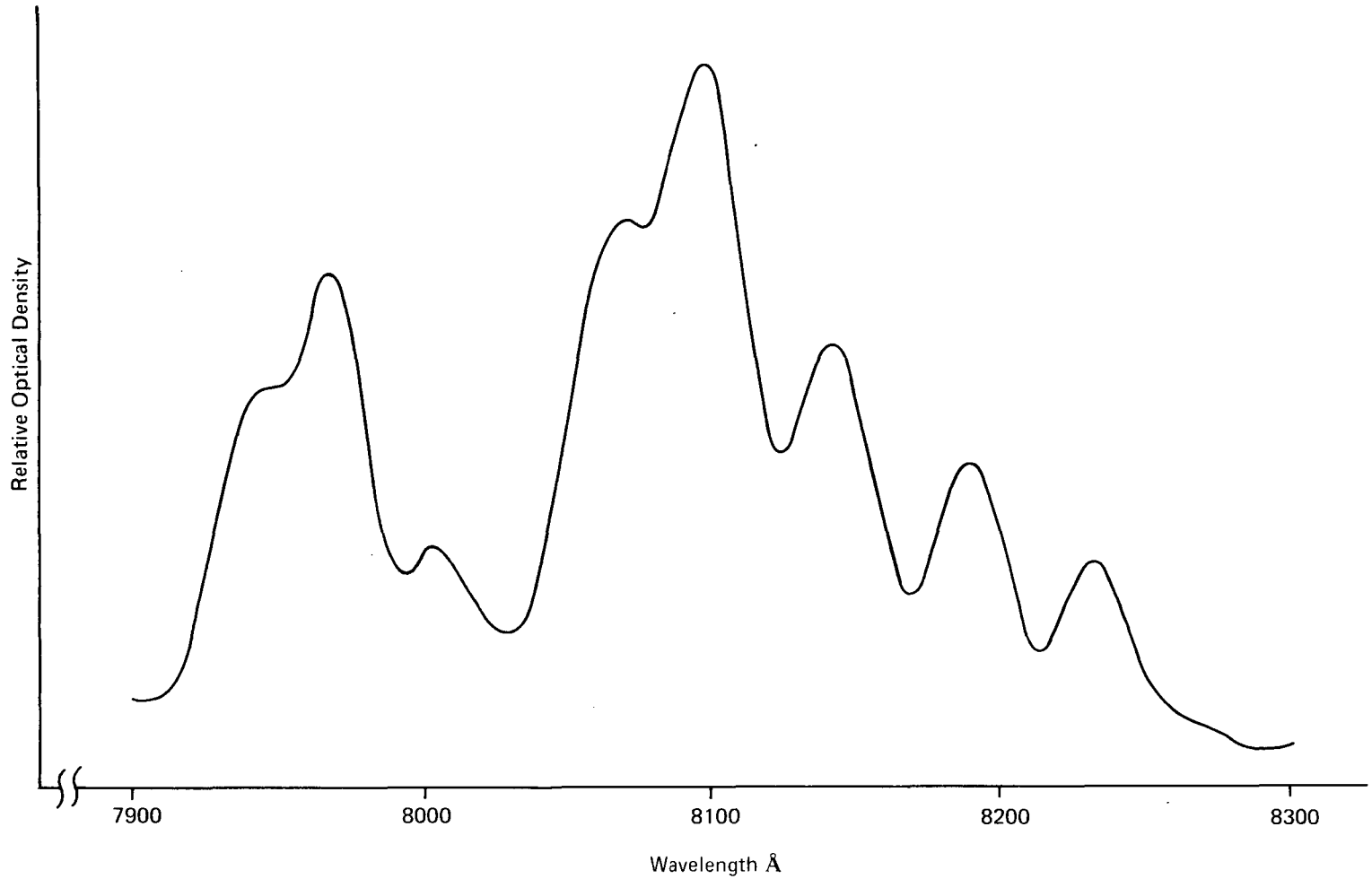

Figure 3-2. Detailed Absorption Spectrum of Nd:YAG in the Transitions from $^4I_{9/2}$ to $^4F_{5/2}$ and $^2H_{9/2}$ States at Room Temperature.

3.2.1 Rate Equations

The pumping cycle of Nd:YAG energy levels[5] is shown in Figure 3-3. The difference of population density N between the upper (N_2) and lower (N_1) levels of the laser transition and the photon density Q of the coherent electromagnetic field obey the following single mode nonlinear rate equations.

$$\frac{dN}{dt} = R_{eff} - \frac{N}{t_s} - WNQ \tag{3.2-1}$$

$$\frac{dQ}{dt} = WNQ - Q(\delta + T_m) \tag{3.2-2}$$

where R_{eff} is the effective pumping rate per unit volume

$$R_{eff} = R - N_1/t_s \tag{3.2-3}$$

R is the pumping rate per unit volume to the upper laser levels, W is the stimulated constant related to the absorption cross section σ of the laser transition by

$$W = c\sigma \tag{3.2-4}$$

c is the speed of light and t_s is the spontaneous emission lifetime of the upper laser levels. δ and T_m are the round trip cavity loss and the fractional output mirror transmission each multiplied by $c/2L$. L is the one way optical length of the resonant cavity. In deriving (3.2-1), we hypothesize that all nonradiative transitions are fast, thus, we may always neglect the population of the pumping band, the population density of the lower laser states are thermalized and proportional to a Boltzmann factor and light intensity is substantially uniform over the beam area. In (3.2-2), the contribution due to spontaneous emission has been neglected.

For operation near room temperature, the laser transitions of Nd:YAG are from line (4) and (5) combined (as shown in Figure 3-3). Hence,

$$N_2 = N_{22} + N_{21} = N_{21}\ (1 + A_2)$$

$$N_1 = N_{12} + N_{13} = N_{12}\ (1 + A_1)$$

$$A_2 = \exp\left(-hc(11510-11426)/kT\right)$$

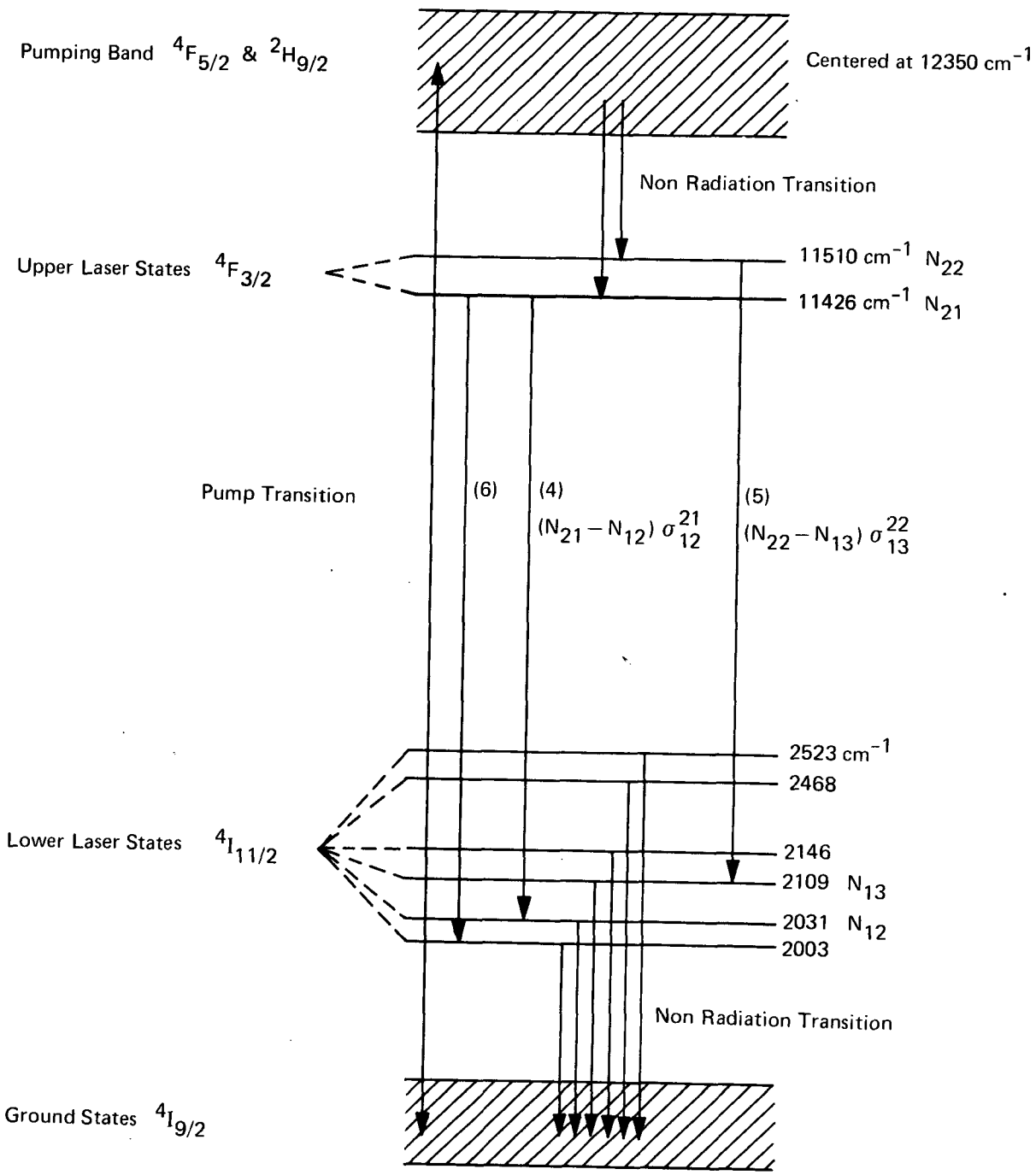

Figure 3-3. Pumping Cycle of Nd:YAG Energy Levels

$$A_1 = \exp [-hc(2109-2031) / kT]$$

$$(N_2-N_1)\,\sigma_{21} = (N_{21}-N_{12})\,\sigma_{12}^{21} + (N_{22}-N_{13})\,\sigma_{13}^{22}$$

$$N_{21} = N_2/(1+A_2),\quad N_{22} = A_2N_2/(1+A_2)$$

$$N_{12} = N_1/(1+A_1),\quad N_{13} = A_1N_1/(1+A_1)$$

$$(N_2-N_1)\;\sigma_{21} = \left(\frac{N_2}{1+A_2} - \frac{N_1}{1+A_1}\right)\sigma_{12}^{21} + \left(\frac{A_2N_2}{1+A_2} - \frac{A_1N_1}{1+A_1}\right)\sigma_{13}^{22}$$

Since $A_2 \cong A_1$

Thus
$$\sigma_{21} = \sigma_{12}^{21}/(1+A_2) + A_2\,\sigma_{13}^{22}/(1+A_2) \qquad (3.2\text{-}5)$$

The values σ_{12}^{21} and σ_{13}^{22} determined by the absorption measurement are 4.6×10^{-20} cm^2 and 8×10^{-19} cm^2, respectively, for the laser transition operating at room temperature [13].

If we denote the CW equilibrium values of N, R_{eff} and Q by $\bar{N}$, $\bar{R}_{eff}$ and $\bar{Q}$; the steady state solutions are obtained from (3.2-1) and (3.2-2) by setting the time derivative equal to zero. Hence,

$$\bar{N} = (\delta + T_m)/W \qquad (3.2\text{-}6)$$

$$\bar{Q} = \left[\bar{R}_{eff}/(\delta + T_m)\right] - 1/Wt_s \qquad (3.2\text{-}7)$$

At the laser threshold, Q=0, from (3.2-1) and (3.2-2) we obtain

$$\bar{R}_{eff}(th) = \frac{\delta + T_m}{Wt_s} \qquad (3.2\text{-}8)$$

Since $\bar{R}_{eff} = \bar{R} - \frac{N_1}{t_s}$

$$\bar{R}(th) = \frac{1}{t_s}\left(\frac{\delta + T_m}{W} + N_1\right) \qquad (3.2\text{-}9)$$

Let

$$\bar{R}(th) = \frac{\eta \bar{P}_{th}}{Vh\,\nu_p} \tag{3.2-10}$$

η is a conversion factor from electrical input power to the pumping rate on the upper laser levels, P_{th} is the electrical input power at the laser threshold, and ν_p is the diode emission central frequency and V is the pumping volume. Thus,

$$\bar{P}_{th} = \frac{Vh\,\nu_p}{\eta\, t_s}\left(\frac{T_m}{W} + \frac{\delta}{W} + N_1\right) \tag{3.2-11}$$

Therefore, $\bar{P}_{th}$ is linearly proportional to the mirror transmission. If $\bar{P}_{th}$ is plotted versus T_m, we will be able to determine the conversion factor and round trip cavity loss.

The steady state power output is

$$\begin{aligned} P &= h\,\nu\, A_m d\, T_m \bar{Q} \\ P &= h\,\nu\, A_m d\, \frac{T_m}{\delta + T_m}\left(\bar{R} - \bar{R}(th)\right) \end{aligned} \tag{3.2-12}$$

Where A_m is the cross section for the laser mode volume, d is the length of the laser active medium, h is Planck's constant and ν is the laser emission frequency. For optimum power output, we set $\frac{dP}{dT_m} = 0$ and obtain an optimum transmission as

$$T_o = \delta\left[\left(\bar{R}_{eff}\, Wt_s/\delta\right)^{1/2} - 1\right] \tag{3.2-13}$$

Substituting T_o for T_m in eq. (3.2-12), we obtain the optimum power output as

$$P_{opt} = h\,\nu\, A_m d\left[(\bar{R}_{eff})^{1/2} - \left(\frac{\delta}{Wt_s}\right)^{1/2}\right]^2 \tag{3.2-14}$$

3.2.2 Amplitude Modulation

Direct modulation of the laser signal output by varying the excitation rate can be done in a diode pumped Nd:YAG laser. The light intensity of the diode is linearly proportional to the amplitude of input current over a large current range [14, 15]. The upper frequency limit for modulation is related to the radiative recombination life of the diode, the resonator decay time, and the pumping rate. To analyze this problem, we use the previous single mode rate equation model. Let n(t) and q(t) be the time dependent perturbations superimposed on CW equilibrium values of $\bar{N}$, $\bar{R}_{eff}$ and $\bar{Q}$; using the small signal approximation, we have the following relationships:

$$\frac{dn(t)}{dt} = r(t) - n(t)\left(\frac{1}{t_s} + W\bar{Q}\right) - Wq(t)\bar{N} \tag{3.2-15}$$

$$\frac{dq(t)}{dt} = W\bar{Q}n(t) \tag{3.2-16}$$

Here we retain only the first order terms. If equations (3.2-15) and (3.2-16) are differentiated with respect to t, we obtain:

$$\frac{d^2n(t)}{dt^2} + \beta\frac{dn(t)}{dt} + \omega_o^2 n(t) = \frac{dr(t)}{dt} \tag{3.2-17}$$

$$\frac{d^2q(t)}{dt^2} + \beta\frac{dq(t)}{dt} + \omega_o^2 q(t) = W\bar{Q}r(t) \tag{3.2-18}$$

$$\omega_o^2 = W\bar{R}_{eff} - \frac{\delta + T_m}{t_s} \tag{3.2-19}$$

$$\beta = \frac{W\bar{R}_{eff}}{\delta + T_m} = \frac{\omega_o^2}{\delta + T_m} + \frac{1}{t_s} \tag{3.2-20}$$

For r(t) = 0 in equations (3.2-17) and (3.2-18), n(t) and q(t) are both proportional to Exp (j ω t), where

$$\omega = \omega_r + j\omega_i$$

$$\omega_r^2 = \omega_o^2 - \left(\frac{\beta}{2}\right)^2 \qquad (3.2\text{-}21)$$

$$\omega_i = \frac{\beta}{2} \qquad (3.2\text{-}22)$$

This shows that when the effective pumping rate is suddenly increased from zero to $\overline{R}_{eff}$, the photon density exhibits a damped relaxation oscillation at the angular frequency ω_r. With a continuous excitation, the presence of this spiking resonance enhances itself in the depth of the light intensity modulation. From equations (3.2-21) and (3.2-22), we will be able to solve for $\overline{R}_{eff}$ and δ in terms of ω_r and ω_i using the relationships of equations (3.2-19) and (3.2-20).

$$\overline{R}_{eff} = \frac{2\omega_i t_s (\omega_r^2 + \omega_i^2)}{W (2\omega_i t_s - 1)} \qquad (3.2\text{-}23)$$

$$\delta = \frac{t_s (\omega_r^2 + \omega_i^2)}{(2\omega_i t_s - 1)} - T_m \qquad (3.2\text{-}24)$$

Thus, equations (3.2-23) and (3.2-24) provide a means to determine the effective pumping rate and the round trip cavity loss. If we have a sinusoidal modulation of pumping rate,

$$r(t) = R_o \exp(j\omega_m t) \qquad (3.2\text{-}25)$$

The solution of equation (3.2-18) will be

$$q(t) = Q_o \exp(j(\omega_m t - \phi)) \qquad (3.2\text{-}26)$$

With

$$Q_o = W\bar{Q}R_o \Big/ \left[(\omega_o^2 - \omega_m^2)^2 + \beta^2 \omega_m^2\right]^{\frac{1}{2}} \qquad (3.2\text{-}27)$$

and

$$\phi = \arctan \left[\beta \omega_m / (\omega_o^2 - \omega_m^2) \right] \tag{3.2-28}$$

The maximum output modulation depth occurs at

$$\omega_m^2 = \omega_o^2 - \frac{\beta^2}{2} \tag{3.2-29}$$

4.1 PUMPING EFFICIENCY OF CYLINDRICAL REFLECTOR IN A LIGHT EMITTING DIODE-PUMPED SOLID STATE LASER

An optically pumped solid state laser should have efficient optical coupling from the radiation source to the laser rod. Among several schemes such as: the elliptical cylindrical [16, 17] reflector; spherical reflector [18]; and exfocal ellipsoidal [19] reflector; the elliptical cylindrical reflector is still the most popular one. Nevertheless, fabrication of an elliptical cavity is difficult; it is hard to make a perfect elliptical shape and polish it to a high optical quality. For this practical reason, we consider a circular cylindrical reflector instead of an elliptical cylindrical reflector. The analysis that follows will apply specifically to the light emitting diode (LED) pumped solid state laser. Since light emission of an LED comes from the N-type flat surface, a half-cylinder reflector will be adequate for an LED-pumped laser reflector.

The purpose of this analysis is to calculate the pumping efficiency for an LED-pumped Nd:YAG laser as a function of emission width of the LED, optical resonator configuration and laser rod size. The calculation is made for TEM_{oo} mode operation. Therefore, the loss due to Fresnel reflection at the crystal surface, the power absorbed in the laser rod before entering the mode volume, and the second reflection of a gold plated groove underneath the rod, will all be considered. Since the circular cylindrical reflector is terminated at each end by highly reflecting mirrors perpendicular to the axis of the cylinder, it may be assumed that the cylinder is infinitely long. With this assumption, the analysis is reduced to a two-dimensional case.

A circular reflector is a distorted lens system; the image location and image size vary as a function of position on the reflector surface; thus, it is difficult to derive a general expression for the real situation. Consequently, a ray tracing technique was used to calculate the amount of power absorbed in the fundamental mode volume after reflection and attenuation through the laser rod.

The method for ray tracing to be presented here is shown in Figure 4-1. P_o is the total optical power emitted by the light source, and 2W is the emission width of the LED. The light source will be placed on the x-axis with its center at d_1 and divided in increments, du. The one dimensional coordinate u on the

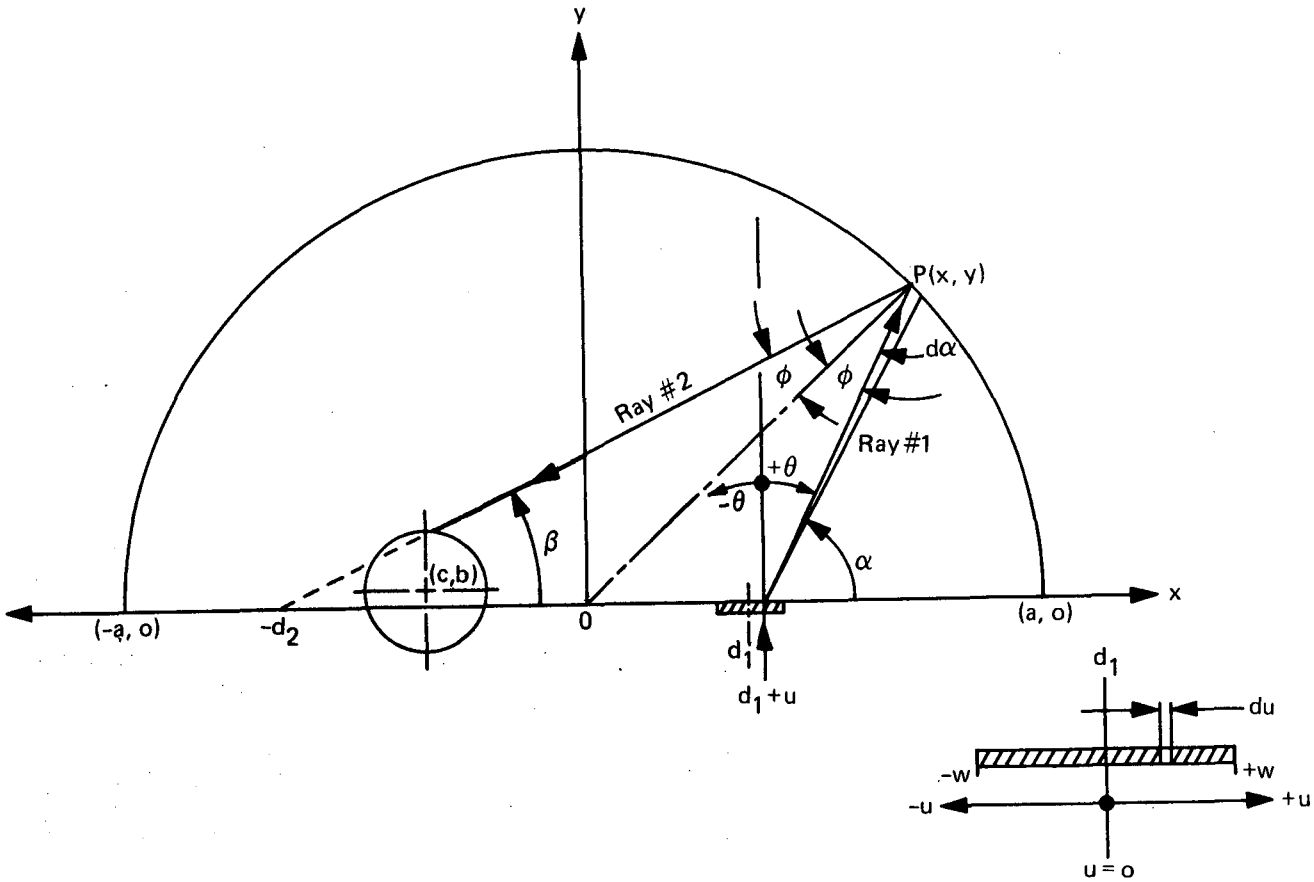

Figure 4-1. Ray Tracing of a Circular Reflector in Diode Pumped Nd:YAG Laser

light source is chosen with u=o at d_1; therefore, the position u on the light source corresponds to d_1+u on the x coordinate. Thus, the flux dF radiated into an angle $d\alpha$ from an increment du located at u is

$$dF = \frac{P_o \cos\theta \, d\alpha \, du}{2 W \pi} \qquad (4.1\text{-}1)$$

where $\cos\theta$ is the emission pattern of the flat LED [20,21]. The angle θ is related to α by

$$\theta = \frac{\pi}{2} - \alpha . \qquad (4.1\text{-}2)$$

Thus $\cos\theta = \sin\alpha$.

If the laser rod were not in place, the flux dF would reflect at the position $-d_2$ as shown in Figure 4-1. From the geometry, it can be seen that

$$(d_1 + u)/\sin \phi = a/\sin (\pi-\alpha) \tag{4.1-3}$$

$$d_2/\sin \phi = a/\sin \beta \tag{4.1-4}$$

where $\beta = \alpha - 2\phi$ (4.1-5)

and $\phi = \arcsin [(d_1+u) \sin \alpha/a]$. (4.1-6)

Dividing (4.1-4) by (4.1-3), we obtain

$$d_2/(d_1 + u) = \sin \alpha/ \sin \beta .$$

Hence, $d_2 = (d_1+u) \sin \alpha/\sin \beta$ (4.1-7)

the slope of the reflected ray 2 is $m = \tan \beta$.

The line of the reflected ray 2 can be expressed by

$$y = m (x+d_2) \tag{4.1-8}$$

Now we consider a laser rod located at (-c, b). The perimeter of the laser rod can be expressed by the equation

$$(x+c)^2 + (y-b)^2 = R^2 \tag{4.1-9}$$

where R is the radius of the laser rod. If this reflected ray passes through the laser rod, then equations (4.1-8) and (4.1-9) should have common real solutions. Substituting $x = (y-md_2)/m$ in equation (4.1-9), we get

$$Ay^2+By + C = 0 \tag{4.1-10}$$

where

$$A = 1+m^2$$

$$B = -2m (d_2-c+mb)$$

$$C = m^2 [(d_2-c)^2+b^2-R^2].$$

Therefore, the condition of the reflected ray intercepting the laser rod is

$$B^2 - 4AC > 0 \tag{4.1-11}$$

and

$$y = (-B \pm (B^2 - 4AC)^{1/2})/2A$$

Since the reflected ray is propagating downward, the intercept with the greater y value is the intercept where the ray first encounters the rod surface.

Let

$$y_o = \left\{-B + (B^2 - 4AC)^{1/2}\right\}/2A \tag{4.1-12}$$

then

$$x_o = (y_o - md_2)/m. \tag{4.1-13}$$

Hence (x_o, y_o) is the point which the reflected ray first encounters in the laser rod. The normal to the rod surface at the point (x_o, y_o) of interception is

$$y = m_1 x + h \tag{4.1-14}$$

$$m_1 = (y_o - b)/(x_o + c) \tag{4.1-15}$$

$$h = b + m_1 c.$$

The angle of the normal with respect to the x-axis is

$$\gamma = \arctan (y_o - b)/(x_o + c).$$

Therefore the incident angle θ_1 to the laser rod is

$$\theta_1 = |\gamma - \beta| \tag{4.1-16}$$

the refraction angle θ_2 inside of the laser rod is

$$\sin \theta_2 = n_1 \sin \theta_1 / n_2 \tag{4.1-17}$$

where n_1 is the index of refraction outside of the laser rod and n_2 is the refractive index of the laser rod.

The line of the refracted ray can be represented by

$$y = m_1 x + h_1 \tag{4.1-18}$$

where $$m_1 = \tan (\beta \pm \theta_2). \tag{4.1-19}$$

In equation (4.1-19) the plus sign is for the case $\beta \leq \pi/2$ and the minus sign for the case $\beta > \pi/2$.

$$h_1 = y_o - m_1 x_o \tag{4.1-20}$$

Assume the radius of the fundamental transverse mode volume is R_m, then

$$(x + c)^2 + (y - b)^2 = R_m^2 \tag{4.1-21}$$

If the refracted ray passes through the mode volume, then equations (4.1-18) and (4.1-21) should have common solutions. Substituting in equation (4.1-21), we obtain

$$A_1 y^2 + B_1 y + C_1 = 0 \tag{4.1-22}$$

where

$$A_1 = 1 + m_1^2 \qquad B_1 = -2 (h_1 - m_1 c + m_1^2 b)$$

$$C_1 = (h_1 - m_1 c)^2 + m_1^2 (b^2 - R_m^2).$$

Then

$$y_1 = [-B_1 + (B_1^2 - 4A_1C_1)^{1/2}]/2A_1 \quad (4.1\text{-}23)$$

$$y_2 = [-B_1 - (B_1^2 - 4A_1C_1)^{1/2}]/2A_1 \quad (4.1\text{-}24)$$

and

$$x_1 = (y_1 - h_1)/m_1 \quad (4.1\text{-}25)$$

$$x_2 = (y_2 - h_1)/m_1 \quad (4.1\text{-}26)$$

(x_1, y_1) is the first point where the refracted ray enters into the mode volume and (x_2, y_2) is the point where the refracted ray leaves the mode volume as shown in Figure 4-2. (x_3, y_3) is the point where the refracted ray leaves the laser rod surface.

$$y_3 = [-B_2 - (B_2^2 - 4A_2C_2)^{1/2}]/2A_2 \quad (4.1\text{-}27)$$

$$x_3 = (y_3 - h_1)/m_1 \quad (4.1\text{-}28)$$

where

$$A_2 = A_1$$

$$B_2 = B_1$$

$$C_2 = (h_1 - m_1c)^2 + m_1^2 (b^2 - R^2)$$

After leaving the rod, the ray will reenter the rod through the reflection of the gold plated groove underneath the rod as shown in Figure 4-2. Now we can proceed to calculate the power absorbed inside of the mode volume.

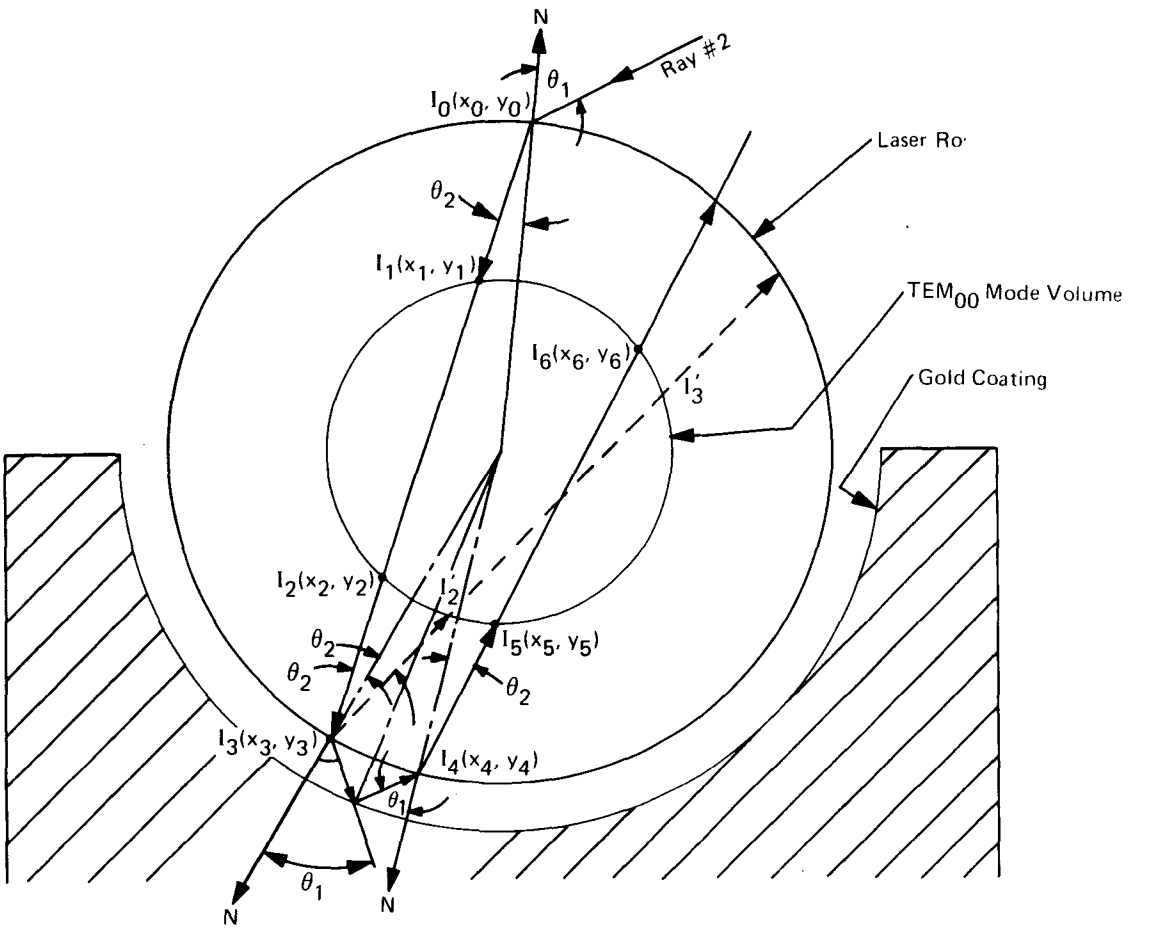

Figure 4-2. Beam Paths Inside of the Nd:YAG Rod

The average Fresnel reflection on the rod surface for perpendicular and parallel polarizations [22] is

$$R_f = \frac{1}{2}\left[\frac{\sin^2(\theta_1-\theta_2)}{\sin^2(\theta_1+\theta_2)} + \frac{\tan^2(\theta_1-\theta_2)}{\tan^2(\theta_1+\theta_2)}\right] \qquad (4.1\text{-}29)$$

Thus the transmission into the rod is $T = 1-R_f$.

The distance that the ray travels through the laser rod is

$$D_r = \left[(x_o - x_3)^2 + (y_o - y_3)^2\right]^{\frac{1}{2}} \tag{4.1-30}$$

Similarly, the distance that the ray passes through the mode volume is

$$D_m = \left[(x_1 - x_2)^2 + (y_1 - y_2)^2\right]^{\frac{1}{2}} \tag{4.1-31}$$

Let $I_o(x_o, y_o)$ be the optical flux incident to the rod at (x_o, y_o) then

$$I_1(x_1, y_1) = TI_o(x_o, y_o) \exp\left[-\alpha_o (D_r - D_m)/2\right] \tag{4.1-32}$$

where α_o is the absorption coefficient of the Nd:YAG crystal. And

$$I_2(x_2, y_2) = TI_o(x_o, y_o) \exp\left[-\alpha_o (D_r + D_m)/2\right] \tag{4.1-33}$$

$$I_3(x_3, y_3) = TI_o(x_o, y_o) \exp\left(-\alpha_o D_r\right) \tag{4.1-34}$$

$$I_4(x_4, y_4) = T^3 R_g I_o(x_o, y_o) \exp\left(-\alpha_o D_r\right) \tag{4.1-35}$$

R_g is the reflectivity of the gold coating. It can be seen in Figure 4-2, that internally reflected rays I_2' and I_3' inside the rod and the re-entering rays I_4, I_5 and I_6 will pass the same distance as I_1, I_2 and I_3.

Hence,

$$I_5 = T^3 R_g I_o(x_o, y_o) \exp\left[-\alpha_o (3D_r - D_m)/2\right] \tag{4.1-36}$$

$$I_6 = T^3 R_g I_o(x_o, y_o) \exp\left[-\alpha_o (3D_r + D_m)/2\right] \tag{4.1-37}$$

$$I_2' = R_f TI_o(x_o, y_o) \exp\left[-\alpha_o (3D_r - D_m)/2\right] \tag{4.1-38}$$

$$I_3' = R_f TI_o(x_o, y_o) \exp\left[-\alpha_o (3D_r + D_m)/2\right] \tag{4.1-39}$$

Therefore the power absorbed inside the mode volume is

$$P_m = (I_1 - I_2) + (I_5 - I_6) + (I_2' - I_3') \tag{4.1-40}$$

Substitution of (4.1-32) through (4.1-39) in (4.1-40), gives an expression for the fraction of power absorbed in the mode volume

$$P_{ab}(\%) = 2T \sin h\,(\alpha_o D_m/2) \exp(-\alpha_o D_r/2)\,[1+(T^2 R_g + R_f) \exp(-\alpha_o D_r)] \tag{4.1-41}$$

The total pumping efficiency into the mode volume is calculated by combining equations (4.1-1) and (4.1-41), and integrating over the ranges indicated.

$$E_{cp} = \frac{R_g}{W} \int_{-W}^{W} \int_{0}^{\pi} (\sin\alpha) \exp(-\alpha_o D_r/2) \sin h\,(\alpha_o D_m/2)\, x \; T\left[1 + (T^2 R_g + R_f) \exp(-\alpha_o D_r)\right] d\alpha\, du \tag{4.1-42}$$

where D_r and D_m are all complicated functions of α and u. The pumping efficiency E_{cp} can be evaluated numerically. The results are plotted in Figure 4-3 with the following parameters:

Radius of the circular reflector a = 2.5 cm.

Laser rod diameter 1.5mm.

The width of GaAlAs LED 2W = 0.03048 cm.

Nd:YAG doping level 1.3 atomic percent [23].

Peak absorption cross section of Nd:YAG at 8100Å.

$\sigma = 1.2 \times 10^{-19}$ cm^2 [13]

The average absorption coefficient of Nd:YAG for the transition from $^4I_{9/2}$ to $^4F_{5/2}$ and $^2H_{9/2}$ is $\bar{\alpha}_o = 3.55$ cm^{-1}.

The reflectivity of gold near 8100Å, $R_g = 97.4\%$. Refractive index of Nd:YAG $n_2 = 1.82$.

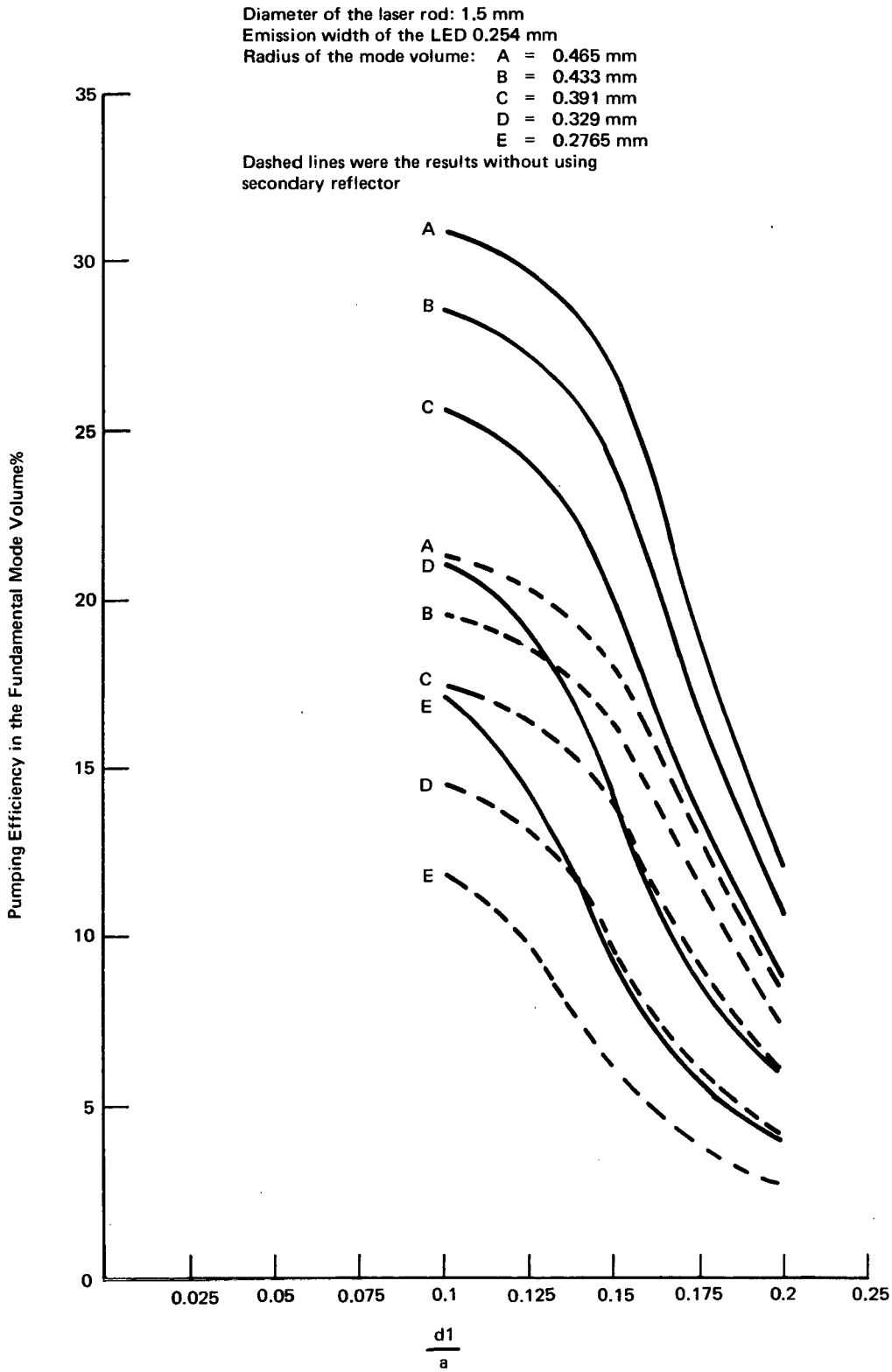

Figure 4-3. Pumping Efficiency of a Circular Cylindrical Reflector

The data plotted in Figure 4-3 was divided into two groups: Group I was the actual pumping efficiency in the fundamental mode volume; and Group II was evaluated without considering secondary reflection from the gold plated groove underneath the rod. Note that a good reflection gold plated groove is necessary since one-third of the power absorbed in the mode volume is due to the secondary reflection.

By a similar ray tracing approach, the case of a single elliptical cylinder has been analyzed. The pumping efficiency for single elliptical cavity was plotted in Figure 4-4. Comparing the results of Figure 4-3 and 4-4, it may be concluded that if the separation of laser rod and LED array is equal to or less than 15 percent of the reflector diameter, the pumping efficiency of a circular reflector is comparable to the corresponding elliptical reflector; however, as the separation of LED array and laser rod increase, the pumping efficiency of the circular reflector drops more steeply than for the elliptical reflector, since a large portion of the reflected rays from the circular reflector are then outside of the mode volume.

4.2 INDEX MATCHING

Mismatch of the refractive indices at the interface of semiconductor material and air limits light output efficiency of the diode. For the case of GaAlAs LEDs, light generated in the p-n junction is emitted through the flat n-type surface; the large index of refraction mismatch between the diode ($n = 3.5$) and air ($n = 1$) prevents light emission at angles greater than the critical angle ($\theta_c = \sin^{-1}$ (1/3.5) or 16°) by total internal reflection. This difficulty limits maximum light output efficiency of a bare diode to approximately 2 percent even though the internal quantum efficiency is nearly 100 percent.

The loss due to total internal reflection can be reduced by diode configuration. A spherical domed structure that surrounds the planar junction region at about 3.5 times the junction diameter increases the diode emission significantly, since the incidence of most of the light with the spherical surface will be at angles less than critical. This technique is very useful for individual diodes but is less favorable in diode arrays because of the limited packing density and scattering from adjacent domes. Another technique by which this loss can be reduced is through avoidance of semiconductor/air interfaces. This can be realized by placing a solid, transparent reflectively coated cylinder in direct contact with the diode array. Since direct contact is difficult when diode lead wires cause interference, the more practical design places the cylinder very near the array (~ 50 μm) and fills the gap with viscous transparent fluid with

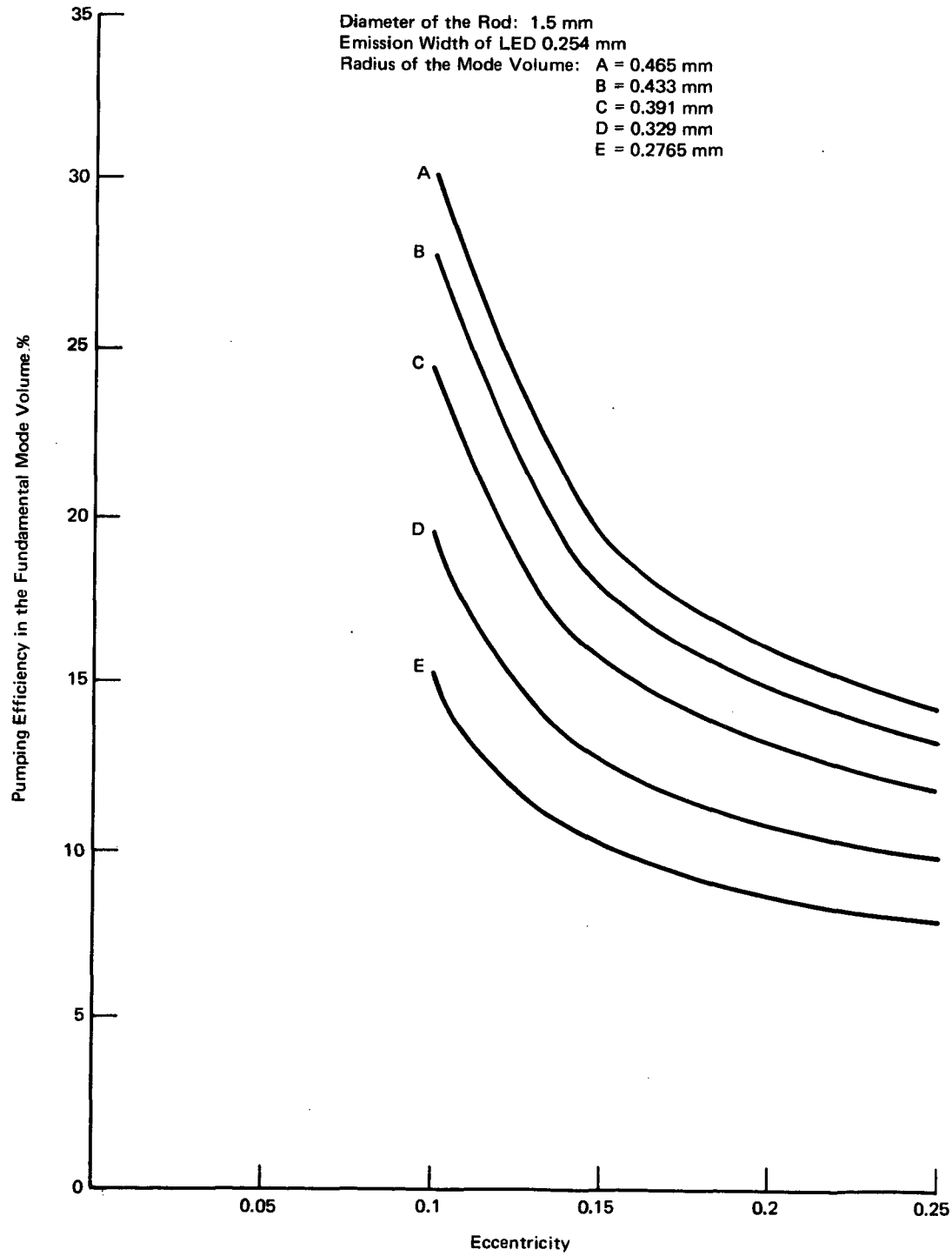

Figure 4-4. Pumping Efficiency of an Elliptical Reflector

an appropriate refractive index. This increases the critical angle and also reduces the Fresnel reflection both of which increase the diode efficiency. This method lends itself to the construction of large arrays with high packing density. For a specified volume excitation density and LED efficiency, the diode drive current density is inversely proportional to the packing density. Since diode life is adversely affected by high current density, high packing density and concomitant low current density are very desirable.

The sketch of an index matching technique is shown in Figure 4-5. According to Snell's law

$$n_1 \sin\theta = n_2 \sin\theta_2 = n_3 \sin\theta_3 \qquad (4.2\text{-}1)$$

where n_1 is the index of refraction in the LED, n_2 in the interface and n_3 in the index matching cylinder. θ_1, θ_2 and θ_3 are the incident angle in the medium 1, 2, and 3, respectively. The maximum emission angle of the diode is

$$\begin{aligned} \theta_{max} &= \arcsin(n_3/n_1) \quad \text{for the case } n_1 > n_2 > n_3 \\ \theta_{max} &= \arcsin(n_2/n_1) \quad \text{for the case } n_1 > n_3 > n_2 \end{aligned} \qquad (4.2\text{-}2)$$

The relative emission efficiency of a diode can be expressed by

$$E_c = \frac{B}{2\pi} \int_0^{\pi} \int_0^{\theta_{max}} (1-R_{12}^2)(1-R_{23}^2) \sin\theta_1 \cos\theta_1 \, d\theta_1, d\phi \qquad (4.2\text{-}3)$$

In deriving Equation (4.2-3) it is assumed that the n-type surface of the GaAlAs diode is completely transparent; reflected light is absorbed in the material. In reality, these conditions may not be exactly true. R_{12} is the reflection coefficient between medium 1 and 2 and R_{23} between medium 2 and 3. Cos θ is the emission pattern of LED. B is the transmission constant related to the interface and laser rod. E_c is integrated in the solid cone within θ_{max}. Two polarizations have to be considered [24], namely perpendicular polarization where the electric vector E is perpendicular to the plane of incidence and, parallel polarization where E is parallel to the plane of incidence.

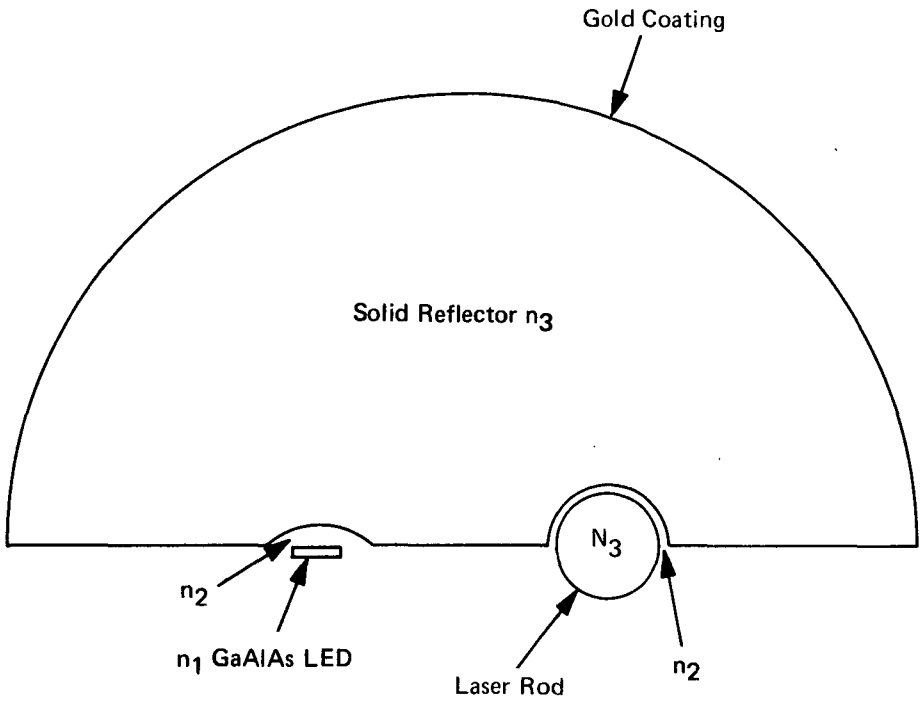

(a) Optical Index Matching

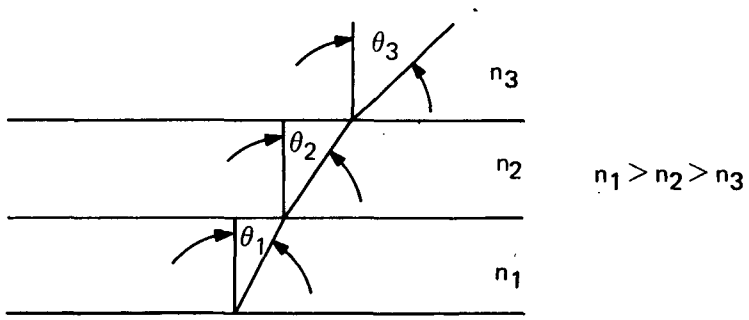

(b) Beam Refraction Through Multilayer Medium

Figure 4-5. Index Matching Technique

Case I: Perpendicular Polarization

$$R_{12}(I) = \frac{\cos\theta_1 - [(n_2/n_1)^2 - \sin^2\theta_1]^{1/2}}{\cos\theta_1 + [(n_2/n_1)^2 - \sin^2\theta_1]^{1/2}} \qquad (4.2\text{-}4)$$

$$R_{23}(I) = \frac{\left\{1-(n_1\sin\theta_1/n_2)^2\right\}^{1/2} - \left\{(n_3/n_2)^2 - (n_1\sin\theta_1/n_2)^2\right\}^{1/2}}{\left\{1-(n_1\sin\theta_1/n_2)^2\right\}^{1/2} + \left\{(n_3/n_2)^2 - (n_1\sin\theta_1/n_2)^2\right\}^{1/2}} \qquad (4.2\text{-}5)$$

Case II: Parallel Polarization

$$R_{12}(II) = \frac{(n_2/n_1)^2\cos\theta_1 - \left\{(n_2/n_1)^2 - \sin^2\theta_1\right\}^{1/2}}{(n_2/n_1)^2\cos\theta_1 + \left\{(n_2/n_1)^2 - \sin^2\theta_1\right\}^{1/2}} \qquad (4.2\text{-}6)$$

$$R_{23}(II) = \frac{(n_3/n_2)^2\left\{1-(n_1\sin\theta_1/n_2)^2\right\}^{1/2} - \left\{(n_3/n_2)^2 - (n_1\sin\theta_1/n_2)^2\right\}^{1/2}}{(n_3/n_2)^2\left\{1-(n_1\sin\theta_1/n_2)^2\right\}^{1/2} + \left\{(n_3/n_2)^2 - (n_1\sin\theta_1/n_2)^2\right\}^{1/2}} \qquad (4.2\text{-}7)$$

From equations (4.2-4) through (4.2-7), all functions of angle are expressed in terms of θ_1 through the relationship (4.2-1). Equation (4.2-3) was evaluated for three cases, diode to air ($n_1 = 3.5$, $n_2 = n_3 = 1$), diode to Lens Bond to Yttrium Aluminum Garnet (YAG) cylinder ($n_1 = 3.5$, $n_2 = 1.55$, $n_3 = 1.82$), and diode to low melting point high index glass to YAG cylinder ($n_1 = 3.5$, $n_2 = 2.2$, $n_3 = 1.82$). The computed results of relative diode emission efficiency are listed in Table 4-1.

Table 4-1. Improvement of Diode Emission Efficiency by Index Matching

I. Perpendicular Polarization				
n_1	n_2	n_3	E_c	Improvement related to bare diode
3.5	1	1	1.33%	Same
3.5	1.55	1.82	4.495%	338.9%
3.5	2.2	1.82	7.685%	579.5%

Table 4-1. Improvement of Diode Emission Efficiency by Index Matching (cont.)

II. Parallel Polarization				
n_1	n_2	n_3	E_c	Improvement related to bare diode
3.5	1	1	1.84%	Same
3.5	1.55	1.82	5.635%	306.5%
3.5	2.2	1.82	8.35%	454.3%

From above results, the average theoretical improvement for laser pumping rate through index matching are 517% for $n_2 = 2.2$ and 324% for $n_2 = 1.55$. The transmissions from diode to laser rod through various index matching media as a function of angle were plotted in Figure 4-6 and Figure 4-7.

These figures show how various index materials affect the transmission of optical energy and the critical emission angle in the semiconductor material.

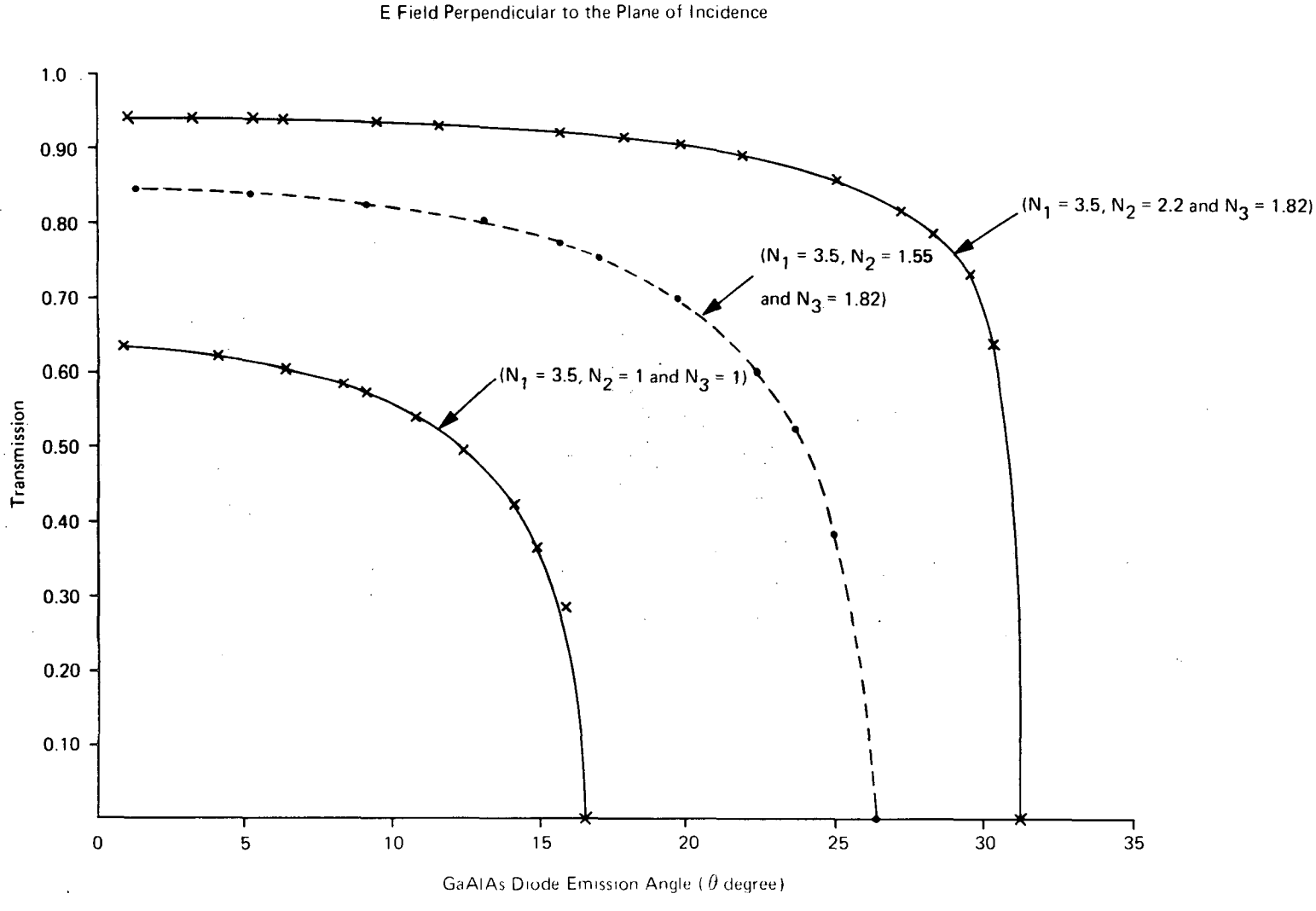

Figure 4-6. Light Transmission Through Layered Media for E Field Perpendicular to the Plane of Incidence

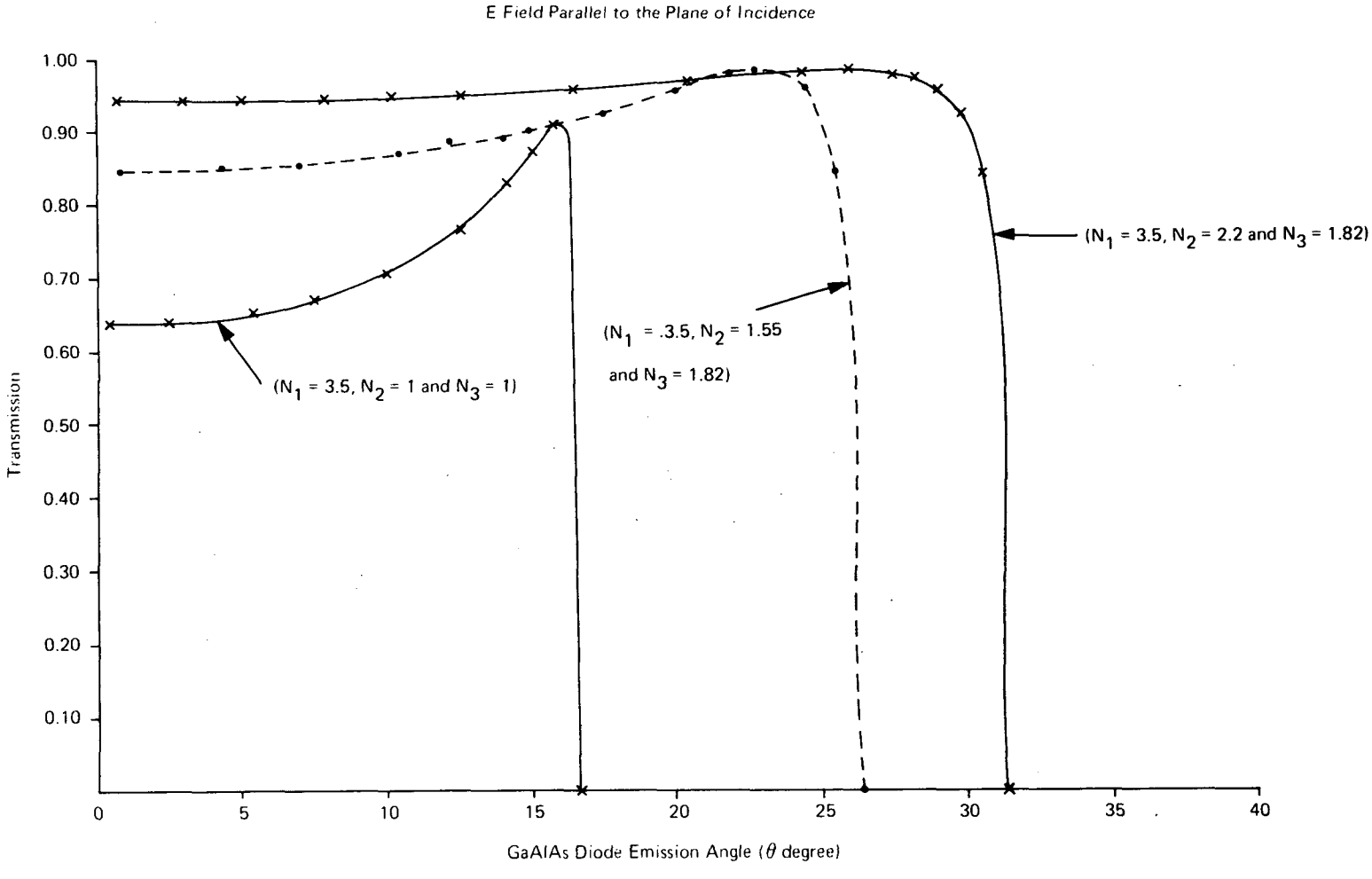

Figure 4-7. Light Transmission Through Layered Media for the E Field Parallel to the Plane of Incidence

5.1 APPARATUS

Lasers with two kinds of pumping cavities were used in these experiments; a semicircular metal reflector, and a solid half-cylinder. Both were 5.0 cm in diameter and 5.6 cm long. The metal reflector was stainless steel with the inside surface optically polished and gold plated. The solid half-cylinder was Schott LaSF12 glass. The curved and flat end surfaces were optically polished and gold coated. Two grooves parallel to the cylinder axis were at opposite sides of the center line on the glass half-cylinder. The groove for the laser rod was 1.5 mm in diameter and 2.5 mm off center. The other groove was 1.4 mm wide and 0.5 mm deep, located 2.5 mm off center, at the position of the diode array. Both grooves were optically polished to reduce scattering losses. The interfaces between the diode array, glass cylinder, and laser rod were filled with Lens Bond* for index matching. The physical appearance of the metal reflector, glass half-cylinder, and an assembled diode array can be seen in Figure 5-1.

The upper surface of the diode array and the axis of the laser rod were located on the diameter of the reflector. The diode array heat sink was fastened on a horizontal sled. Horizontal adjustment was provided by two screws threaded into the sled. Dowel pins at each end of the heat sink slid into the arms of a vertical yoke of the fixture. The yoke provided relative vertical motion between the horizontal sled and the heat sink for vertical adjustment of the diode array. The bottom plate of the fixture was supported on three thermoelectric coolers. All contact surfaces between metal parts were gold plated and had a thin layer of Wakefield thermal joint compound No. 120 for good thermal conduction. The bottom plates of the thermoelectric coolers were soldered to a water-cooled box for heat removal.

The laser rod was placed in an optically polished and gold plated groove in its own heat sink. This heat sink fastened to another fixture in exactly the same arrangement as the diode array side, but was thermally isolated from it. The laser rod and diode array temperature were controlled independently by varying the current through their respective thermoelectric coolers. Temperatures

*Lens Bond F-65 made by Summers Laboratories, Inc., Fort Washington, Pennsylvania 19034.

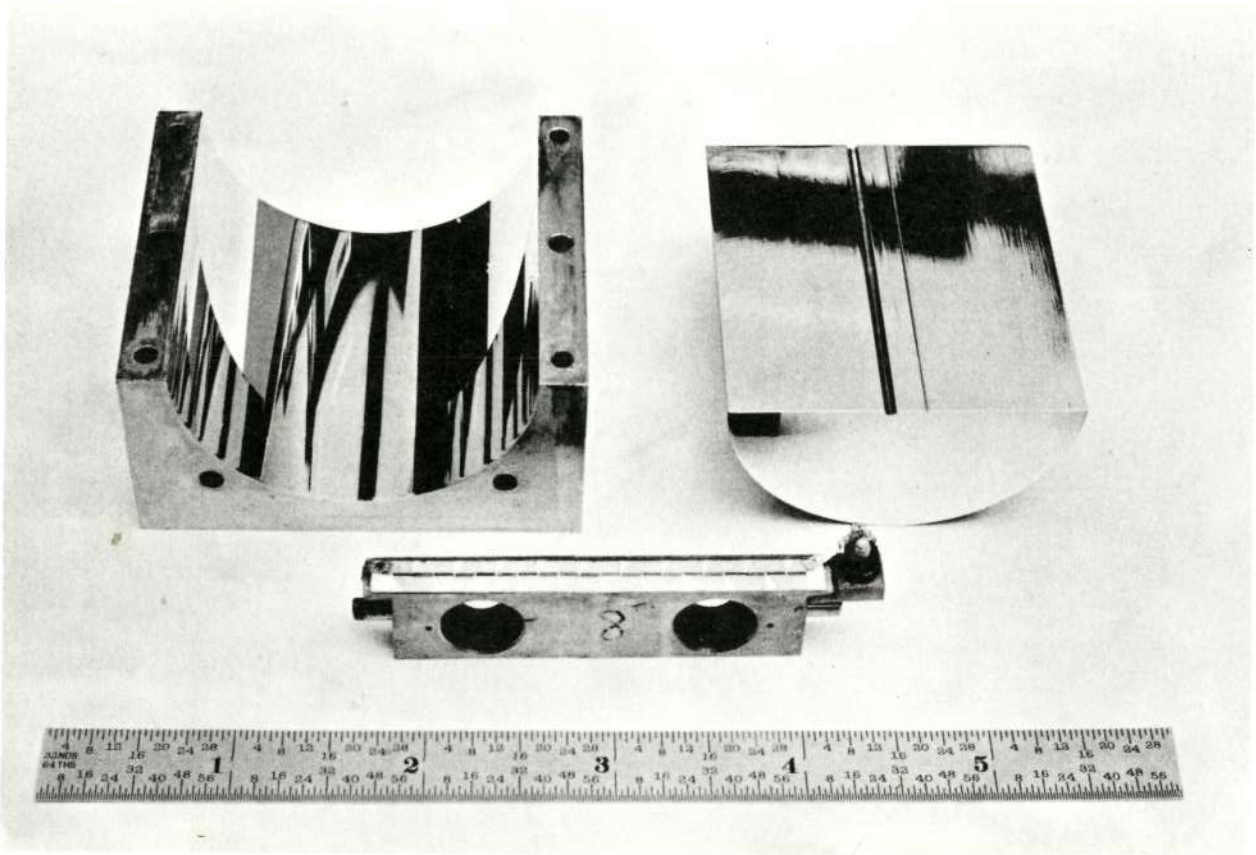

Figure 5-1. Photograph of Metal Reflector, Index Matching Cylinder, and the Assembled Diode Array

were monitored with copper-constantan thermocouples directly attached to the heat sinks. The schematic drawing of this laser device with a metal reflector is shown in Figure 5-2. Figure 5-3 shows the photograph of the complete laser device with end plates removed. Figure 5-4 is the photograph of a laser device with index matching solid cylinder.

Alignment of the laser rod and diode array was very critical for efficient laser operation. Initial alignment was done using a 3-axis traveling microscope to align the relative positions of the rod, diode array, and reflector according to predetermined dimensions. The sharp edges of the reflector, diode, and the perimeter of the laser rod were chosen as the references for the microscope measurements. The measurements of the front and back ends were repeated several times to ensure their accuracy. When laser oscillation begins, further improvement of the coupling efficiency can be achieved by slight vertical and horizontal adjustments of the diode array. The best experimental results were obtained with this alignment procedure.

All experiments were performed with 1.5 mm diameter and 56 mm long laser rods with dielectric coatings on the end surfaces. Output transmission was 0.1, 0.2 and 0.4 percent on flat (0.1 percent) and one meter radius of curvature surfaces; the other ends had a one meter radius of curvature and were coated for maximum reflection. In all cases, the beam diameters of TEMooq mode were approximately uniform along the rod. The diode array was driven in continuous (CW) and pulsed modes. For pulsed operation, a Rutherford pulse generator Model B7D, cathode follower amplifier and a Tektronix Model 565 oscilloscope with Dual Beam Plug in Type 1A1 were used. The pulse current was measured by the voltage drop across a one ohm resistor in series with the GaAlAs diode array. The schematic for pulsed operation is shown in Figure 5-5. In all pulsed experiments, a pulse repetition frequency of 20 Hz was used. CW laser power output was detected with an EG&G radiometer Model 580 and narrow beam adapter. Measured values were calibrated by using an Epply Thermopile and a Keithley nanovoltmeter. The whole laser device was enclosed in a clear acrylic plastic box with a continuous dry nitrogen gas purge for operation below room temperature. Gas flow pressure was maintained constant at 2 lb./in.^{2} by a fine pressure regulator.

5.2 LASER PERFORMANCE WITH CONVENTIONAL METAL REFLECTOR

a. Pumping Threshold — The threshold for lasing in Nd:YAG is very sensitive to temperature variations due mainly to the increase in lower laser level population density, N_1, as described by Boltzmann's law.

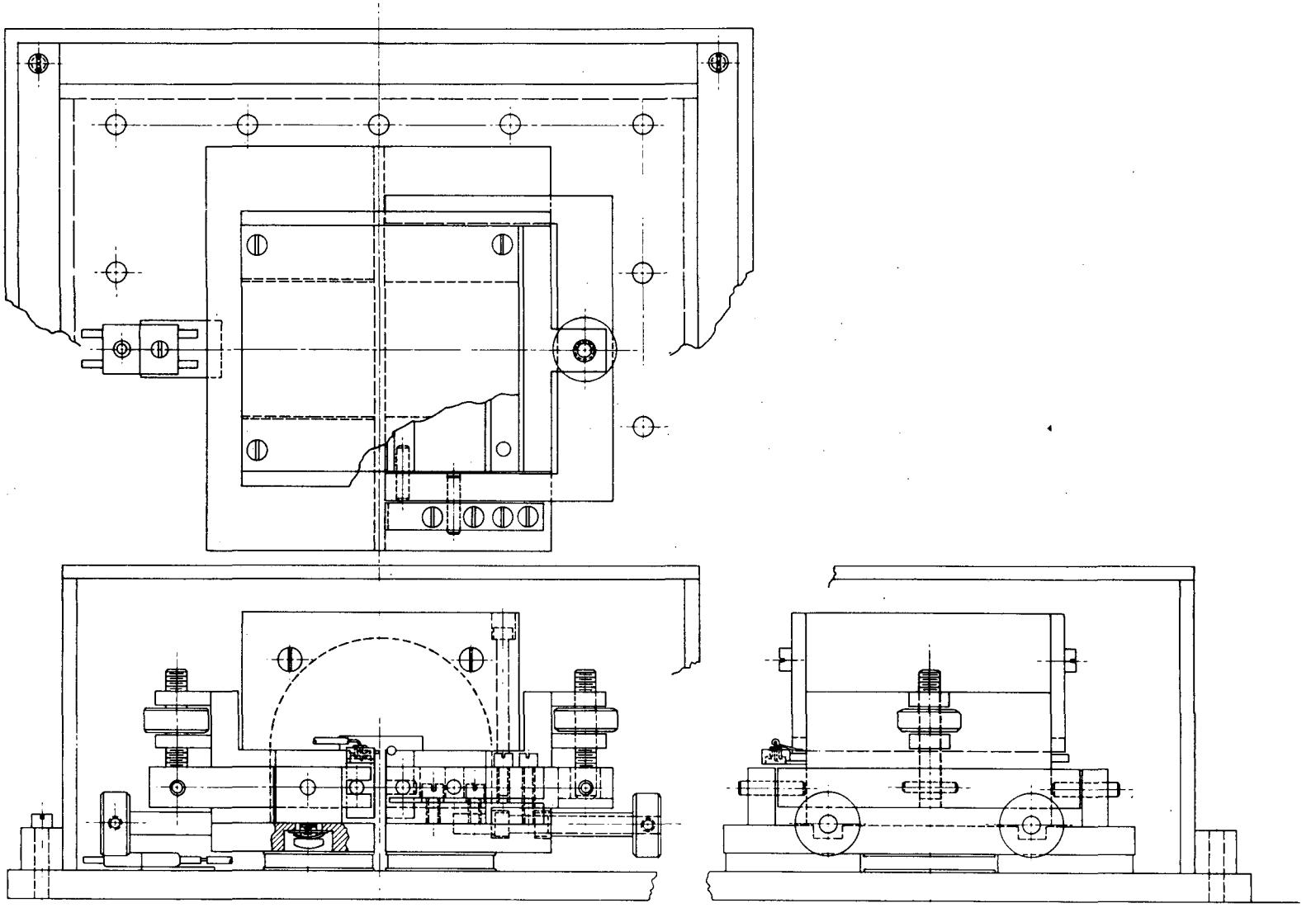

Figure 5-2. Schematic Layout of Diode Pumped Nd:YAG Laser Device

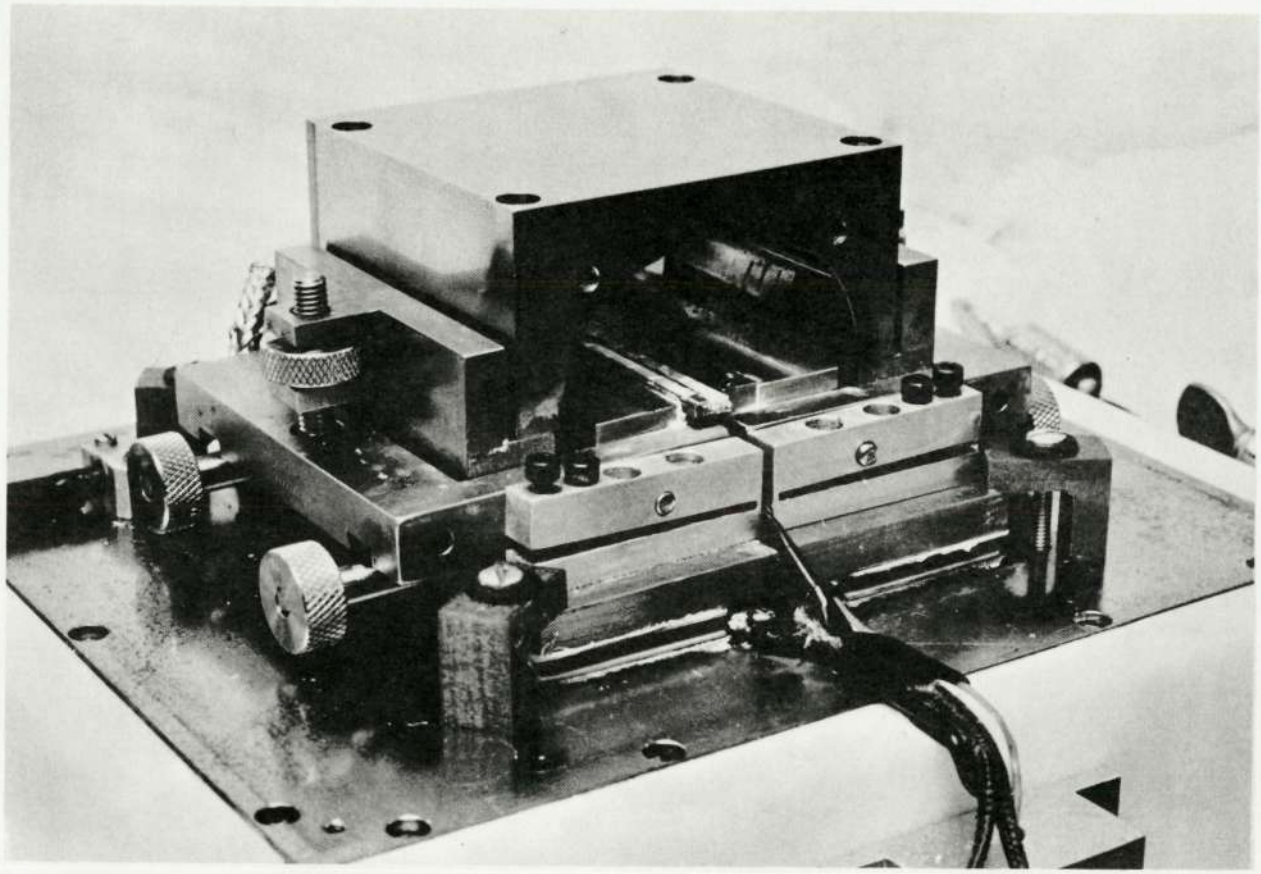

Figure 5-3. Photograph of Diode Pumped Nd:YAG Laser Device with End Reflector Removed

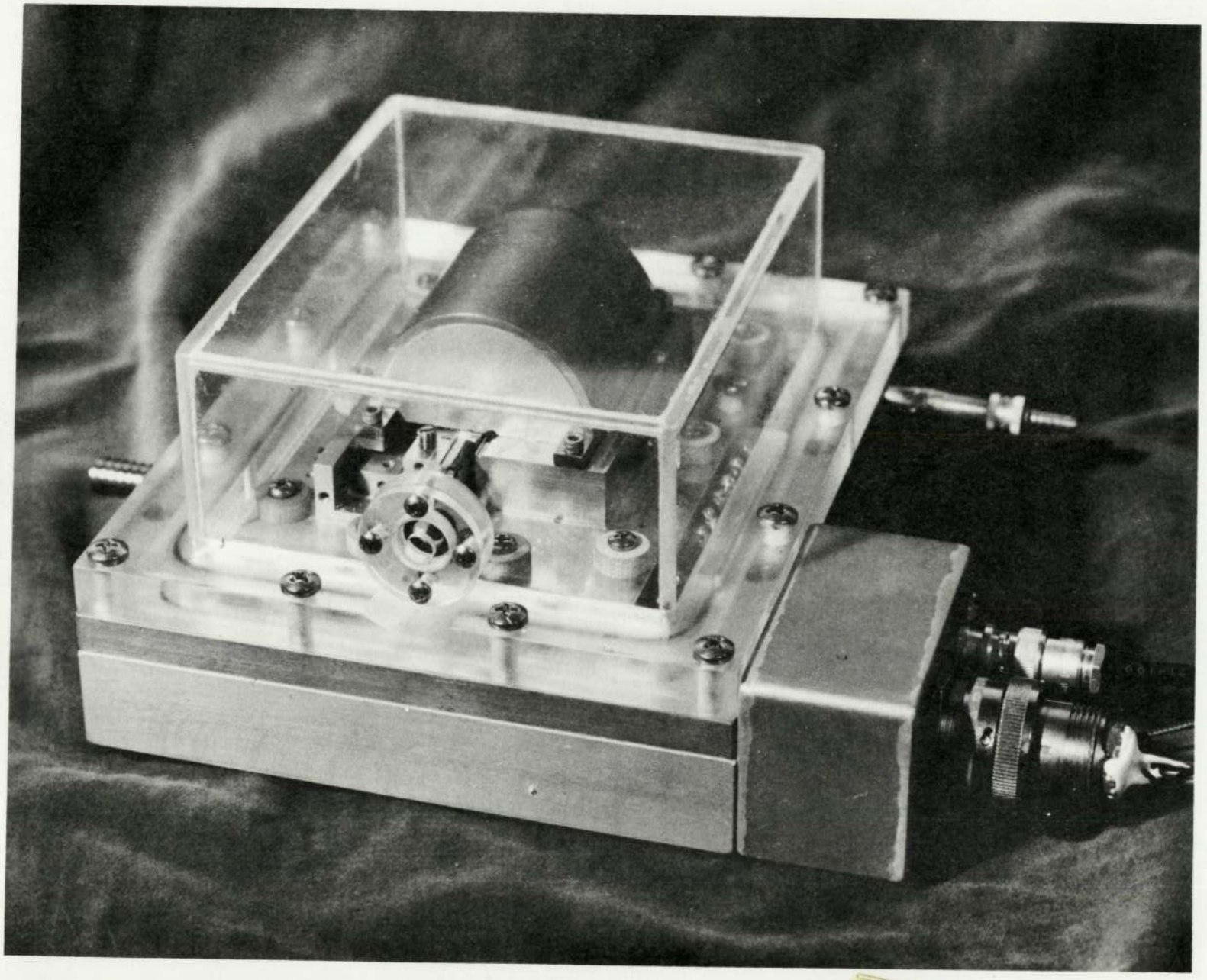

Figure 5-4. Diode Pumped Nd:YAG Device with Index Matching Solid Cylinder

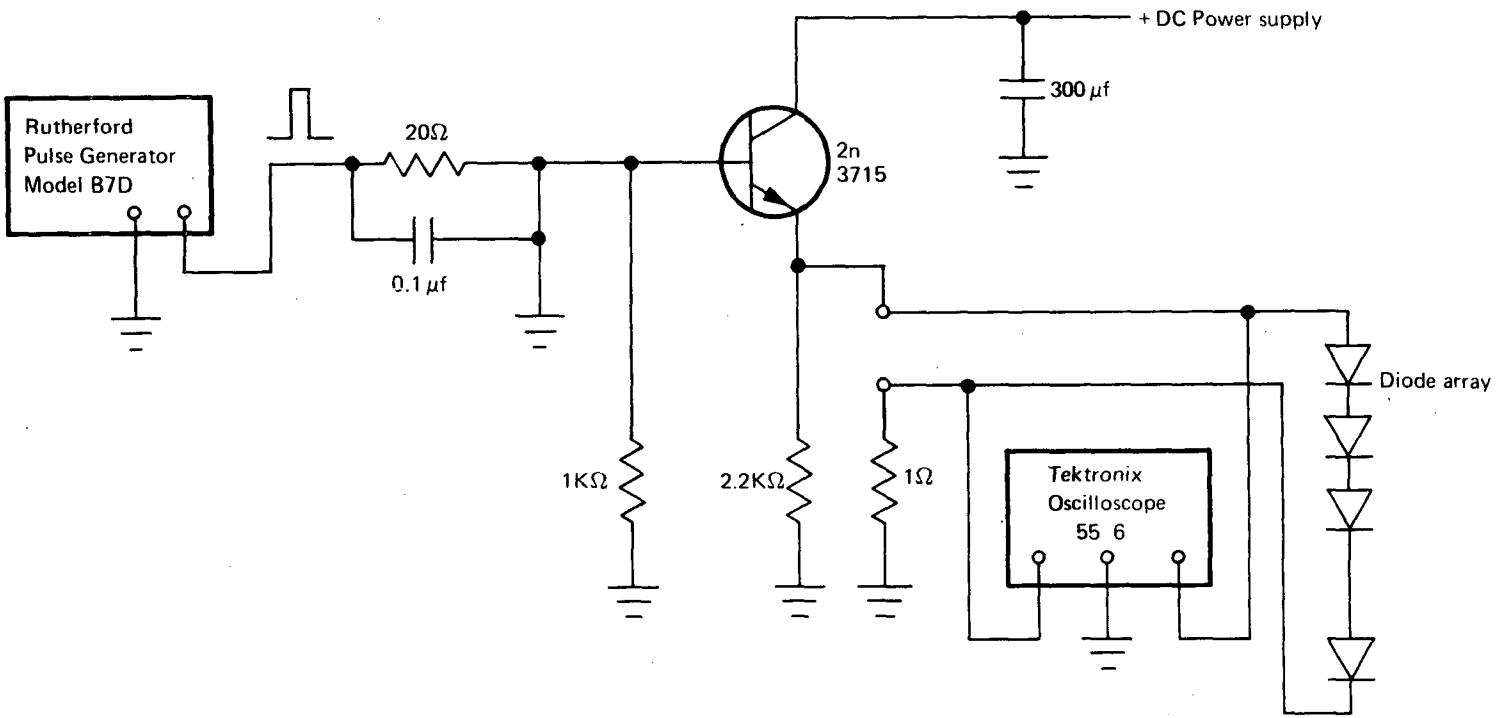

Figure 5-5. Electric Circuit for Pulsed Laser Operation

Using equation (3.2-9), the temperature dependence of laser threshold can be calculated. The results are plotted in Figure 5-6 for the following parameters:

Laser rod: 1.5mm x 56mm

Output mirror transmission: 0.1%, 0.2% and 0.4%

Average beam diameter: 0.0658cm for 0.1% output transmission laser rod; 0.553 cm for both 0.2% and 0.4% output transmission laser rod.

Doping density of Lutetium compensated Nd:YAG rod: 1.3%

Nd ion density: 1.76×10^{20} cm^{-3} [23]

Total cavity loss: 0.56%

Experimental values of laser threshold were measured in pulse operation at one percent duty cycle, minimizing the problem of diode heating. Furthermore, current density in pulsed operation could be as high as three times the corresponding CW operation without dramatic effect on the lifetime of the diode array. The results of pulsed laser threshold are shown in Figure 5-7. During the experiments, the temperature of the diode array was maintained between -5 and -8°C. The temperature variation of the diode array was due to the slight thermal conduction of the stainless steel reflector from the laser rod side to the diode side.

CW laser threshold is expected to be lower than for the pulsed laser. The relationship can be expressed by

$$P_{cw}(th) = P_{pulse}(th)\ (1 - e^{-\frac{\Delta t}{t_s}}) \qquad (5.2\text{-}1)$$

Where Δt is the input current pulsewidth in seconds and t_s is the spontaneous lifetime of the upper laser level. If the input pulsewidth was much greater than the spontaneous lifetime, the CW and pulsed thresholds would be approximately equal.

b. Pulsed Operation — Pulsed operation of the diode pumped Nd:YAG laser is useful for determining laser threshold, checking optical alignment of the laser rod and diode array, and observing relaxation oscillations. In our pulsed experiments, we applied a rectangular

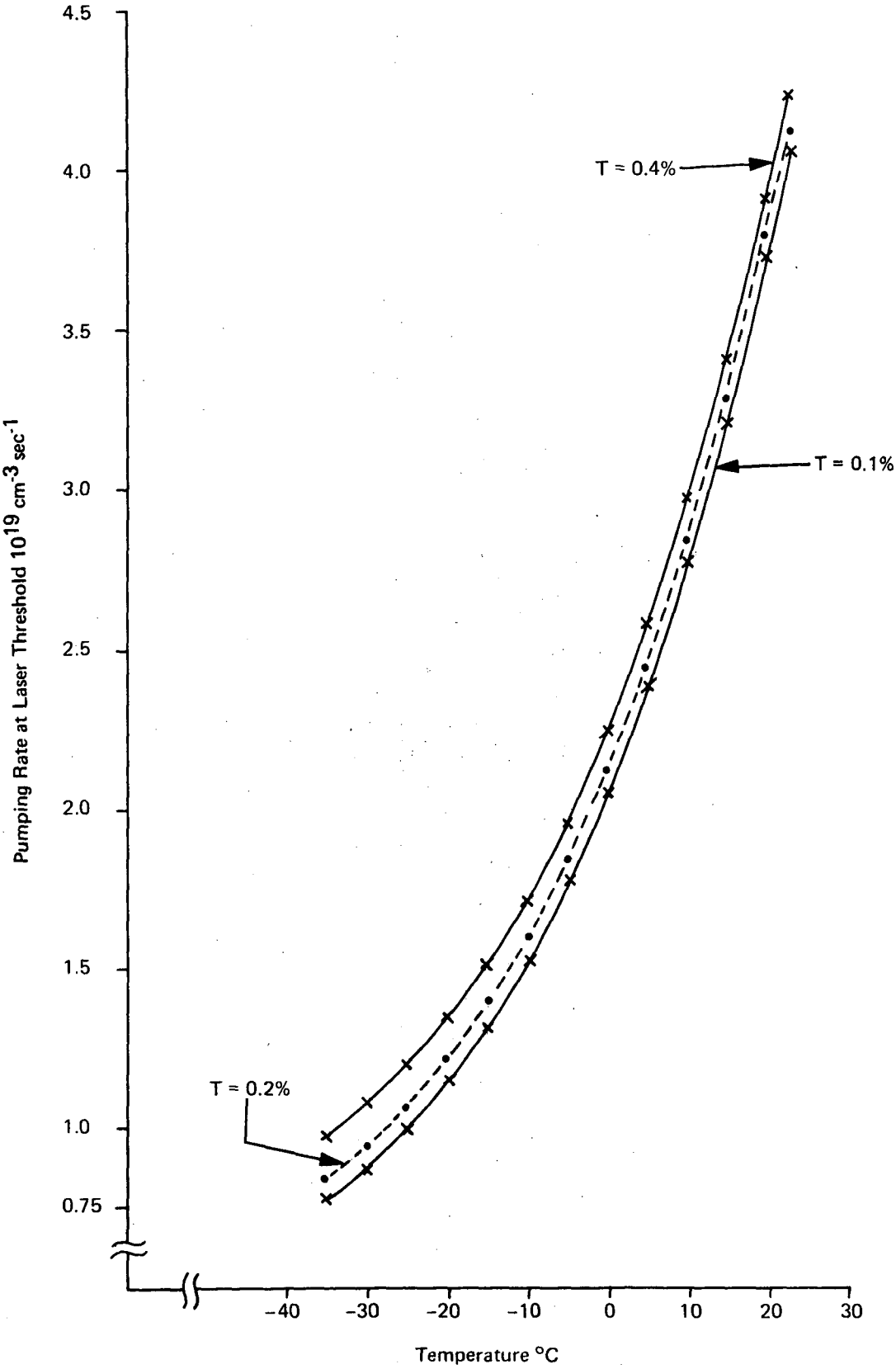

Figure 5-6. Theoretical Prediction of Nd:YAG Laser Threshold

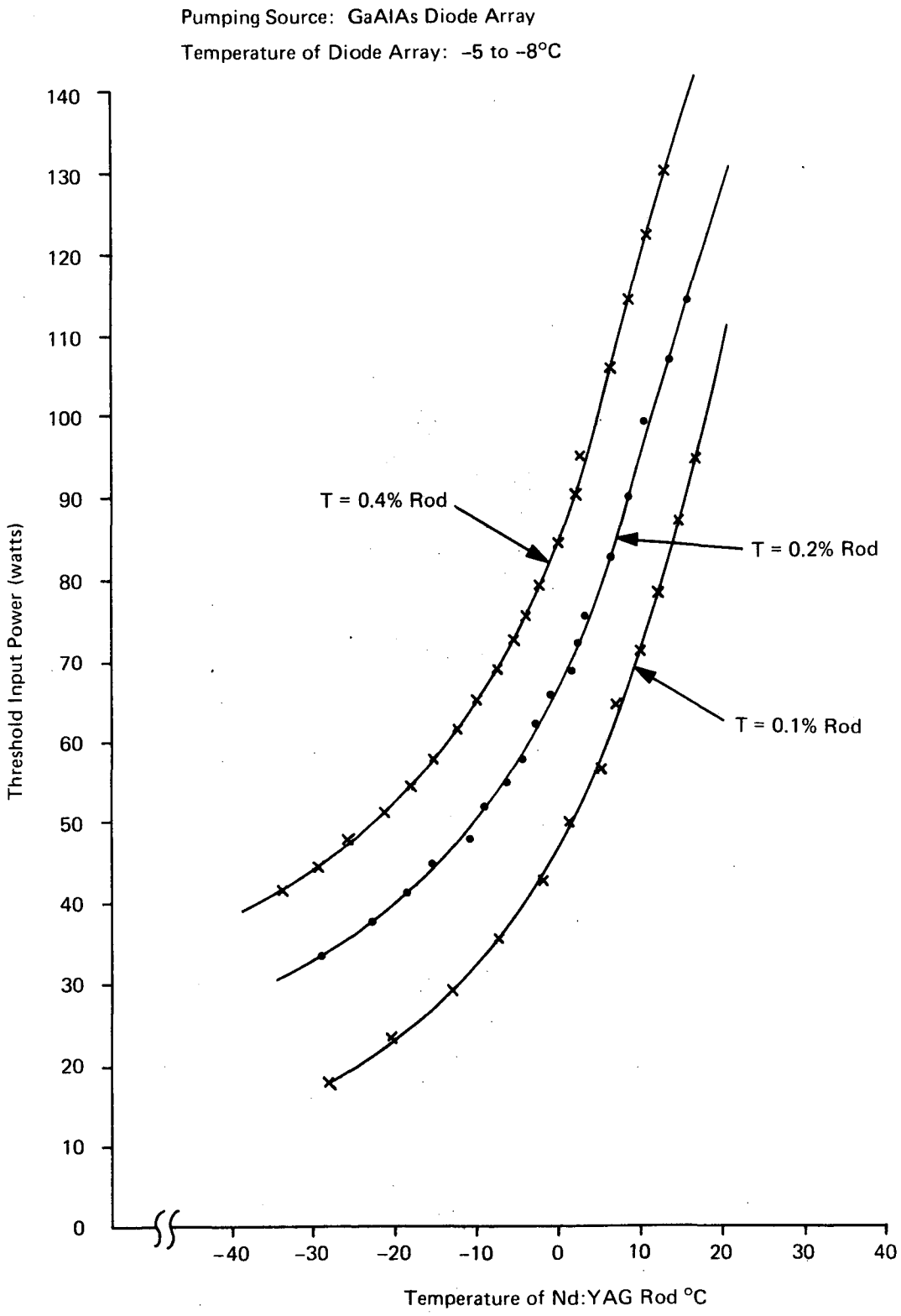

Figure 5-7. Laser Threshold vs Temperature

current pulse to drive the GaAlAs diode array. When the input pumping power was near threshold, the laser appeared in a single spike oscillation at the end of the input current pulse as shown in Figure 5-8. For a slight increase of pumping power above threshold, oscillation spikes increased to three and four as shown in Figure 5-9. For a long drive current pulse, the laser oscillations approached the steady state near the end of the current pulse as shown in Figure 5-10. The time delay of the first spike relative to the driving current pulse was also related to the pumping level; higher pumping power resulted in shorter time delays. For driving power far above threshold, the spikes became random oscillations as shown in Figure 5-11. These phenomena might indicate that the higher order transverse mode had been excited.

The relaxation oscillation frequency and decay time constant can be used for calculating the effective pumping rate and the total cavity loss by utilizing equations (3.2-23) and (3.2-24). This gives an independent way to determine the operation parameters of the laser.

Pulsed power output versus input electric power was measured with the laser rod at -27°C. The highest power obtained was 32.5 milliwatts; slope efficiency was 0.051 percent. Figure 5-12 shows the experimental results.

c. CW Operation — Threshold for the Nd:YAG laser is reduced at lower rod temperatures. Therefore, it is more favorable to operate CW at low temperature since more input power above threshold will be available for conversion to laser power output. For example, the laser threshold at -20°C requires only 28.2 percent of the room temperature pumping power. At the pumping level for room temperature threshold, the pumping rate is more than three times the threshold for -20°C operation. In our experiments, we have operated CW with the metal reflector in the temperature range from -10° to -30°C. The output couplings of laser rod were 0.1 and 0.2 percent. Optimum operating temperature of the diode array has to be determined from experiment since each diode array may have a different emission spectrum and different thermal properties. The CW power output reported was obtained with 0.2% output coupling. The rod temperature was maintained at -27°C and heat sink temperature of the diode array at -14°C. The CW experimental results are plotted in Figure 5-12 together with pulse laser results for comparison.

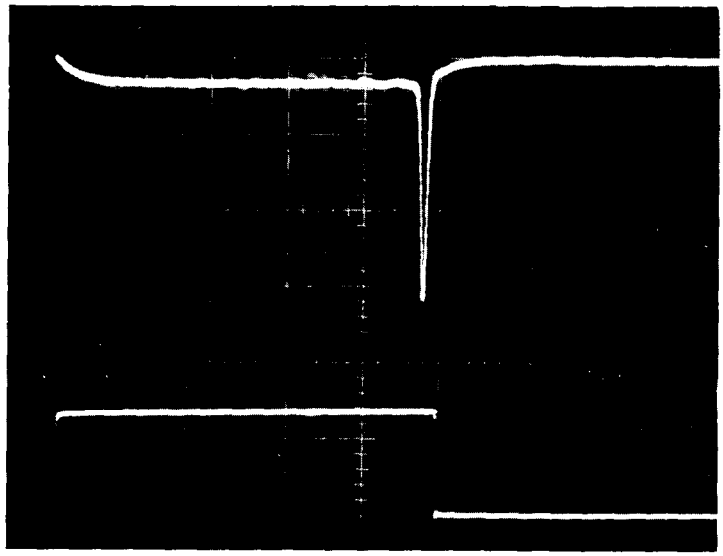

Upper Trace: Laser signal
Lower Trace: Input current pulse
Time Scale: 100 μs/div.

Figure 5-8. Laser Oscillation Near Threshold

Theoretical predictions of the optimum power output and output mirror transmission were claculated for the fundamental transverse mode. The results are plotted in Figure 5-13. It should be noticed that there are two important differences between the calculated model and the actual laser performance. The model calculated assumes a uniform transverse intensity distribution and a single oscillating mode while the actual laser beam was approximately Gaussian with a large number of axial mode oscillations.

5.3 LASER PERFORMANCE WITH INDEX MATCHING GLASS CYLINDER

To improve diode emission efficiency, the stainless steel reflector was replaced by a half-glass cylinder of refractive index 1.8. The interfaces between the diode array, the glass cylinder and the laser rod were filled by Lens Bond (n=1.55). Care was taken to eliminate any air bubbles trapped at the interfaces. Again, a precision alignment of diode array and laser rod relative to the position of glass cylinder was essential for efficient laser operation.

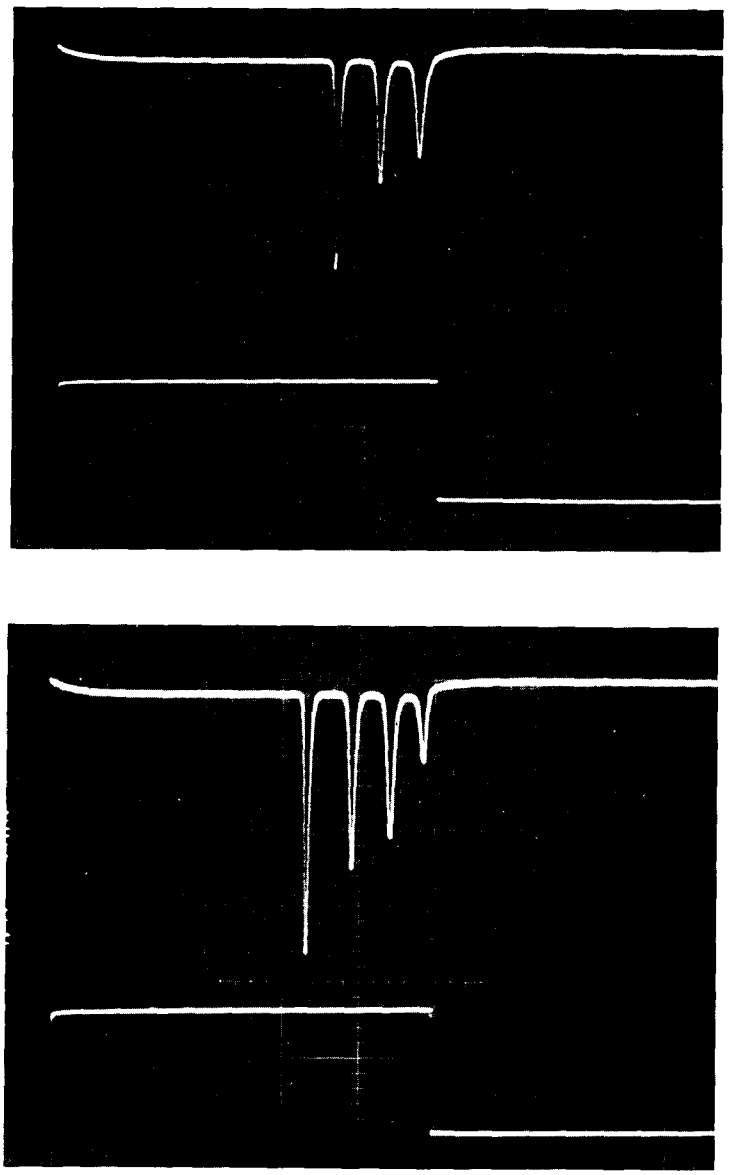

Upper Trace: Laser signal
Lower Trace: Input current pulse
Time Scale: 100 μs/div.

Figure 5-9. Laser Oscillation at Slightly Above Threshold

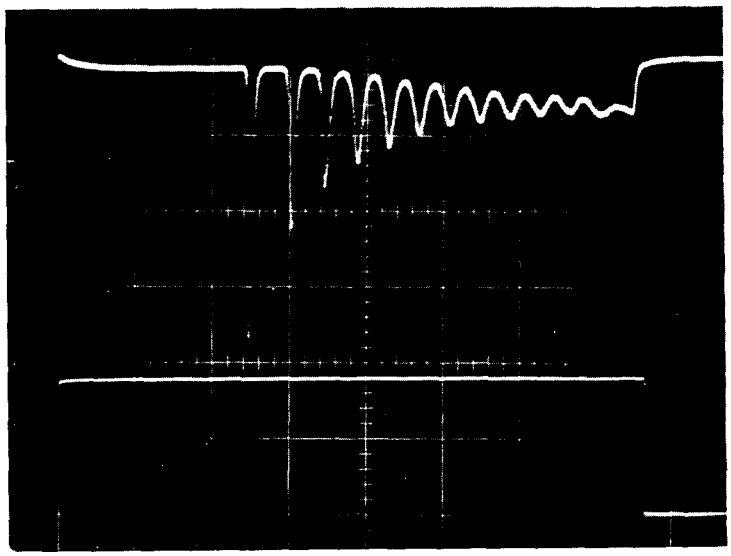

Upper Trace: Laser signal
Lower Trace: Input current to the diode
Time Scale: 100 μs/div.

Figure 5-10. Laser Oscillations Approach to the Steady State Near the End of the Long Input Current Pulse

In order to compare the pumping efficiency with metal reflector, the experiments were performed under the same temperature conditions. In all cases, the 0.2 percent transmission laser rod was used. Laser thresholds as a function of the rod temperature are listed in Table 5-1.

According to the threshold data, the coupling efficiency for the index matching cylinder shows between 159 and 199.5 percent improvement as compared with the metal pumping cavity. Theoretical calculation had predicted 323.7 percent improvement. The pulsed and CW laser output are compared to Figures 5-14 and 5-15, respectively, with previous metal reflector data. The improvement for pulsed power output was 270 percent and CW power output was 440 percent.

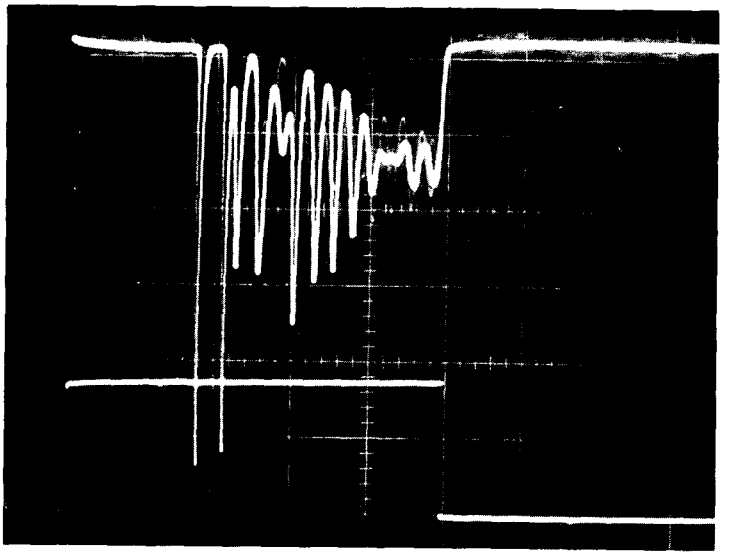

Upper Beam:	Laser signal output 50 mV/div.
Lower Beam:	Input current pulse 1A/div.
Time Scale:	100 μs/div.

Figure 5-11. Pulsed Laser Oscillation at Higher Pumping Level

Following are several reasons for the difference between the theoretical prediction and experimental results:

a. Alignment of the diode array with respect to the rod was very critical; even 25 μm misalignment measurably affected the laser threshold.

b. The original alignment of the diode emission surfaces in the array was not perfect; there was normally a 25 μm to 50 μm misalignment from a straight line.

c. There are errors in the reflector configuration and absorptions in the reflective coatings.

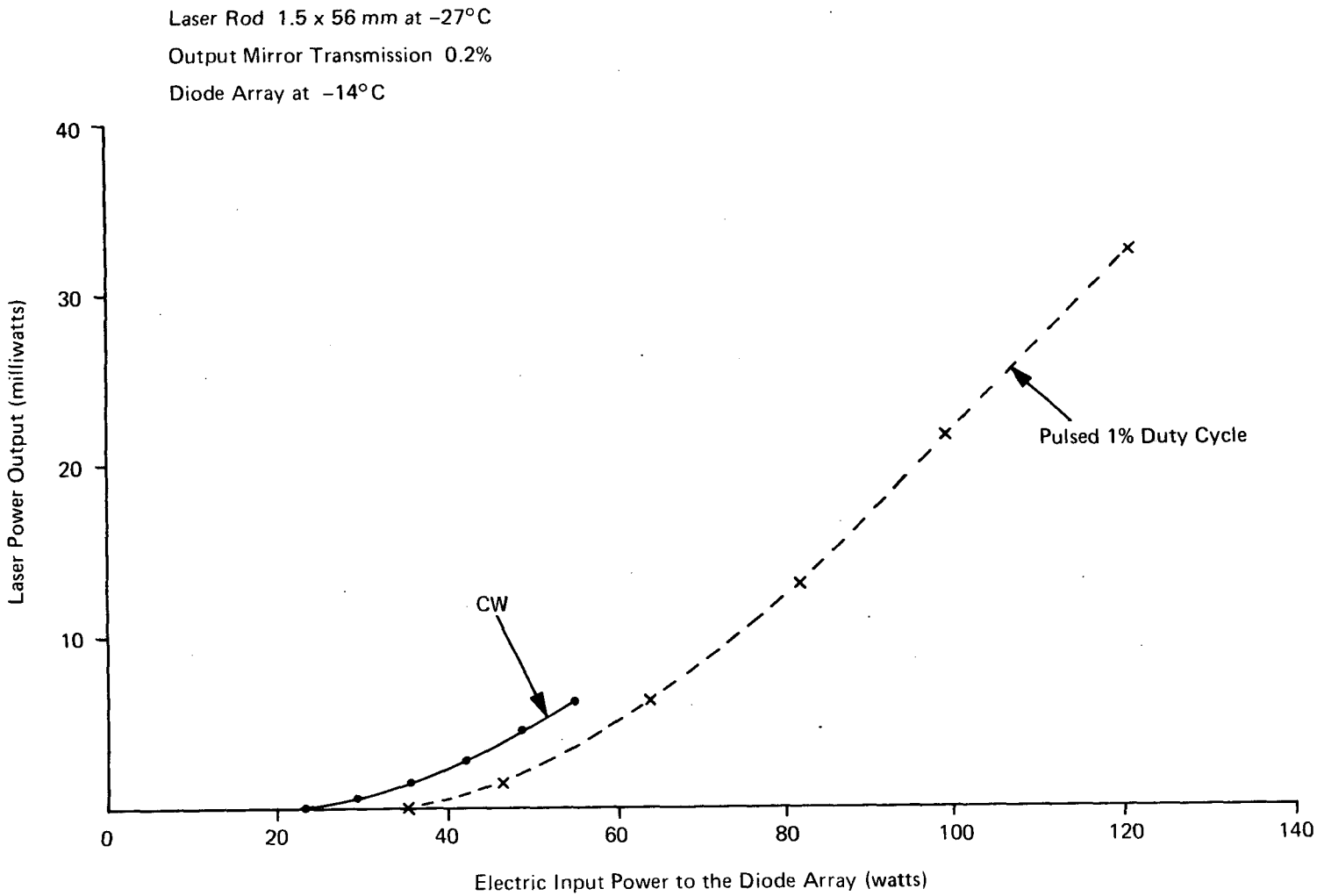

Figure 5-12. Laser Power Output with Conventional Metal Reflector

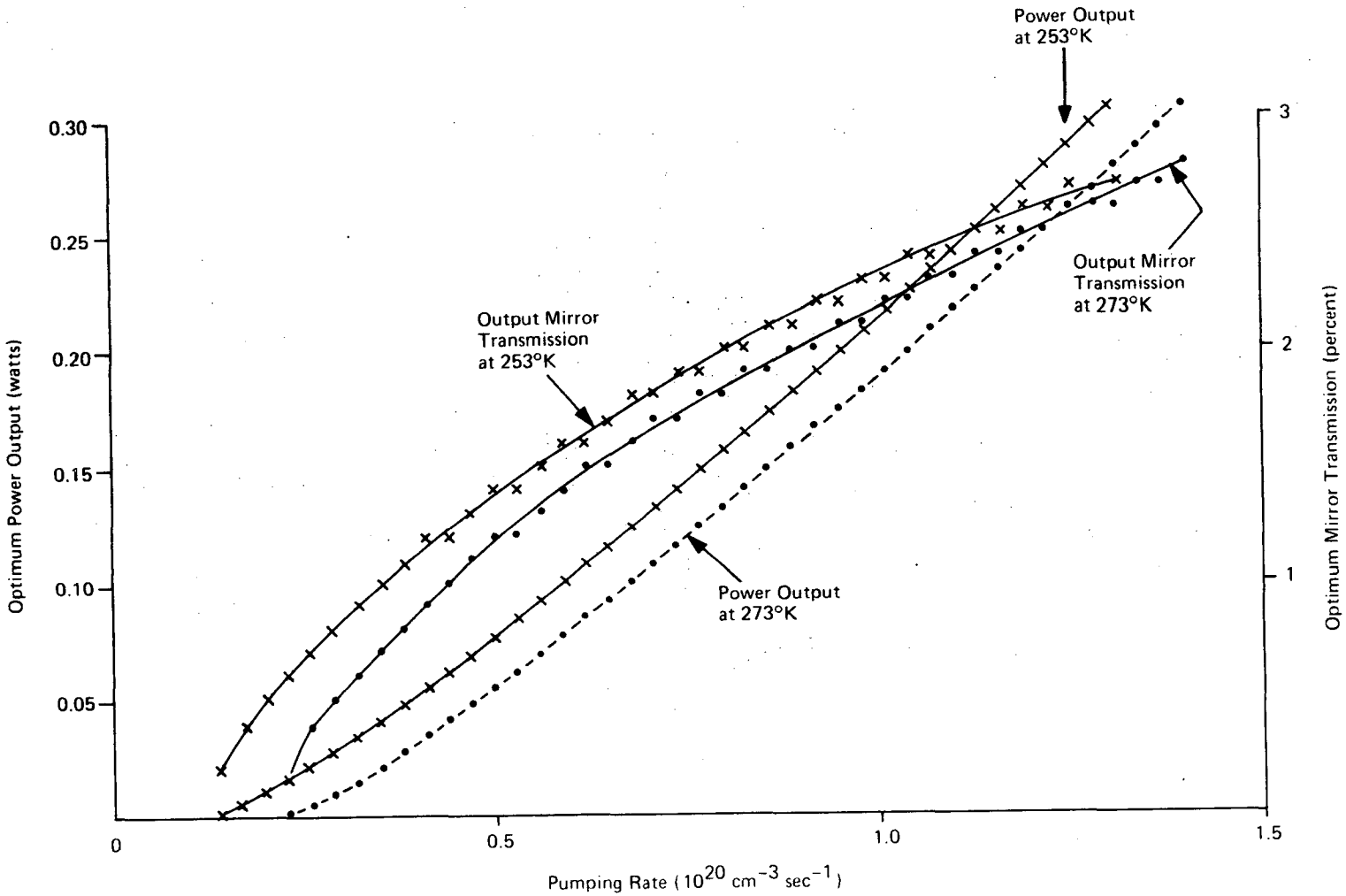

Figure 5-13. Optimum Power Output and Mirror Transmission vs Pumping Rate

Table 5-1. Comparison of Pumping Threshold Between Index Matching Cylinder and Metal Reflector

Rod Temperature	Diode Temperature	Pulsed Threshold		Improvement With Index Matching Technique (%)
		Metal Reflect.	Index Matching Cylinder	
11.7°C	-7°C	112.7 W	71 W	159
8°C	-8°C	106.5 W	64 W	166.5
6°C	-8°C	96 W	56.2 W	171
-10.2°C	-10°C	61.8 W	32.9 W	188
-23°C	-8°C	44.3 W	22.2 W	199.5
-25°C	-25°C	39.9 W	20.2 W	197.6

d. Strain in the rod due to the mismatch between rod groove and glass reflector.

e. Diode efficiency and spectrum are slightly different from the original calibrated values.

Nevertheless, the improvement of coupling efficiency with index-matching cylinder was quite significant. The CW power output had much greater improvement than the pulsed power output because the threshold for CW operation was lower than the pulsed operation. If a higher liquid were used for filling the interfaces, the coupling efficiency would be further improved.

5.4 LASER MODULATION

Light output of a diode pumped Nd:YAG laser can be directly modulated by varying the drive current to the diode. For amplitude modulation, the maximum depth of the output modulation depends on the effective pumping rate, cavity loss and spontaneous lifetime of the upper laser state. In order to understand this modulation effect as a function of frequency, we have calculated the modulation depth and phase shift under the assumptions that the laser was operated at -25°C and pumped at 1.2 times the threshold. Figure 5-16 is the calculated modulation depth and phase shift versus modulation frequency. The peak resonant frequency is at 23.2 kilohertz. In Figure 5-17, the frequency and phase at maximum modulation depth are plotted as a function of laser rod temperature. It may be of interest to notice that the phase shift is approximately 90 degrees out of phase from the modulation signal at all the maximum modulation output.

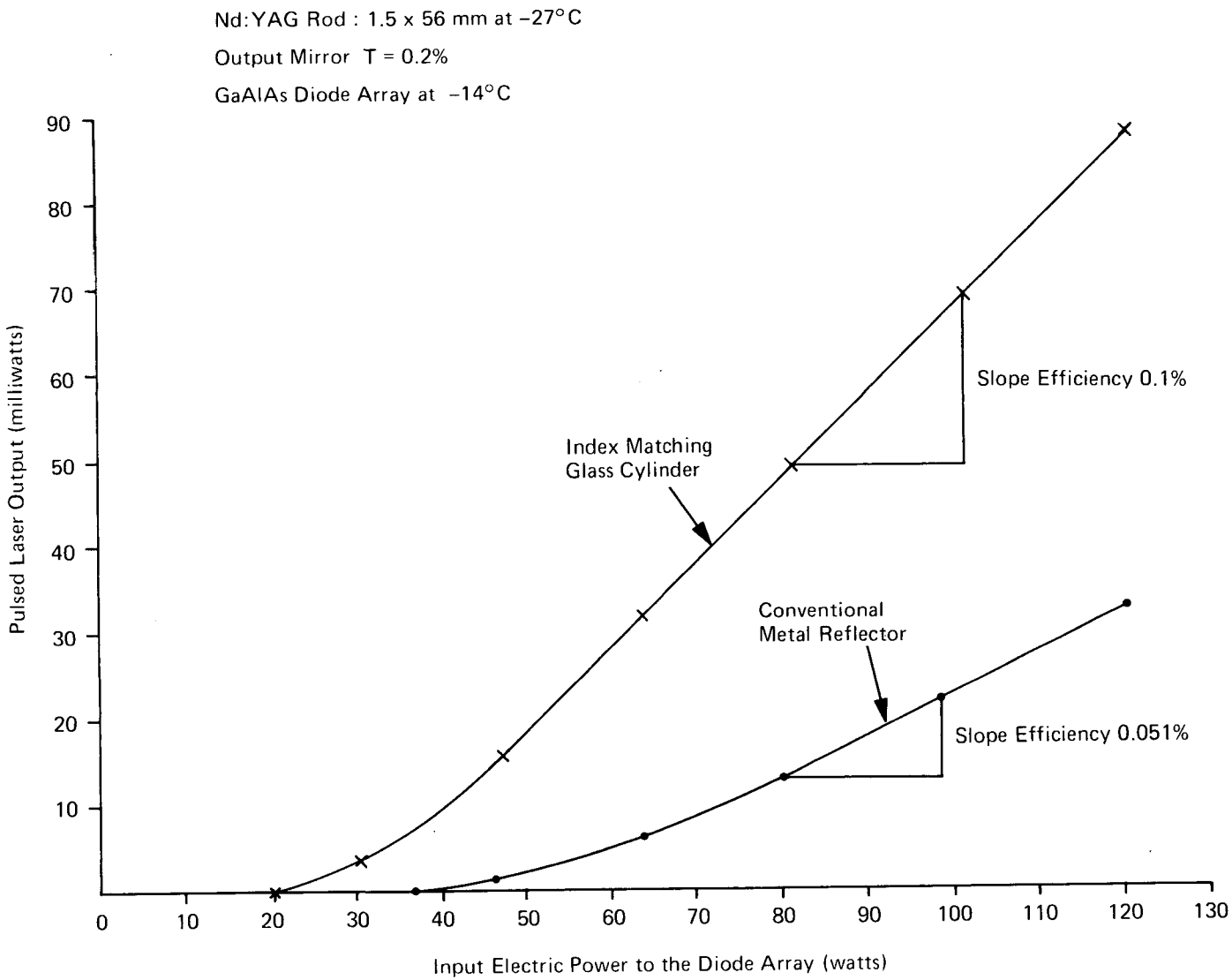

Figure 5-14. Comparison of Pulsed Laser Output Between Index Matching Cylinder and Metal Reflector

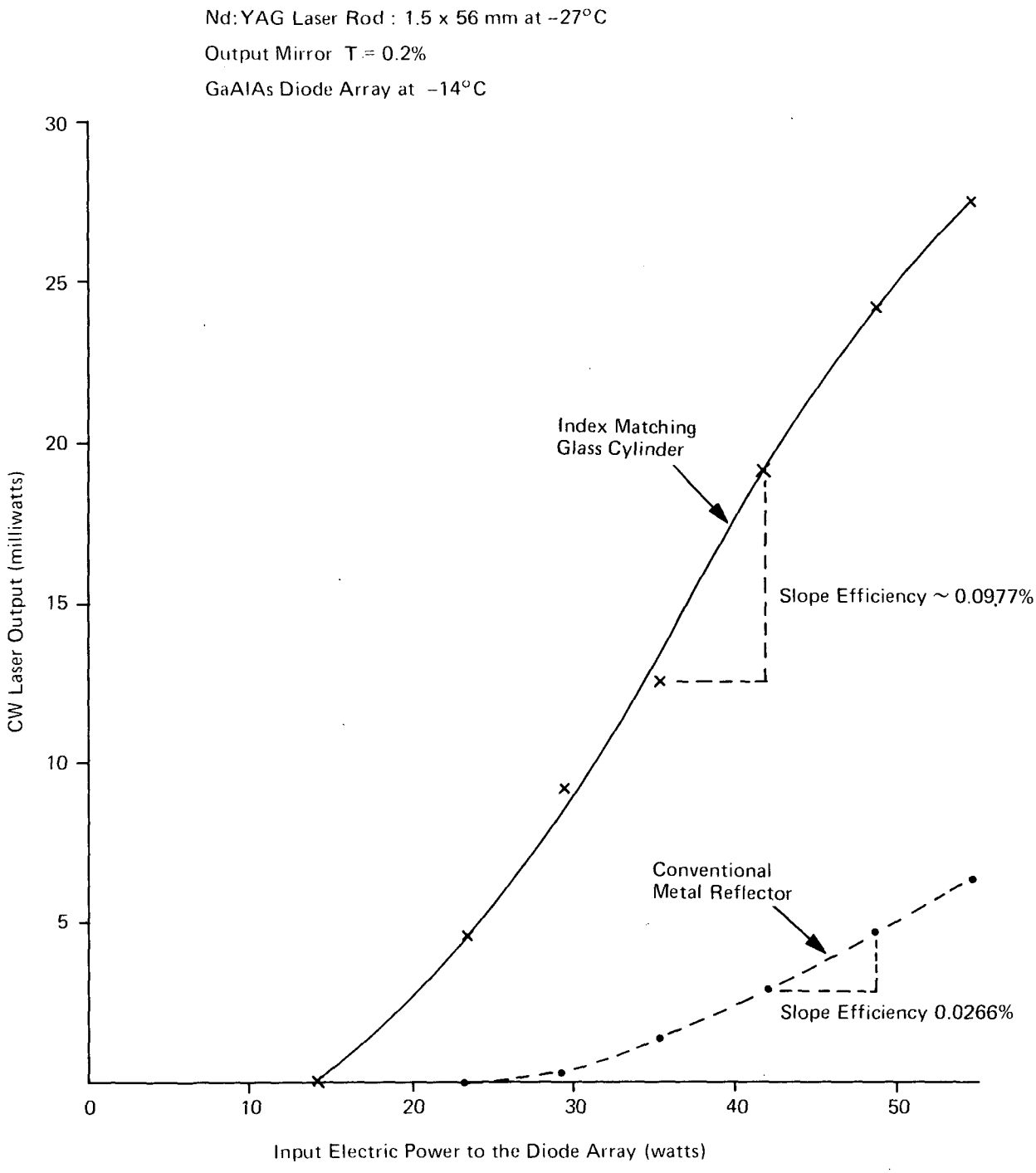

Figure 5-15. Comparison of CW Laser Output Between Index Matching Cylinder and Metal Reflector

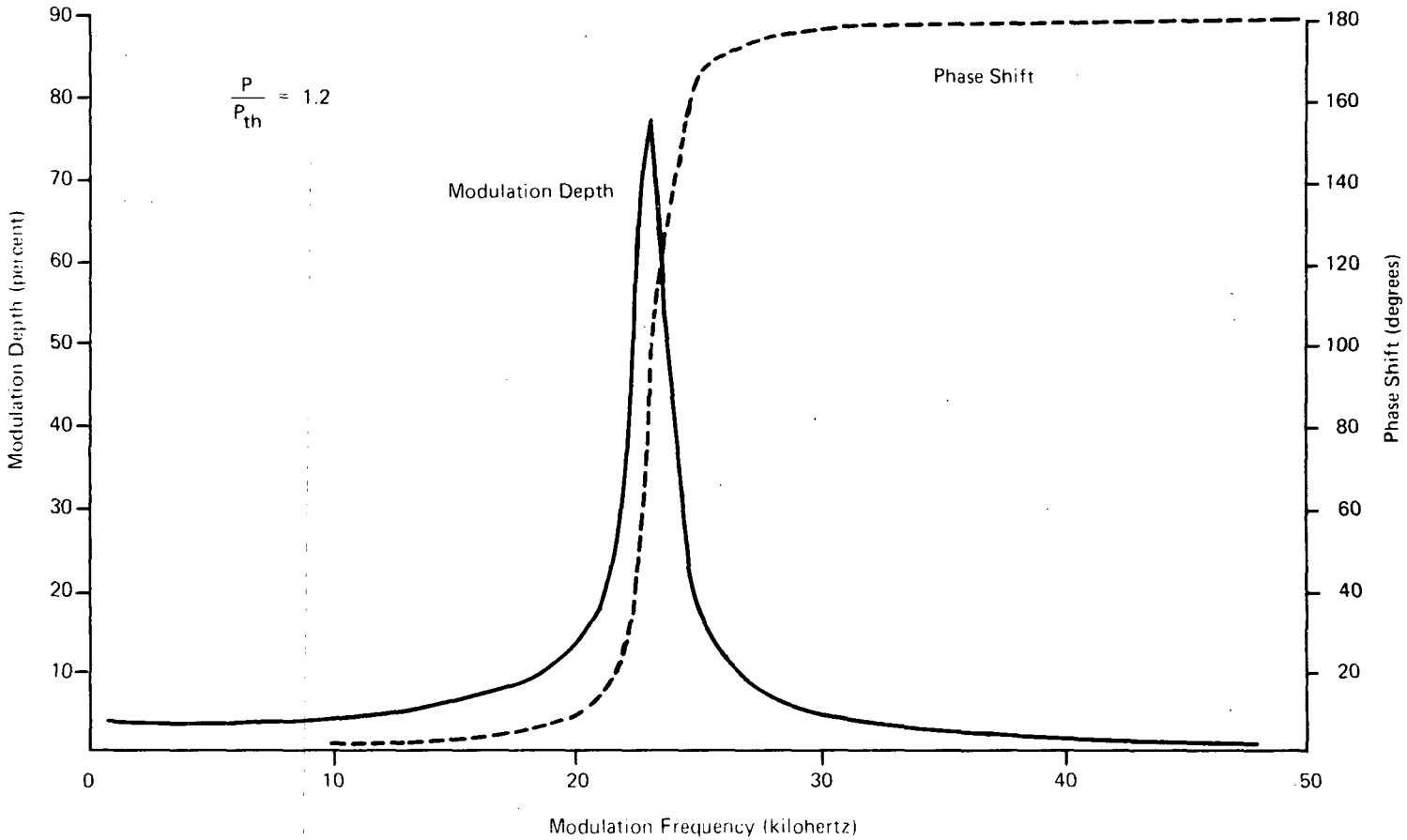

Figure 5-16. Modulation Depth and Phase Shift vs Modulation Frequency

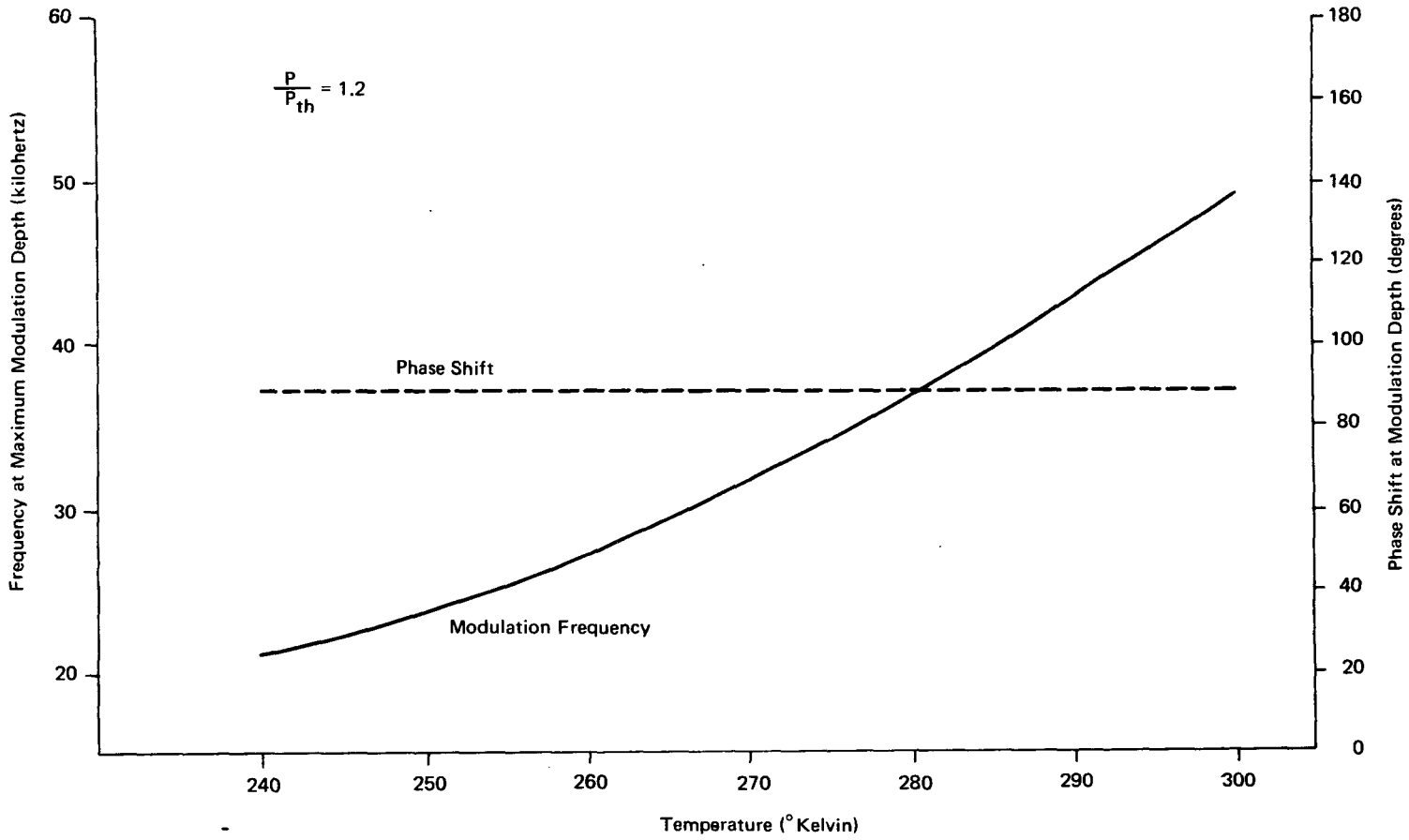

Figure 5-17. Temperature Dependence of Frequency and Phase Shift vs the Maximum Modulation Depth

In the experiment, a 1.5mm x 56mm Lutetium compensated Nd:YAG rod was used with an index-matching glass cylinder as discussed in the previous section. The laser rod temperature was maintained in the vicinity of -25°C and the heat sink of the diode array at -1°C. The laser was operated continuously with one milliwatt output at 12 percent above the threshold. The laser beam appeared to be a TEM_{00} mode as viewed with an image converter; however, the intensity profile across the beam was not measured.

The modulation effect may be separated into two frequency ranges; the regular spiking mode, where the modulation frequency depends only on the flourescent life time of the upper laser state. The nonlinear rate equations do not explain this phenomena, and the resonant amplitude modulation, which is predicted by the nonlinear rate equations on the assumption of a small signal perturbation.

When the modulation frequency approaches the inverse of the spontaneous lifetime; the laser oscillations appear as sharp spikes at regular time intervals, similar to a repetitively Q - switched laser signal. Figure 5-18 shows the laser modulation at 3.125 kilohertz - slightly less than the spontaneous relaxation frequency. The laser produced a sharp spike 60 microseconds after the modulation signal, followed by two small relaxation oscillations. If the modulation frequency is exactly at the spontaneous relaxation frequency, we obtained only a repetitive sharp spike with rise and fall time less than 10 microseconds. Figure 5-19 shows the laser modulation at 5 kilohertz. The spike is delayed about 80 microseconds modulation signal. For a higher modulation index (ac modulation current 50 percent of the dc current) at 5 kilohertz, the peak power of the spikes was about 97 times the average CW power output in agreement with Danielmeyer and Ostermayer's results[25].

For the resonant amplitude modulation at the frequency for which the output modulation depth is maximum, the laser followed the same waveform and frequency as the modulation signal. Figure 5-20 shows the laser modulation at 22.2 kilohertz. The input modulation index was 10 percent and the output modulation depth was 44.5 percent. Theoretical calculation had predicted that the frequency for maximum resonant amplitude modulation was 23.3 kilohertz for a pumping level of 1.2 times threshold. This agrees with the experimental results within 5 percent. If the frequency is detuned from the resonant frequency, the laser oscillations becomes random and unstable. However, at higher modulation index, the laser output again becomes stable and follows the waveform of modulation signal. For frequencies beyond 50 kilohertz, the modulation signal has negligible effect on the laser output.

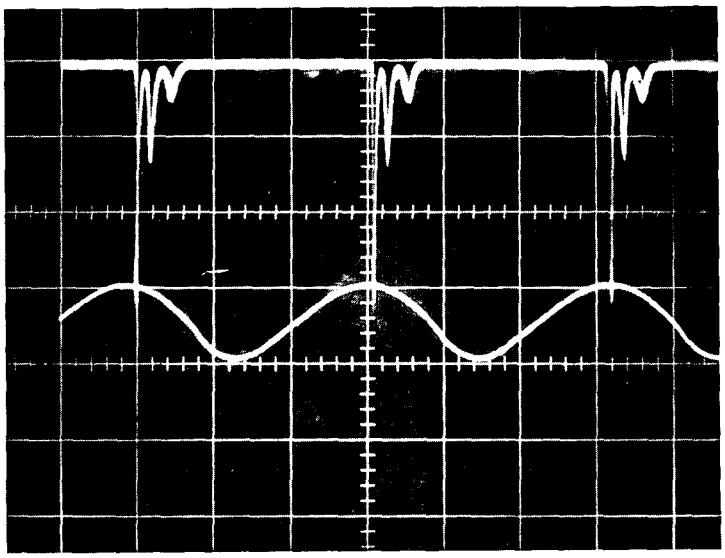

Upper Beam:	Laser signal 5 mV/div.
Lower Beam:	Modulation voltage to the diode array. DC input current was 0.3A before modulation and the average current was 0.9A after applied modulation signal.
Time Scale:	100 μs/div.

Figure 5-18. Laser Modulation at 3.125 Kilohertz

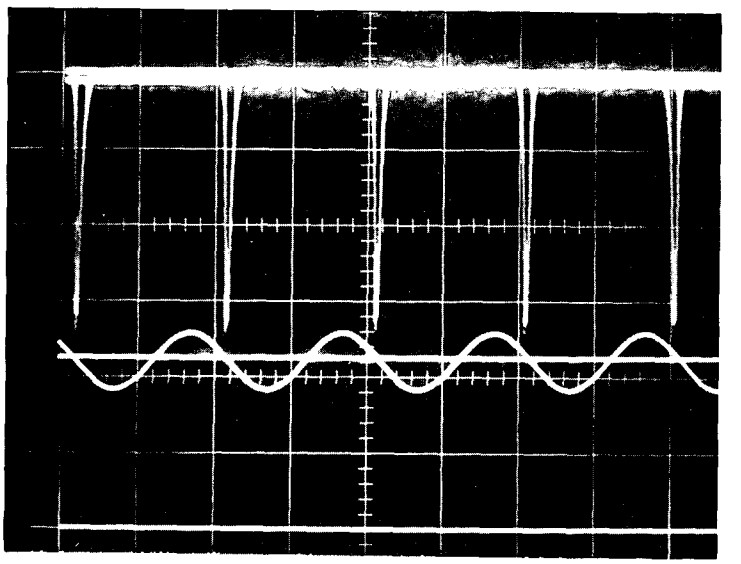

Upper Beam:	Laser signal output 100 mV/div.
Lower Beam:	Input current to the diode array 0.4A/div.
Time Scale:	100 μs/div.

Figure 5-19. Laser Modulation at 5 Kilohertz

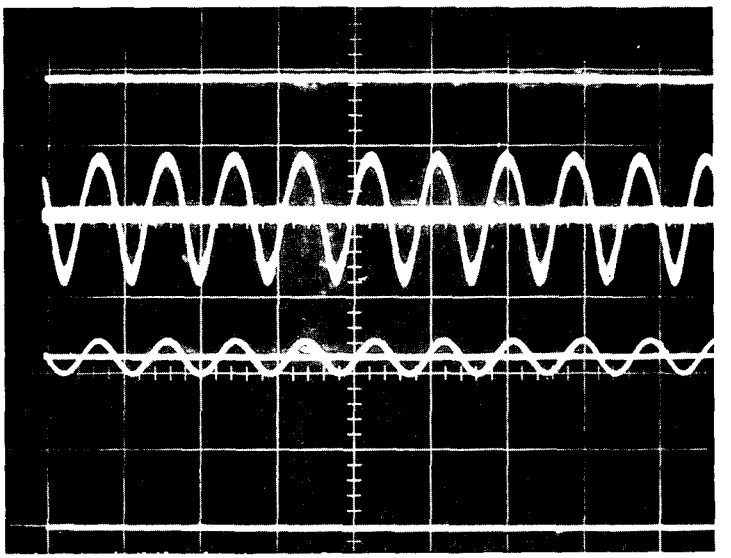

Upper Beam:	Laser signal output 10 mV/div.
Lower Beam:	Input current to the diode array 0.4A/div.
Time Scale:	50 μs/div.

Figure 5-20. Laser Modulation at 22.2 Kilohertz

Laser modulation produced by a pumping intensity variation has shown two types of modulation effects. In the resonant AM mode, the modulated output followed exactly the same waveform as the input signal. Its frequency depends on the pumping level and cavity loss. In the regular spiking mode, the modulation frequency depends only on the flourescent lifetime of the upper laser state. Peak powers were about 100 times the CW power. This should be very useful for second harmonic generation as the efficiency of conversion is proportional to the square of the intensity at the fundamental frequency.

In this section the selection basis of parameter values is described. The characteristics of major laser components are considered in order to relate them to the overall device design.

6.1 DIODE PUMP

One of the outstanding advantages of diode pumping is the absence of heat due to absorption of useless pump radiation. Instead, the pump emission is carefully matched to a Nd^{3+} absorption which populates the upper laser level. Several absorption bands satisfy this requirement with high efficiency [26] so the selection can be made on other criteria. The energy difference between the absorbed pump photon and the laser photon will result in crystal lattice heating. Therefore, it would be desirable to pump at wavelengths not much shorter than the laser emission. The absorption resulting in direct excitation from the ground state to the upper laser level is at 8700Å and for many reasons related to the GaAlAs LED material is attractive. At the low pumping flux achieved in diode pumping, the 3-level aspect of this transition presents no limitation. The efficiency and thermal conductivity, as well as the emission wavelength of GaAlAs, are dependent on the aluminum concentration in the crystal. The thermal conductivity decreases with increasing aluminum concentration. The emission wavelength decreases and the efficiency is constant over the wavelength range from 7500Å to 9000Å; for shorter wavelengths, it also decreases. For all of these reasons the 8700Å absorption is attractive; unfortunately, this absorption is weaker by more than a factor of two than the absorption at 8100Å. Therefore, this 8100Å nearest wavelength alternative was selected as the pumping transistor. The aluminum concentration of the GaAlAs was adjusted to match the peak absorption, and the gradients were controlled to match the absorption bandwidth. To maximize diode efficiency, a wide range of doping densities were explored in the investigation of its effect on interval quantum efficiency and absorption. Contact technology was improved to reduce chronic losses. A minimum bandgap structure was grown to reduce the bulk absorption of the material overlaying the junction region. The thickness of the n-type layer through which the pump light is emitted was minimized.

The thermal conductivity of the individual diodes was improved over previous material by growing the "n-up" structure. Only a thin ($\sim 35\ \mu m$) epitaxial

layer of GaAlAs is grown on a GaAs substrate which serves as the thermal conduction path to the heat sink. The array consists of 20 diodes connected electrically in series, bonded on a hybrid circuit board. The board is made of beryllium oxide, an electrical insulator with high thermal conductivity. The diodes are soldered to this board and the board to the heat sink, thereby minimizing thermal discontinuities.

Diode design parameters which are available within this basic array structure of the form factors are operating current and operating temperature. The length of the diodes used in this program was 0.25 cm. This length was chosen on the basis of material homogeneity and handling requirements. It proved to be adequate from the standpoint of diode yield and minimum number of array elements. The array length was designed to match the length of the laser mode, i.e., the laser rod. The rod length used was the maximum thought feasible for the 0.15 cm rod diameter without excessive breakage. The diode emission width was chosen to fall within the laser mode diameter. A constant stripe of 87μm was applied to the n-type diode surface to accommodate the 75 μm ball diameter of the thermal compression bonded wire leads. Table 6-1 shows a comparison of pumping efficiencies (defined as 100x absorbed light ÷ emitted light) for different rod and mode diameters and diode widths. These results show that the choice of diode width should be based on thermal behavior rather than mode diameter.

Since long operating life is one of the characteristics sought, the current density chosen for diode operation was the maximum which intuitively appeared to offer this life. Observation of low duty rate pulsed emission and continuous operation under identical current density show similar efficiency up to about 115A/cm^2. Above that point the efficiency of the continuously excited diodes drops below the pulsed efficiency indicating an increase in junction temperature. Life tests at 115A/cm^2 show the desired expectancy.

The diode array operating temperature must be established before the material is grown since the emission wavelength is dependent on it. Generally, diode performance is better at lower temperatures but, depending on the cooling system available, it will probably be necessary to choose an operating temperature near ambient to minimize power expenditure. Typical power requirements for thermo-electric coolers are shown in Figure 6-1 and 6-2. The temperature chosen for the laser rod operation is not significantly influenced by the heat load presented by the rod. At most this would be of the order of 0.1 watt. Therefore, the rod operating temperature will be chosen as low as is compatible with the application.

Table 6-1. Pumping Efficiency of Circular Cylindrical Reflector as Function of Diode Emission Width and Laser Rod Size

0.0254 cm. Emission Width of the GaAlAs Diode				
Radius of the Laser Rod	Pumping efficiency in the fundamental mode volume			
	R_m = 0.02765 cm	R_m = 0.0329 cm	R_m = 0.0391 cm	R_m 0.0465 cm
0.1 cm	14.9%	18.2%	22%	26.7%
0.075 cm	17.3%	21.2%	25.7%	30.9%

0.0508 cm Emission Width of the GaAlAs Diode				
Radius of the Laser Rod	Pumping efficiency in the fundamental mode volume			
	R_m = 0.02765 cm	R_m = 0.0329 cm	R_m = 0.0391 cm	R_m = 0.0465 cm
0.1 cm	14%	17.7%	21.7%	26.4%
0.075 cm	16.3%	20.5%	25.1%	30.5%

R_m: radius of the TEM_{00} mode volume.

6.2 LASER RESONATOR

The resonator parameters available for design are mirror curvatures and reflectivity and resonator length. Given a power output requirement and a volume excitation rate, the appropriate mode volume and output reflectivity can be selected from curves like those in Figures 6-3 and 6-4. Mode control is achieved by making diffraction losses on desired modes preferentially low. There exists an additional degree of control in diode-pumped losses since the excitation rate is not homogeneous throughout the rod but is much higher in the volumes where the pump is imaged. For some arrays tested, this control alone was sufficient to limit operation to TEM_{00} mode but this was only in exceptional cases. Positive control of transverse mode should be achieved if the diffraction loss on the undesired mode with the lowest threshold is a factor of two greater than the desired mode and equal to about half the optimum output transmission. All resonators tested as part of this program have the mirrors as an integral part of the laser rod. For applications requiring mode locking at least one of the mirrors must be separated from the

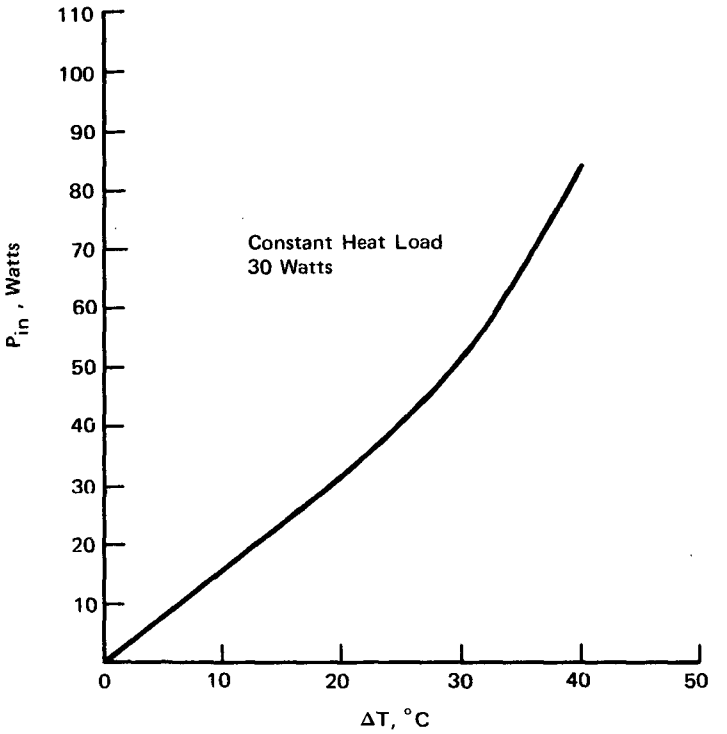

Figure 6-1. Cooler Drive Power vs Diode Operating Temperature

laser rod. The laser gain achieved at the conclusion of this program is not great enough to accomodate the extra loss incurred at the anti-reflection central surfaces and still operate continuously.

6.3 PUMPING CAVITY REFLECTOR

In cylindrical pumping reflector, the separation between laser rod and diode array should be as small as possible for efficient critical coupling. A practical separation between the diode array and laser rod is 5 mm, and based on ray-tracing calculations, a diameter of 5 cm was chosen for the solid glass reflector. Thus, the separation is only one tenth of the reflector diameter. Pumping efficiency at this separation but slightly varying laser rod in the vertical position has been calculated and the results listed in Table 6-2. It was found that the best pumping efficiency occurs for the rod located 200 microns above the x-axis for the hollow metal reflector and 300 microns above the x-axis for index matched solid cylindrical reflector.

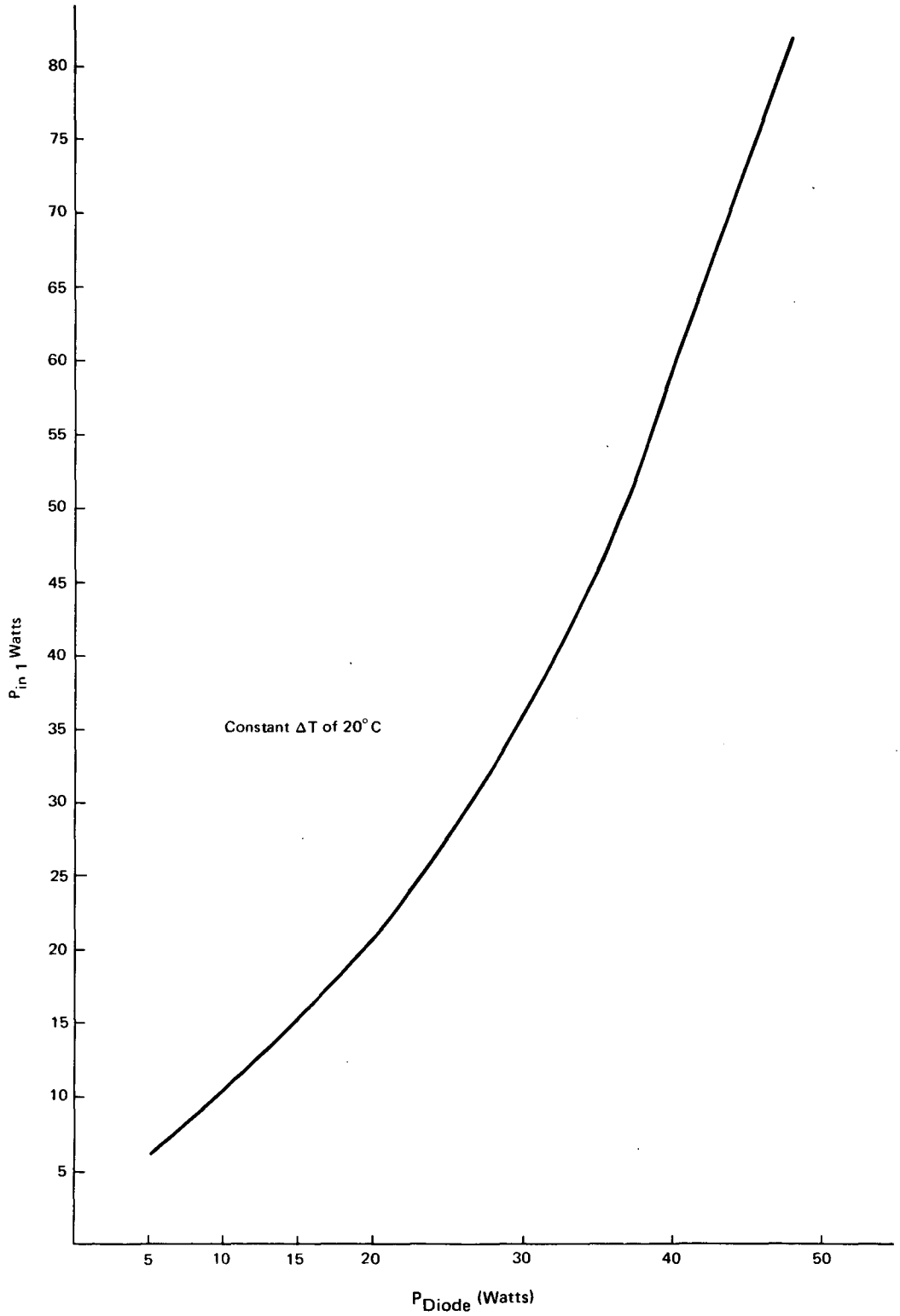

Figure 6-2. Cooler Drive Power versus Diode Drive Power

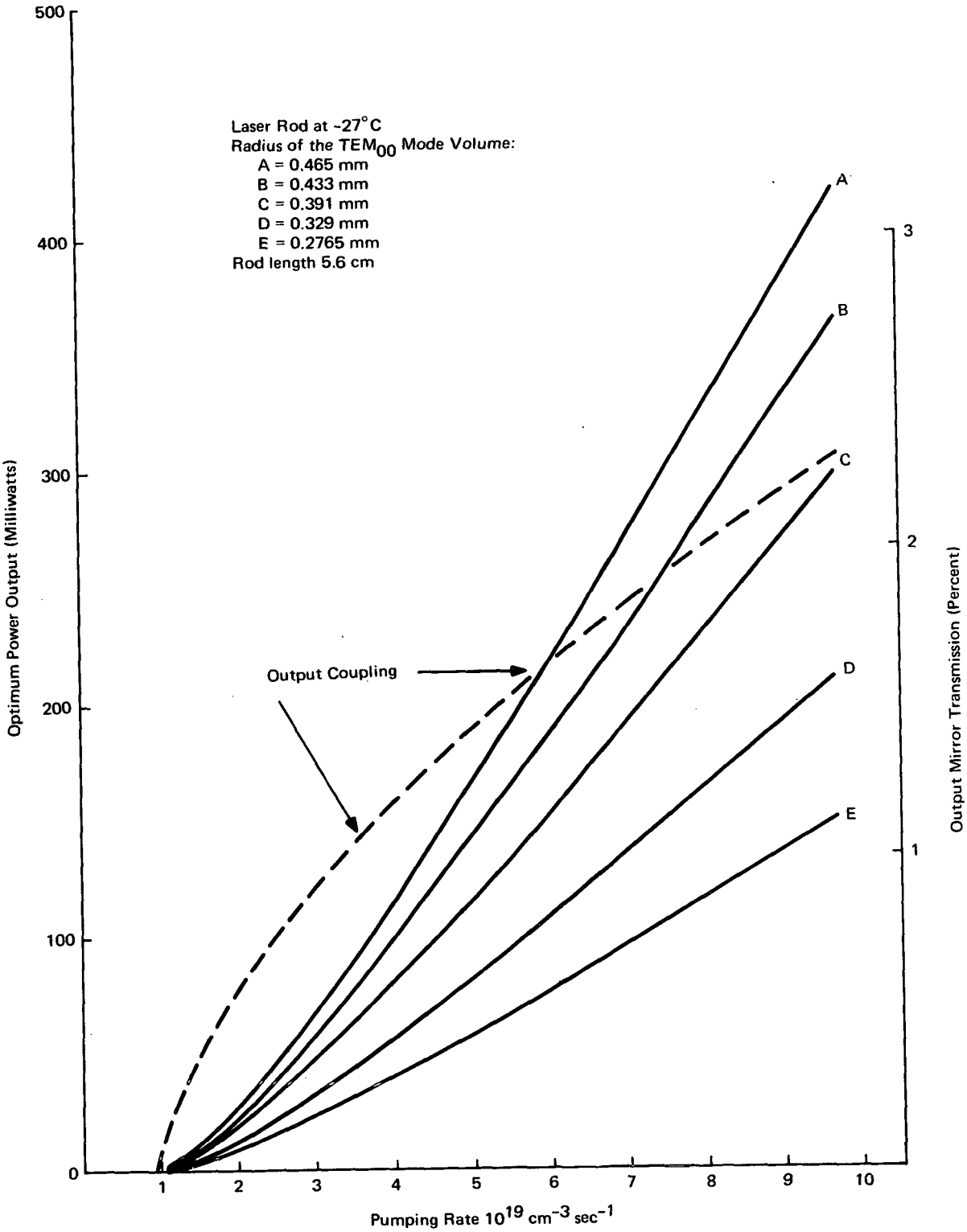

Figure 6-3. Output Power and Coupling at -27°C Operation

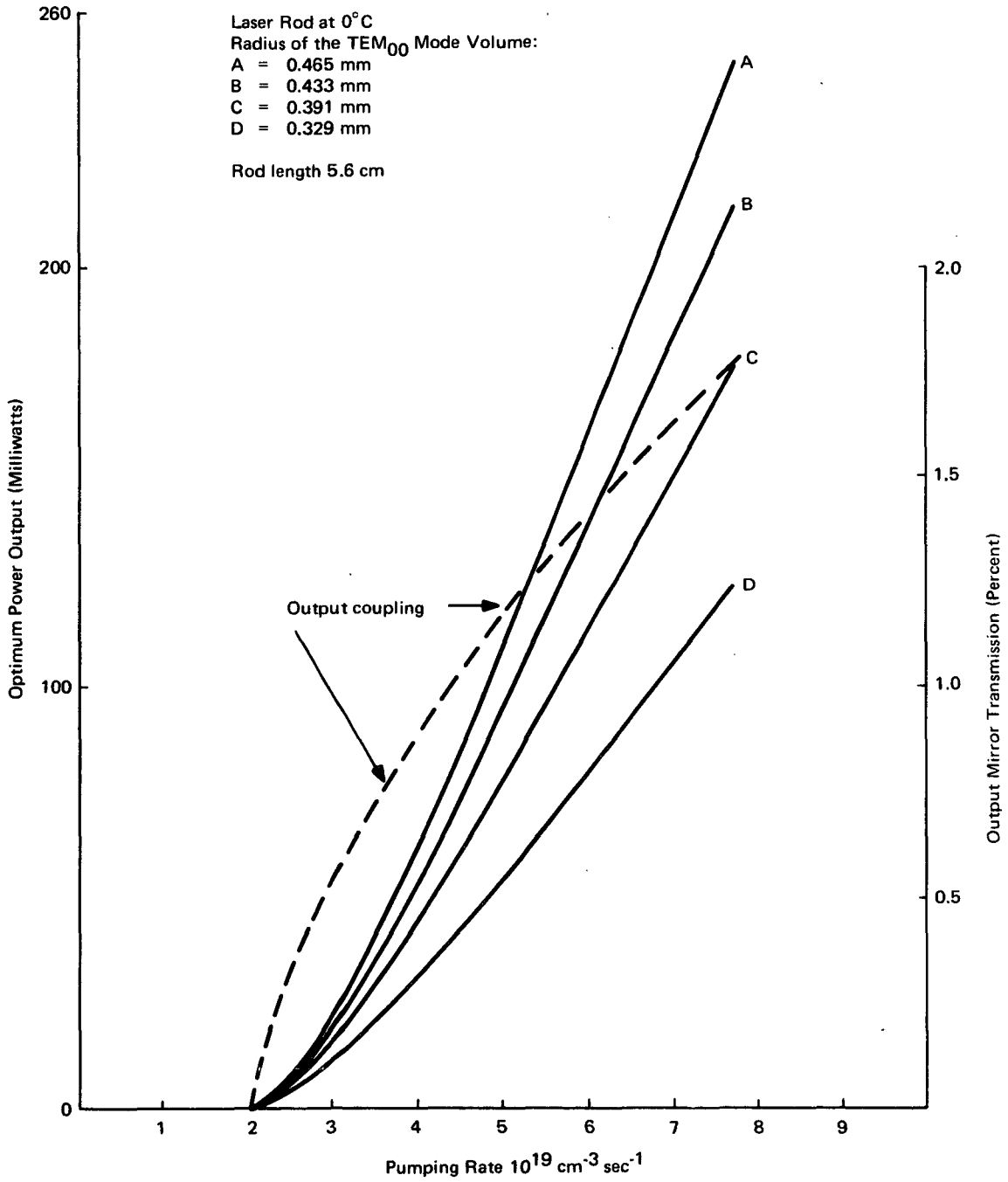

Figure 6-4. Output Power and Coupling at 0° Operation

Table 6-2. Pumping Efficiency of Circular Reflector as Function of Laser Rod Location

Location of Laser Rod (x, y) in cm	Pumping efficiency in the fundamental mode volume (%)		
	Metal Reflector $n_1 = 1$, $n_2 = 1.82$	Glass Cylinder $n_1 = 1.55$, $n_2 = 1.82$	YAG Cylinder $n_1 = 1.82$, $n_2 = 1.82$
(-0.25, -0.020)	19.1	15.2	11.9
(-0.25, -0.010)	20.3	19.5	16.5
(-0.25, 0)	21.2	22.9	21.1
(-0.25, 0.010)	21.7	24.9	24.2
(-0.25, 0.020)	21.99	25.9	25.8
(-0.25, 0.030)	21.97	26.1	26.2
(-0.25, 0.04)	21.5	25.5	25.5

Radius of the laser rod R = 0.075 cm

Radius of the mode volume R_m = 0.0329 cm

Section 7. CONCLUSIONS AND RECOMMENDATIONS

The experiments performed and lasers constructed in the performance of this development program permit a number of conclusions to be drawn. Primarily, the output power and efficiency of an LED-pumped Nd:YAG laser can be improved by the use of index-matching techniques. The basic premise of this approach was never in doubt but many questions regarding its parctical realization did exist. Generally speaking, these questions have been resolved by successful experiments. It was demonstrated that these index-matching techniques improved the diode array output efficiency from 160 to 200 percent at various temperatures. A maximum CW output power of 27 mW was achieved with the index-matching cylinder compared with 6.7mW with a conventional metal reflector.

Although this improvement is significant, it does not represent good agreement with the theoretically predicted goal. For the above mentioned case, the anticipated improvement was 324 percent. One of the significant factors reponsible for this departure lies in the difficulty of optical alignment. These lasers have proven to be very sensitive to alignment of the array and rod in the reflector. Not only is the output power and threshold strongly dependent on the alignment but also the transverse mode structure can be controlled to some extent by it. In the design of these lasers the image of the diode array in the laser rod was selected to be approximately the same width as the fundamental mode diameter which is about half the rod diameter or one-quarter of the rod volume. When the image is precisely aligned in this mode, volume laser operation over a wide range of input power (> 2x threshold) is in TEM_{00} mode. It was found that this operation could only be achieved with certain doide arrays, namely those for which the vertical positioning of the diode chips on the substrate and the flatness of the substrate met the $\pm 25\ \mu$m tolerance which was held on the horizontal positioning. Unfortunately, this was not the typical case. Instead, this tolerance was nearer to $\pm 50\ \mu$m although the deviation between adjacent diodes was generally much less. Two factors contribute to this difficulty, warpage of the substrate and variations in diode thickness.

It may be concluded from these experiments that the glass circular cylinder is a satisfactory pumping cavity reflector with regard to surface figure and performance. In particular, designs in the difference in thermal expansion between the cylinder and other laser elements must be considered. During this program no completely satisfactory solution was found for the problem of index matching

between the diode surface and the reflecting cylinder. An early candidate for this role, low melting point glass, was rejected when efforts to make "flip-chip" diodes failed. The "n-up" diode lead wire which is bonded to the upper surface of the diode is vulnerable to damage from thermal expansion of this material. The presence of the wires constrains the choice of materials to liquids, particularly viscose, noncorrosive liquids. The substance used in most of these experiments, Lens Bond, is a two-part adhesive of which only the uncatalyzed resin was used. In most respects, this material was satisfactory although a higher refractive index is desirable, however, in long term (30 days) use, it is found that the resin solidifies and may then damage the array.

The results reported for this program were achieved with selected laser rods. A wide variation in threshold (50%) and output power was found among laser rods with identical specifications. The cause of this variation was not investigated but could lie in bulk material properties, fabrication-induced strain, coating variation, figure variation or perhaps doping density. The diode-pumped laser is an excellent tool for further investigation of many of these rod characteristics since rods can be rapidly substituted with good control of pumping parameters and with no thermally-induced strain.

Further increases in output power ($\sim$ 100mW) and efficiency (0.3%) can be made by improvement in the diode technology while maintaining or improving the long lifetime characteristics demonstrated in this program. The principle improvement should be based on the "flip-chip" diode configuration. Although a few of these diodes have been made under another program (Contract #NAS5-11447), some difficult fabrication problems still persist. These problems are not unsolvable but will require a unified effort in material growth and device fabrication. The rewards of this improvement are many. Diode efficiency will be increased by the present contact masking factor (1.35); the problem of diode thickness variation will be eliminated, thereby improving the vertical positioning precision; the thermal characteristics will be greatly improved since the distance between junction and heat sink will be greatly reduced (factor of 1/5) and the device resistance will be reduced; and additionally, the elimination of the leads from the diode surface will reduce the index matching problem.

With such improved diodes, it will then be reasonable to increase the diode emission width, rod diameter and mode diameter to increase the total power output. The final result should be a very stable, long-lived laser with a power output of the order of 100 mW.

1. Reuter, W., Rupprecht, H., and Woodall, J. M., "Liquid Phase Epitaxial Growth of $Ga_{1-x}Al_xAS$," Journal of the Electrochemical Society, Vol. 116, No. 6, June 1969.

2. Capik, R. J., Hayashi, I., Miller, B. I., and Pinkas, E., "Reproducible Liquid-Phase Epitaxial Growth of Double Heterostructure GaAs-$Al_xGa_{1-x}As$ Laser Diodes," Journal of Applied Physics, Vol. 43, No. 6, pp. 2817-2826, June 1972.

3. Shockley, W., "The Theory of p-n Junctions in Semiconductors and p-n Junction Transistors," Bell System, Technical Journal, Vol. 28, pp. 435-489, July 1949.

4. Noyce, R. N., Sah, C. T., and Shockley, W., "Carrier Generation of Recombination in p-n Junctions and p-n Junction Characteristics," Proc. IRE, Vol. 45, pp. 1228-1243, September 1957.

5. Geusic, J. E., and Koningstein J. A., "Energy Levels and Crystal Field Calculations of Neodymium in Yttrium Aluminum Garnet," The Physics Review, Vol. 136, No. 3A, pp. A711-A716, November 2, 1964.

6. Geusic, J. E., et al, "Continuous 0.532 μ Solid State Source Using $Ba_2NaNb_5O_{15}$," Applied Physics Letters, Vol. 12, No. 9, pp. 306, May 1, 1968.

7. (a) Krupke, William F., "Radiative Transition Probabilities Within the $4f^3$ Ground Configuration of Nd:YAG," IEEE Journal of Quantum Electronics, Vol. QE-7, No. 4, pp. 153, April 1971.

   (b) Geusic, J. E., "The Development of the Continuous Room Temperature YAIG:Nd Laser," Final Report on Contract DA-36-039-AMC-02333(E), August 30, 1965.

8. Krupke, William F., private communication, December 1972.

9. Brock, E. G., et al, "Laser Modulation at the Atomic Level," Final Report NASA CR-66, February 1966.

10. Tang, C. L., "On Maser Rate Equations and Transient Oscillations," Journal Applied Physics, Vol. 34, pp. 2935-2940, October 1963.

11. Kleinman, D. A., "The Maser Rate Equations and Spiking," The Bell System Technical Journal, pp. 1505, July 1964.

12. Chesler, R. B., Geusic, J. E., and Karr, M. A., "An Experimental and Theoretical Study of High Repetition Rate Q-Switched Nd:YAG Laser," Proceedings of the IEEE, Vol. 58, No. 12, pp. 1899, December 1970.

13. Geusic, J. E., Kushida, Takashi, and Marcos, H. M., "Laser Transition Cross Section and Fluorescence Branching Ratio for Nd^{3+} in Yttrium Aluminum Garnet," Physics Review, Vol. 167, No. 2, pp. 289, March 10, 1968.

14. Marinace, J. C., "High Power CW Operation of GaAs Injection Lasers at 77° K," IBM Journal Research Development, Vol. 8, pp. 543-544, November 1964.

15. Kitasawa, F., Nishizawa, J., and Takamiya, S., "Amplitude Modulation of Diode Laser Light in Millimeter-Wave Region," Proc. IEEE (Letters), Vol. 56, pp. 135-136, January 1968.

16. Bowness, C., "On the Efficiency of Single and Multiple Elliptical Laser Cavities," Applied Optics, Vol. 4, No. 1, pp. 103-107, January 1965.

17. Neeland, J. K., Evtuhov, V., "Multiple Pass Effects in High Efficiency Laser Pumping Cavities," Applied Optics, Vol. 6, No. 3, pp. 437-441, March 1967.

18. Church, C. H., and Liberman, I., "The Spherical Reflector for Use in the Optical Pumping of Lasers," Applied Optics, Vol. 6, No. 11, pp. 1966-1968, November 1967.

19. Roess, Dieter, "Exfocal Pumping of Optical Masers in Elliptical Mirrors," Applied Optics, Vol. 3, No. 2, pp. 259-265, February 1964.

20. Hillman, D. K., and Smith, G. E., "The High Brightness LED," IEEE Spectrum, Vol. 5, No. 1, pp. 62-66, January 1, 1968.

21. Lockwood, H. F., "Polarization in Junction Luminescence," Journal of Applied Physics, Vol. 34, No. 7, pp. 2110-2111, July 1963.

22. Jenkins and White, "Fundamentals of Optics," p. 510, McGraw-Hill Book Co., Inc. New York 1957.

23. R. Puttback of Airtron, N. J., private communication.

24. Jordan, Edward C., "Electromagnetic Waves and Radiating Systems," Chapter 5, Prentice-Hall Inc., Englewood Cliffs, N. J., 1958.

25. Danielmeyer, H. G., and Ostermayer, Jr., F. W., "Diode-Pumped-Modulated Nd:YAG Laser," Journal Applied Physics, Vol. 43, No. 6, pp. 2911-2913, June 1972.

26. Brandewie, R. A. and Telk, C. L., "Quantum Efficiency of Nd^{3+} in Glass, Calcium Tungstate and Attrium Aluminum Garnet, "Journal of the Optical Society of America, Vol. 57, No. 10, pp. 1221-1225, October 1967.